

Electronic Theses and Dissertations, 2004-2019

2015

Thermally induced motion, collision and mixing of levitated droplets

Ashkan Davanlou
University of Central Florida

 Part of the [Mechanical Engineering Commons](#)
Find similar works at: <https://stars.library.ucf.edu/etd>
University of Central Florida Libraries <http://library.ucf.edu>

This Doctoral Dissertation (Open Access) is brought to you for free and open access by STARS. It has been accepted for inclusion in Electronic Theses and Dissertations, 2004-2019 by an authorized administrator of STARS. For more information, please contact STARS@ucf.edu.

STARS Citation

Davanlou, Ashkan, "Thermally induced motion, collision and mixing of levitated droplets" (2015).
Electronic Theses and Dissertations, 2004-2019. 5012.
<https://stars.library.ucf.edu/etd/5012>

THERMALLY INDUCED MOTION, COLLISION AND MIXING OF LEVITATED
DROPLETS

by

ASHKAN DAVANLOU

B.S. Sharif University of Technology, 2007

B.S. Aachen University of Applied Sciences, 2008

M.S. Aachen University of Applied Sciences, 2011

M.S. University of Central Florida, 2013

A dissertation submitted in partial fulfillment of the requirements
for the degree of Doctor of Philosophy in Mechanical Engineering
in the Department of Mechanical and Aerospace Engineering
in the College of Engineering and Computer Science
at the University of Central Florida
Orlando, Florida

Summer Term
2015

Major Professor: Ranganathan Kumar

© 2015 Ashkan Davanlou

ABSTRACT

This dissertation investigates the motion of a levitated droplet experimentally and analytically against the Marangoni flow in an immiscible outer fluid at higher speeds than is possible currently. Based on our earlier experiments, when a droplet is released from a height of 1.5 – 4 times its diameter from the liquid surface, it can overcome the impact and stay levitated at the liquid-air interface due to the existence of an air gap between the droplet and the liquid film. In order to explain this behavior of droplet traveling against the counter-current motion, we propose a simple approach: first, the Marangoni convection inside the thin film is considered without the droplet floating on the surface. By using a level-set method and solving the Navier-Stokes equation, the free surface velocity and deformation are calculated. Then, these quantities are used to solve for droplet velocity and drag coefficient simultaneously using a force balance. In order to compare the simulation results, experiments with levitated water droplets on an immiscible carrier liquid, FC-43, were conducted for various temperature gradients, and droplet velocities were measured at different locations using high-speed imaging. The experimental results are in good agreement with the developed theoretical model. For a Reynolds number range of 2-32, it is shown that the drag coefficients are up to 66% higher than those for the fully immersed sphere at the same Reynolds numbers. A correlation is proposed to calculate the drag coefficient of levitated droplets for various temperature drops across the channel.

For the first time, it is shown that it is possible to realize the natural coalescence of droplets through Marangoni effect without any external stimulation, and deliver the coalesced droplet to a certain destination through the use of surface tension gradients. The effects of the various shapes

and sizes upon collision are studied. Regions of coalescence and stretching separation of colliding droplets are delineated based on Weber number and impact number. The existence of the transition line between coalescence and stretching separation in this passive mode of transport is similar to what was observed in the literature for forced coalescence at significantly higher Weber numbers. It is also found that a thermocapillary environment improves the mixing process. In order to illustrate and quantify the mixing phenomenon, the dispensed droplets were made of potassium hydroxide and phenolphthalein which is used as a pH indicator. The experiments show the possibility to reach mixing rates as high as 74% within 120 ms. This study offers new insight to thermo-coalescence and demonstrates how natural coalescence could be used to transport, mix and collect biochemical assays more efficiently. The results of this research can be engineered to enhance the performance of self-cleaning surfaces and micro-total analysis systems (μ TAS), where sample transport, filtration, chemical reactions, separation and detection are of great interest.

*To my amazing family, Jimi, Giti & Majid for their endless love, support & encouragement.
My dad is my best mentor in life & source of inspiration; my mom is an exceptional teacher who
teaches me valuable life lessons; my brother is my rock & best friend.*

To Rebecca for her passion & love.



ACKNOWLEDGMENTS

I want to show gratitude to those who helped shape this dissertation. First and foremost, I have to thank my parents for their unconditional love and support throughout my life. Thank you for giving me the confidence and strength in achieving my goals and dreams.

I would like to sincerely thank my advisor and mentor, *Professor Ranganathan Kumar*, for his guidance and support. Also for believing in me and inspiring creativity and growth. I am grateful to Dr. Hyoung Jin Cho, Dr. Hansen Mansy, Dr. Bhimsen Shivamoggi, and Dr. Weiwei Deng who served as my committee members and gave me their valuable feedback. I want to give my gratitude to Rebecca Capell, who has given me her precious critique and proofreading. The comments I received from this group of people, has profoundly improved the composition and quality of this thesis.

To all my friends at UCF, especially my lab mates during last four years; Abhishek Saha, Joshua Lee, Benjamin Patrick, James Wilson, Michael Gabany, Pretam Choudhury, Eduardo Castillo-Orozco, Kalpana Hanthanan Arachchilage and Majid Haghshenas. I am grateful, for all their continued support, teamwork, and collaboration. I would like to sincerely thank Jeanine Clements for helping me throughout the graduate program. Also, I like to acknowledge Alireza Karbalaee for fabrication of silicon platform and assistance in glucose experiments. Finally, I thank the National Science Foundation for supporting this work (ECCS-1102280).

TABLE OF CONTENTS

LIST OF FIGURES	x
LIST OF TABLES	xvi
CHAPTER 1: INTRODUCTION	1
1.1: Microfluidics	1
1.2: Droplet actuation mechanisms	3
1.3: Harnessing the Marangoni effect as droplet actuation mechanism.....	9
1.4: Organization of dissertation	10
CHAPTER 2: COUNTER-CURRENT MOTION OF LEVITATED DROPLETS ON A LIQUID FILM UNDERGOING MARANGONI CONVECTION	12
2.1: Introduction	12
2.2: Experimental setup.....	14
2.3: Results and discussion.....	18
2.3.1: Experimental levitation of spherical droplets.....	18
2.3.2: Theoretical model for Marangoni convection in thin film	22
2.3.3: Model for the motion of levitated droplets.....	31
2.4: Conclusion.....	38
CHAPTER 3: LIFETIME OF LEVITATED LIQUID DROPLETS.....	40
3.1: Introduction	40

3.2: Theoretical Background.....	42
3.3: Experimental Work.....	44
3.4: Results and Discussion	46
3.5: Summary.....	51
CHAPTER 4: THERMALLY INDUCED COLLISION OF DROPLETS IN AN IMMISCIBLE OUTER FLUID	52
4.1: Introduction.....	52
4.2: Methods	56
4.3: Results.....	59
4.4: Discussion.....	69
CHAPTER 5: PASSIVE MIXING ENHANCEMENT OF MICROLITER DROPLETS IN A THERMOCAPILLARY ENVIRONMENT.....	72
5.1: Introduction.....	72
5.2: Experimental Setup.....	74
5.3: Results and Discussion	75
5.4: Summary.....	83
CHAPTER 6: APPLICATIONS.....	84
6.1: Applications	84
6.1.1: Introduction	84

6.1.2: Design and fabrication.....	85
6.1.3: Transferring, trapping and mixing of biological assays	87
CHAPTER 7: SUMMARY AND OUTLOOK.....	92
7.1: Conclusions	92
7.2: Outlook and future directions.....	94
APPENDIX: THEORETICAL MODEL FOR MARANGONI FLOW INSIDE THE THIN FILM AND DROPLET MOTION	97
Governing Equations.....	98
Model for the Motion of Levitated Droplets	99
LIST OF REFERENCES	100

LIST OF FIGURES

Figure 1.1: Available techniques for droplet manipulation: optical, magnetic, electrowetting, thermal, piezoelectric and chemical methods.	5
Figure 2.1: Schematic of experiment set-up.	15
Figure 2.2: (Top) Schematic illustration of counter-current motion of a levitated droplet against the Marangoni flow. The dashed lines depict the Marangoni circulation inside the thin liquid (FC-43) film with a thickness of 2 mm. (Bottom) Motion of a levitated droplet (d=1.5 mm) toward the warmer region captured at 100 fps with IR camera. Average velocity was measured at 12.2 mm/s using sequential pictures from a high-speed camera at 2000 fps. The imposed thermal gradient is 0.89 °C/mm.....	17
Figure 2.3: Motion of a spherical drop (3 mm diameter). a) Steady temperature distribution along the platform from the IR-camera, b) The corresponding thermal gradient which causes spherical drops to get attracted to higher temperature regions.....	20
Figure 2.4: Experimental droplet velocity for a 3mm diameter droplet along the channel. Thermal gradients cause spherical drops to get attracted to high temperature regions. Steeper temperature gradient leads to higher droplet velocity along the axis.	21
Figure 2.5: Photograph of the levitated droplet merged with the schematic. Deformation and airflow generated at the free surface of a thin immiscible liquid layer (exaggerated for clarity) propels a levitated droplet towards the hotter end of the test section.	21
Figure 2.6: Computational domain.	24
Figure 2.7: Surface velocity magnitudes (m/s) for the steady state case (from top to bottom); $\Delta T=5\text{ }^{\circ}\text{C}$, $\Delta T=10\text{ }^{\circ}\text{C}$, $\Delta T=15\text{ }^{\circ}\text{C}$, $\Delta T=25\text{ }^{\circ}\text{C}$. The colors represent velocity in m/s.....	28

Figure 2.8: Numerical solution: free surface velocity variation along X for four temperature differences.....	29
Figure 2.9: Non-dimensional free surface profile at steady state for various temperature gradients.....	29
Figure 2.10: Deformation of the free surface due to an imposed thermal gradient (case 2 in Table 2.3) is shown in dotted blue line. The circulation results from Marangoni effects inside the carrier liquid and the arrows depict the velocity field where the average surface velocity for this specific temperature is 17 mm/s. <i>Note that the y-axis is stretched to show better clarity while the x-axis is limited to only 30 mm.</i>	30
Figure 2.11: Dimensional drop velocity from experiments compared to the model predictions (solid line) for four temperature drops. (a) $\Delta T=25$ °C, (b) $\Delta T=15$ °C, (c) $\Delta T=10$ °C, and (d) $\Delta T=5$ °C.....	35
Figure 2.12: Droplet velocity normalized by surface velocity for various temperature drops. Symbols show experimental droplet velocity at the same X^* locations but different ΔT . The solid line is the curve-fit generated from the numerical results for 4 different cases.....	36
Figure 2.13: (a) Velocity scale variation with temperature drop in the channel, (b) Drag coefficient versus Reynolds number for levitated drop compared with the fully immersed case (Morrison 2013).....	38
Figure 3.1: (a) Free surface profile of the liquid film in vicinity of the contact line, (b) A levitated drop from the side, the underlying air film is shown in red as t	43
Figure 3.2: Schematic of experimental setup.....	45

Figure 3.3: Levitation of a liquid droplet on the liquid pool of a distinct immiscible fluid. (a) Droplet floats above the air/liquid interface. The inset magnifies the interstice under droplet where the air gap is present. (b) As the temperature of the droplet rises, the air gap shrinks. (c) After thermal equilibrium, the droplet partially submerges within the pool. The vectors inside the liquid pool show the surface tension forces, while the vectors outside show the air flow. Droplet is 3 mm and $\Delta T = 10\text{ }^\circ\text{C}$ between two media. 46

Figure 3.4: Variation of droplet lifetime with temperature for a 3 mm drop released at a height of 4.5 mm above the pool. $T_p - T_d$ is the difference of temperature between the pool liquid and the droplet at the time of landing. Droplet temperature rise will eventually lead to rupture of the air film. 47

Figure 3.5: Theoretical relationship between film thickness and temperature difference for silicon oil droplets on a silicon oil pool and water droplets on a FC-43 pool. 49

Figure 3.6: Effect of droplet size on its lifetime (droplet: water; pool: FC-43). 50

Figure 4.1: Normalized release height as a function of Bond number ($Bo = \rho g H^2 \sigma$, where H is the releasing height). Droplet diameters are indicated in red. Weber number is calculated as $We = \rho U^2 D_{drop} / \sigma$, where U is the impact speed which is a function of release height given as $U = 2gH$ 55

Figure 4.2: The experimental setup to study the collision of droplets on thin liquid films due to Marangoni effect. The micro-heaters are made out of copper. Light source and cameras are aligned with the droplet migration. An infrared camera is used to monitor the temperature variation of droplets and the carrier liquid. Droplets are produced from a precision needle that is kept at a constant height from the film. 57

Figure 4.3: (a) The trajectory of a 3mm droplet for a temperature drop, ΔT , of 20°C across the channel is shown on an infrared image. The black circles represent the position of the droplet at every 14 frames; (b) Liquid film's temperature profile along the y-axis symmetry line of the channel from IR measurements. The heater is turned on right after the droplet is released..... 60

Figure 4.4: Variation of droplet velocity with temperature difference ($\Delta T=60$ °C). Velocity scale (theoretical), sessile drop velocity and spherical drop velocity (experimental) for a 3 mm water drop are shown. The velocity scale data are curve-fitted to show the trend. The inset shows experimental results compared to velocity scale for $\Delta T=40$ °C. 61

Figure 4.5: Transport and coalescence of levitated droplets. Initially, all heaters except the one shown as 'off' are active. The first droplet of potassium hydroxide is levitated at one end of the printed circuit board, and is allowed to flow through Path 1. After it migrates to the more powerful central heater, a second levitated droplet, phenolphthalein, is allowed to flow through Path 2 under the same condition. The drops collide and mix into a larger pink droplet. With continuous heating, the air layer underneath the droplet is ruptured, and the droplet sinks and becomes a sessile drop without being pinned. The sessile drop then moves towards lower temperature through Path 3. This dual migration of droplet moving towards or away from the heat source is governed by the thermocapillary effect due to the drop shape effect. The inset on the left shows the schematic for the migratory behavior of the levitated droplet against Marangoni convection. The inset on the right shows the schematic for the larger coalesced sessile droplet moving away from the heat source in the direction of the maximum temperature gradient. 63

Figure 4.6: Analytically obtained regions of coalescence, reflexive separation, and stretching separation for equal-sized water droplets based on Ashgriz and Poo (1990) and Qian and Law (1997). The inset shows that collision of drops on a thin film leads to two distinct regimes at very low Weber numbers ($2.5 \text{ mm} \leq D \leq 3.6 \text{ mm}$). Each square shows one experiment..... 65

Figure 4.7: A sequence of high-speed images show the stages of head-on collision that lead to permanent coalescence ($\Delta T=20^\circ\text{C}$, $D=3 \text{ mm}$, $We=0.012$). Both the droplets and their reflection are seen until they coalesce..... 66

Figure 4.8: Snapshots of the collision of identical droplets for $\Delta T = 20 \text{ }^\circ\text{C}$. (a) coalescence of spherical-shaped water droplets ($D= 3 \text{ mm}$, $v= 10.2 \text{ mm/s}$, $We= 0.012$); (b) stretching separation of spherical-shaped water droplets ($D= 3 \text{ mm}$, $v= 10.2 \text{ mm/s}$, $We = 0.012$); (c) coalescence of sessile water droplets on a liquid substrate ($D= 2.5 \text{ mm}$, $v= 14 \text{ mm/s}$, $We= 0.0067$). 68

Figure 4.9: Impact number vs. Weber number for silicon oil drops ($D= 3 \text{ mm}$) of various viscosities. Increase in viscosity leads to higher chance of coalescence even at slightly larger impact numbers. 70

Figure 5.1: Schematic diagram of the experimental setup. Phenolphthalein (HIn) is a pH-indicator that turns pink in a base solution like potassium hydroxide..... 75

Figure 5.2: (a) Head-on collision of droplets. After coalescence due to chemical reaction the color change occurs. Image processing of the coalesced droplet can be divided into: (b) mixing is captured as a color image; (c) conversion of this color image into a grayscale image; (d) conversion of the grayscale image into a binary image; (e) background subtraction and quality improvement on the binary image. 77

Figure 5.3: Schematic diagram of collision and mixing of two equal-sized droplet. 77

Figure 5.4: (a) The variation of mixing efficiency with temperature for three different diameters at 100 ms, (b) platform surface temperature increases almost linearly due to a $\Delta T = 30\text{ }^\circ\text{C}$, (c) The schematic depicts the counter-motion of the droplet towards the heat source against Marangoni flow in the liquid substrate. The initial temperature of the liquid substrate is measured using the IR-camera immediately prior to droplet release, (d) Variation of droplet surface temperature as it migrates towards the heater. 79

Figure 5.5: (a) Mixing progress with time for different drop sizes at $\Delta T = 25\text{ }^\circ\text{C}$. (b) Dependence of Reynolds number with mixing time. 81

Figure 5.6: Normalized mixing time with convection time scale versus Reynolds number. 83

Figure 6.1: The fabrication procedure of the silicon wafer with embedded microheaters. 85

Figure 6.2: Schematic of the experimental setup..... 86

Figure 6.3: A 3mm water droplet migrates towards the heat source. (a) Snapshot of droplet transport, (b) Infrared images of the same phenomenon. 88

Figure 6.4: Trapping of a drop is realized through applied thermal gradient. 89

Figure 6.5: Demonstration of mixing and further manipulation of glucose and enzyme drops after coalescence at selected times. 90

Figure 7.1: (a) Schematic of a generated droplet where cells are within RPMI medium. (b) White light image of a 2mm droplet containing the cell buffer, fluorescence image and overlap of earlier two images (from left to right)..... 96

LIST OF TABLES

Table 1.1: Comparison between conventional droplet actuation mechanisms.	7
Table 2.1: Physical properties of aqueous droplet and the fluorocarbon carrier liquid at room temperature.	16
Table 2.2: Boundary conditions.	25
Table 2.3: Main parameters of the theoretical-experimental model.	35
Table 3.1: Surface tension variation with temperature (± 0.1 mN/m).	45
Table 4.1: Physical properties of tested liquids. Some of the properties are taken from Wehking et al. (2013).	58
Table 5.1: The range of dimensionless numbers at different ΔT s. The data is sorted according to the droplet size and volume.	80

CHAPTER 1: INTRODUCTION

1.1: Microfluidics

Microfluidic devices handle small volumes of fluids. The initial spark in this area was made in the early 80s when inkjet print-heads were being developed. Meanwhile the advancements in the MEMS industry and IC technology revolutionized the field of microfluidics. Nowadays many technologies including analytical devices, DNA chips, micro-propulsion and micro-thermal exploit the precise control and manipulation of sub-millimeter fluids. Increasing interest along with large investments from research agencies and industry have facilitated the growth of this field. The research of microfluidics is predicted to grow by 23% by 2019, with funding estimated to reach 5.3 billion dollars (Persistence Market Research, 2014). The major areas of interest will be pharmaceuticals, life science, rising point of care testing (POCT) and drug delivery (inhalers, micropumps, and microneedles). There are three classifications of microfluidic systems: continuous-flow microfluidics, digital microfluidics and droplet-based microfluidics. These categories are further discussed in this dissertation.

In continuous-flow microfluidics, reagents and samples move within microfabricated channels. These microchannels are generally manufactured from glass, silicon, Teflon, Parylene, or PDMS. Different actuation mechanisms exist for continuous flow generation, which can be either mechanical (membrane pumps that require moving parts), or non-mechanical (based on capillary or surface effects without any need for moving parts). Table 1 summarizes and gives examples of different available methods. Continuous-flow microfluidics is more suitable for basic biochemical applications that do not require high precision or flexibility. Another issue in

closed-channels is the surface adsorption (Basu 2010), which can cause contamination or blockage (McClain et al. 2003). For example, this occurs regardless of the hydrophobic materials, which have low surface hydration energies (Gascoyne et al. 2004) like proteins and DNA with channel walls.

Compared to the closed-channel continuous-flow systems, in digital microfluidics (DMF), we deal with an open array of electrodes, which manipulates discrete fluids. These devices control the displacement of droplets with using surface properties. Varying electric potential can control the hydrophobicity of the substrate and contact angle of the drop with the surface. The name, digital microfluidics, is influenced by the analogy of digital microelectronics. In DMF, pico to nanoliter droplets can be manipulated to perform fluidic operations by applying electrical potential to an array of patterned electrodes with a hydrophobic insulator (Jebrail et al. 2012). Although electrowetting is known as the main actuation mechanism in DMF, there are several other techniques implemented for droplet manipulation, such as: dielectrophoresis, acoustic waves and optoelectrowetting and mechanical actuation. The main advantages of DMF are flexible device geometry, easy integration with other technologies and a simple device structure. Many of the lab-on-a-chip (LOC) applications are based on DMF technology. This type of microfluidic device is able to manipulate liquid samples in the form of droplets in an immiscible phase, where Reynolds number is low (viscous flow) and flow regimes are laminar. The capability of this new technique in generating nano to picoliter droplets has spurred new interest in this field. These droplets are used to encapsulate reagents and perform chemical or biological reactions in microscale platforms. Droplet-based microfluidics with precise drop control allows user-defined transport and merging (Song

2003). Within this technology, consumption of fluids (chemical/biological compounds) is significantly reduced. Moreover, parallel actuation of multiple droplets is feasible. While some systems require channels in order to move droplets, other systems take advantage of the different physical or chemical properties in realizing the droplet motion on a substrate. The following section will discuss these principles in detail.

The usage of droplet-based microfluidic devices for *in-vitro* diagnostics is prevalent. For example: optimizing protein crystallization condition (Zheng et al. 2003), diffusive mixing in an enzyme kinetic reaction (Song et al. 2003), DNA manipulation (Nakano et al. 2003), and cell study (He et al. 2005). Some of these techniques are extended to micro total analysis systems (μ TAS) and provided a powerful infrastructure for analytical devices. Many biochemical experiments require certain fluidic operations to fulfil their mission. Below is the description highlighting the various actuation mechanisms.

1.2: Droplet actuation mechanisms

Microfluidic devices has attracted wide attention due to their applications in drug screening, chemistry and biological research, diagnostics and material science (Sackmann et al. 2014; Wang and Zhe 2011; Piper et al. 2007; Zhang et al. 2011; Huang et al. 2014; Jebrail et al. 2012). The first generation of microfluidic devices was used continuous-flow microfluidics, where a single-phase liquid was manipulated through enclosed microfabricated channels. In order to actuate the liquid flow in a microchannel, a high driving force is required to overcome the surface tension force, therefore miniaturization has always been a challenge. In addition, these systems can suffer contamination as well as sample evaporation issues (Wu and Suzuki 2011; Hu and Ohta 2011). Deficiencies like these one motivated scientists to innovate the use of droplet-based

microfluidics technology. The use of discrete fluids, in the form of microdrops, results in less sample consumption, which is critical in bioanalysis, but also lower fabrication costs and a higher level of flexibility (Long et al. 2009). The discovery of polydimethylsiloxane (PDMS) material has had an undeniable impact on microfluidic devices. The reason is PDMS is optically transparent, with high elasticity due to its polymeric nature, and can be easily fabricated with a soft-lithography technique. Over the last decade numerous droplet actuation mechanisms were studied including optical forces (Hu and Ohta 2011; Kotz et al. 2004), magnetic forces (Zhao et al. 2010; Lehmann 2006 et al.; Nguyen et al. 2007), dielectrophoresis (Milman et al. 2005; Schwartz et al. 2004; Jones et al. 2001; Park et al. 2010); , acoustic waves (Friend and Yeo 2011; Guttenberg et al. 2005), and thermocapillary forces (Hu and Ohta 2011; Basu and Gianchandani 2009; Burns and Srivastava 2006; Davanlou et al. 2013; Davanlou et al. 2015; Selva et al. 2010). Table 1.1 summarizes the studies done on conventional actuation mechanisms, and compares the advantages and disadvantages.

In one approach, light is utilized as a manipulation method to induce forces on particles or fluids through momentum or energy transfer. These methods can be utilized directly or indirectly. Direct methods such as optical tweezers directly interact with the object while indirect methods rely on the modification of material property. Indirect methods change the interfacial tension, the surface energy or photoconductivity using light energy. Optical manipulation has few major issues. Since the forces that is induced by Marangoni circulations is small, only manipulation of small sized droplets is possible. Another drawback is that optothermal technique requires an external light source (normally a laser), which makes the

configuration complicated and the scalability of the platform limited. The optical tweezers functionality is based on refraction index, meaning they only absorb particles with a higher refractive index versus the surrounding medium (Basu 2008) and requires careful selection of droplet types. Figure 1.1 depicts some of the main droplet actuation mechanisms that have been tested so far.

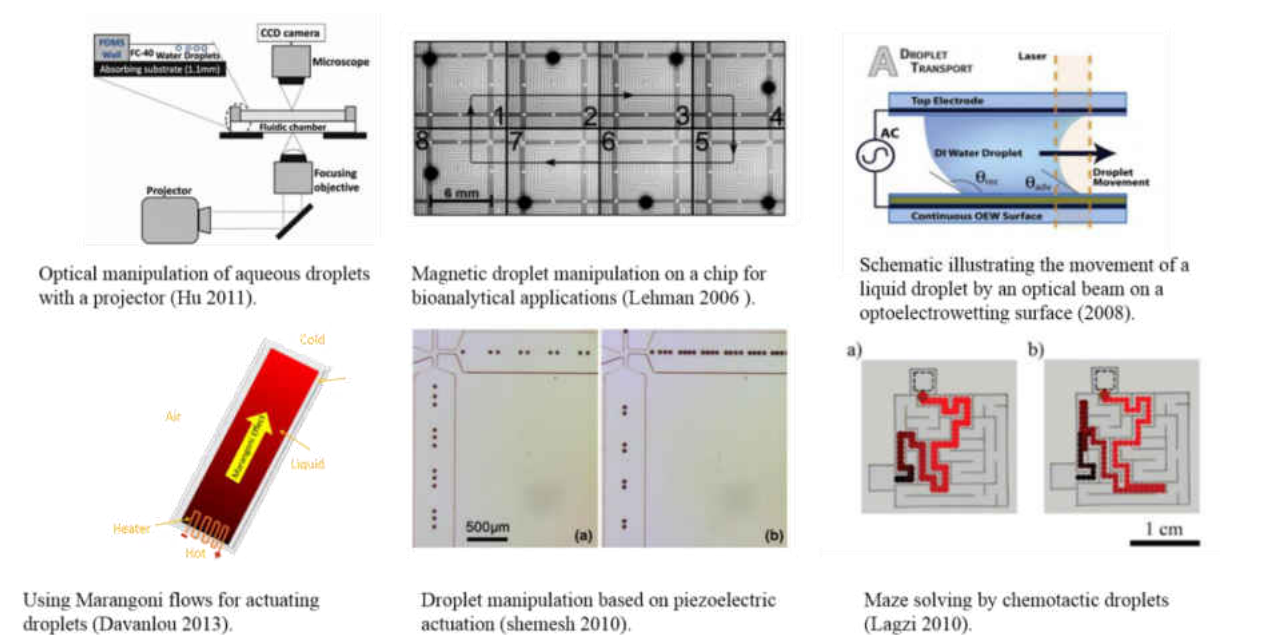


Figure 1.1: Available techniques for droplet manipulation: optical, magnetic, electrowetting, thermal, piezoelectric and chemical methods.

Electrowetting is another popular technique for droplet actuation that uses electric potential over surface electrodes to manipulate droplet movements (Pollack 2002). The lower surface is coated with a hydrophobic layer, which after applying the voltage to electrodes it changes to hydrophilic surface therefore, an aqueous droplet attracts to the surface. By controlling the electrodes, one can change the contact angle of droplets on a surface as a result of surface energy alterations. If surface tension gradients are created with optical techniques rather than electric fields this is called optoelectrowetting. In both methods, the droplet must contact with the

substrate and wet it. However, this approach might not be favorable due to possible contamination, sample loss and contact angle hysteresis issues for sensitive experiments. Despite the appeal for the use of electrowetting, the demand of high voltage as well as limited choice of carrier liquid proves the restrictions of this approach. In dielectrophoresis a force is exerted on a dielectric particle due to non-uniform AC electric fields. As a result, the manipulation of polarizable microparticles, e.g. cells, marker particles, suspended in a liquid medium are possible (Jones 2003). Since there is no necessity for direct contact in this method, potential applications in μ TAS technology is predicted. Nevertheless dielectrophoresis is mostly applicable to ultra-small droplets up to 100 nL (Gascoyne 2004) and contamination is questionable. Creating a magnetic field is an old-fashioned approach to move and manipulate droplets, which is done by using an array of coils. This requires inserting magnetic nanoparticles or beads inside of the droplets. Magnetism is also applied for conducting common operations such as transport and split of droplets (Leh 2007). Adsorption and scalability are mentioned as the main obstacles in further growth of this actuation method. Generating chemical gradients as a mean for droplet manipulation was also reported (Lagzi et al. 2010). The pH variations within a liquid surface move droplet toward regions of a lower pH. Therefore, tweaking surface tension can work as an actuation mechanism. Due to the problems with contamination and limited choice of liquids, this method is not favorable. Many of the conventional droplet-based techniques are susceptible to miniaturization, require a complex structure, are expensive or need an external triggering source. On the contrary, thermal actuation of microscale fluid elements is a unique choice since it is contact-free, easy to apply and practical. Thermal actuation is generally performed by using an array of

microfabricated heaters (Darhuber et al. 2003; Selva et al. 2010). These heaters generate a heat flux that can be engineered to create Marangoni flows in a desired direction; and as a result mixing, sorting, trapping and pumping operations would be possible. As of today, the full capabilities of Marangoni effect in continuous and discrete droplet manipulation schemes, specifically on a droplet actuation has not been explored. The previous studies on droplet manipulation (mostly conducted on solid substrates) has not been able to address the surface wetting and pinning issues.

Table 1.1: Comparison between conventional droplet actuation mechanisms.

Actuation Mechanism	Details	Advantages	Disadvantages	References
Dielectrophoresis	Movement of a particle in a non-uniform electric field due to the interaction of the particle's dipole and spatial gradient of the electric field.	Biocompatibility, simplicity	Limited choice of fluids, low sensitivity	Jones et al. 2001; Schwartz et al. 2004; Park et al. 2010
Optowetting	Radiation causes a gradient in surface free energy leading to the directional motion of the droplet.	Reconfigurable trajectories, parallel manipulation	Low transport velocity, evaporation, requires external component	Ichimura et al. 2000
Electrowetting	Changing the contact angle due an applied potential difference between the solid and the droplets.	Integrable with electrical components, simplicity	High driving voltage, biocompatibility issues, contamination, evaporation, pinning	Lee & Kim 2000; Chiou et al. 2008
Thermocapillary forces	Applying a thermal gradient generated causes circulation inside the liquid therefore migration of droplets.	Compatible with soft-lithography, fast control speed, contact-free, minimal sample adsorption	Sensitivity	Basu & Gianchandani 2009; Selva et al. 2010; Hu & Ohta 2011; Davanlou & Kumar 2015
Vibration	Creating vibrations on a hydrophobic substrate.	Contamination-free, biocompatibility	Additional instrument	Daniel et al. 2005
Magnetic forces	Magnetic particles inside droplets interact with a local field.	Ability to generate large forces, independent from dielectric properties	Using magnetic particles	Lehman et al. 2006; Nguyen et al. 2007; Zhao et al. 2010
Acoustic waves	Droplet is actuated via acoustic forces and pressure gradients without any contact.	Fast control speed, compatible with soft-lithography, parallel manipulation	Mostly for continuous flow, requires external component	Friend and Yeo 2011; Guttenberg et al. 2004

As shown in Table 1, thermocapillary effect is more beneficial when comparing it to other types of actuation mechanisms, as it is applicable for a wide range of fluids, is easy to fabricate and provides a fast and reliable actuation mechanism. In this approach, surface tension gradients caused by temperature or chemical concentration at an interface induces Marangoni-driven flows from regions of high surface tension to low surface tension. The creation of thermal gradients was realized using microfabricated heaters and optical heating. Optical manipulation is a contact-free approach that realized through low power lasers or light sources. Thus this approach is practical when drop sizes are small. The resistance heaters work as a heat source when an electric current passes through them (Joule heating principle). The fabrication of heaters are low-cost, easy to fabricate and tunable. In this work, the resistance heaters are used as the sole method of heat generation. So far the majority of droplet manipulation devices lack precise temperature control. Also selection of fluid type is restricted. Huang et al. (2014) proposed an open-surface droplet manipulation platform for biochemical reagents. Open-surface microfluidic devices have certain advantages such as open optical path, better accessibility and compatibility with biological experiments. Based on such advantages, this dissertation presents a silicon-based platform with embedded titanium heaters, which utilizes the thermocapillary effect to manipulate the droplets. The selection of material in our design allowed for a generation of sharp temperature gradients at low voltages. Also using an inert carrier liquid with low thermal conductivity has improved the cooling process. Thus, migration of droplets which have low vapor pressure or polarity is possible. The details of the fabrication process is mentioned in the next section. Our previous studies have shown that based on the release height, two distinct configurations are possible upon

impact of droplets, levitated or submerged, on the surface of an immiscible liquid. Applying a thermal gradient causes a spherical shape droplet to levitate on the air-liquid interface, to move towards the heat source due to surface deformation. However, a submerged droplet obeys the Marangoni flow and moves toward the cooler part of the surface that has a higher surface tension (similar to tracer particles). Here, we focus on levitated spherical droplets since they can achieve higher speeds and show better controllability. In addition, such drops are not affected by temperature as submerged drops. This can be attributed to the thin layer of air gap underneath the droplet which avoids the direct contact of two liquids. In the following section, the details of the fabrication process and experimental apparatus are provided. Then the actuation and trapping of water droplets creating controlled thermal gradients are demonstrated. The ability of the platform in accurate manipulation of reagents is verified by using glucose calorimetric assay in a series of experiments. Our programmable platform offers high-speed and accurate manipulation of droplets, where contamination, sample evaporation and contact angle hysteresis (pinning) are minimized. These unique properties make our approach an interesting choice for drug screening and biochemical analysis where high throughput analysis of small amount of samples in a short time is required.

1.3: Harnessing the Marangoni effect as droplet actuation mechanism

When a droplet is released from a certain height from the liquid surface, it can sustain the impact, preserve its spherical shape, and levitate on the surface. When one end of the test section is heated, Marangoni convection sets up a temperature gradient on the surface, which causes a surface tension gradient at the interface. This creates deformation of liquid surface with a downhill slope towards the maximum temperature. The spherical drops migrate from colder to

warmer regions against Marangoni convection and move towards the heated surface where maximum depression occurs. Despite the counter-current motion of the surface, the droplet moves down the surface slope due to gravity at a much higher speed than it would on a solid substrate. Increasing the thermal gradient leads to higher drift velocities for droplets of the same size. The IR images show that the droplet increases in temperature as it moves towards the heater, but stays at a significantly lower temperature than the ambient. Next, using the level-set approach the change of liquid film height, as well as surface velocity due to an imposed thermal gradient is calculated and compared with the experiment. This data is then used to solve for droplet velocity and drag coefficient solving a force balance through a fourth-order Runge-Kutta method.

Later, the collision of droplets levitated on Marangoni flow of a second immiscible liquid is studied. Non-dimensional numbers, such as Weber number and impact number are used to explain the phenomenon. A combination of different fluids is used to study the effect of viscosity on coalescence. The results in this work reveal that by creating a thermal map, it is possible to transport droplets to desired locations accurately, and also to drive droplets naturally to coalescence and mix them. Following this, the role of thermocapillary in enhancing the droplet mixing is investigated using image processing of droplets of multiple sizes. The possibilities of conducting chemical and biological reactions, manipulating the samples and collecting them will be further discussed and visually illustrated.

1.4: Organization of dissertation

In this thesis, after review of the literature on microfluidics and highlight the importance of this evolving field specifically the droplet-based microfluidics, the use of thermocapillary

effect to maneuver levitated droplets will be discussed. First, the criteria required for droplet levitation, details of the experimental setup and dual migration behavior of droplets are explored. The numerical simulation for Marangoni convection in thin films along with counter-current motion of levitated droplets in that medium will be experimentally and theoretically investigated in Chapter 2. In addition, the drag coefficient experienced by a spherical droplet will be calculated and compared with an immersed droplet of the same type. This will be followed by studying the parameters affecting the lifetime of a levitated droplet such as size and temperature difference in Chapter 3. The collision and merging of spherical droplets induced by surface tension gradient at the liquid-air interface is the central focus of chapter 4. It will be shown that changing the impact parameter and Weber number can affect the collision outcome and result in coalescence or stretching separation. Moreover, the effect of viscosity and surface tension on these regimes is further studied in that section. Based on the foundations developed, thermocapillary actuation could be used for actuation, merging and mixing of distinct samples. This is highlighted in Chapter 5, where the role of thermal gradient is considered in mixing phenomenon. In Chapter 6, the Marangoni convection is utilized in an open-surface platform manufactured through soft lithography on a silicon wafer. The capability of the platform in transport, trapping and mixing of reagents is shown. The performance of the microfluidic devices in fast and accurate manipulation of droplet illustrated through glucose-enzyme reaction. Finally, conclusion of the entire outcome observed in earlier sections along with an outlook and future directions will be presented in Chapter 7. Additional details regarding the governing equations are highlighted in the appendix.

CHAPTER 2: COUNTER-CURRENT MOTION OF LEVITATED DROPLETS ON A LIQUID FILM UNDERGOING MARANGONI CONVECTION

2.1: Introduction

Surface tension gradient caused by a temperature gradient on a liquid surface leads to an imbalance of tangential stresses at the fluid interface. Due to this surface tension gradient in the tangential direction, an unbalanced force distribution at the interface is created, which starts the fluid motion. This phenomenon is called the Marangoni effect. Several studies have numerically modeled the Marangoni convection during heating and evaporation of droplets (Raghuram et al. 2012; Son et al. 2014). The main focus of these studies were the effect of thermo-physical properties, phase change and contact line dynamics on droplet evaporation. However, the current study focuses on the surface distortion created by local heating of a thin sheet of liquid, which creates Marangoni convection. This distortion of the thin liquid sheet is due to the higher surface tension of colder liquid which pulls the warmer surrounding fluid with lower surface tension. There have been several investigations that take advantage of thermocapillary drift to actuate droplets on solid surfaces, however in all these works even at high temperature gradients the droplet velocity was low, i.e. microns per second, and the motion was in the direction of decreasing temperatures (Brochard 1989; Brzoska et al. 1993). The non-uniformity of the spreading coefficient ($S = \sigma_{\text{carrier}} - \sigma_{\text{carrier-drop}} - \sigma_{\text{drop}}$, where σ indicates interfacial tension) could be due to chemical agents on the solid surface, thermal gradients or electrical charge, and any of these could result in droplet motion. Issues such as droplet pinning or droplet evaporation has motivated researchers to use liquid platforms

instead of solid substrates where droplets would be dispensed on a layer of immiscible liquid and transported by means of thermal gradients (Grigoriev et al. 2006).

The thermocapillary drift of bubbles and droplets in reduced gravity was investigated thoroughly. Zhang et al. (2001) found the crucial role of inertia in determining an asymptotic solution for temperature field when a drop moves in a vertical temperature gradient at small values of thermal *Péclet* number. Marangoni flotation of liquid droplets was studied experimentally and numerically by Dell'Aversana et al. (1995). Their results suggested that surface tension gradient helps to form a stable air film in between the droplet and pool surface which prevents sinking of the droplet. Greco and Grigoriev (2009) investigated thermocapillary driven motion of interfacial droplets and found that in some cases, the droplet suspended at an interface of two liquid layers migrated in the direction opposite to the temperature gradient. Samareh et al. (2014) used the volume of fluid method to simulate thermocapillary migration of a deformable drop in immiscible fluids with variable surface tension. Wegener (2014) numerically studied the effect of droplet diameter, kinematic viscosity ratio and partition coefficient on the mass transfer of a solute in a Marangoni dominated liquid-liquid system. Wu (2014) under the quasi-steady state assumption modeled the thermocapillary droplet migration in a uniform temperature gradient at large Reynolds and Marangoni numbers.

Our preliminary experimental observations (Davanlou et al. 2014; Yakhshi-Tafti et al. 2010a; Yakhshi-Tafti et al. 2010b) showed for the first time that droplets can move in either direction of a thermal gradient, depending on its shape at the air-liquid interface. Infra-red thermal imaging was used to determine the surface temperature of the carrier fluid. It was demonstrated that a spherical drop moved towards the heat source, and a sessile drop away from

it. By using a simple analysis, it was conjectured that spherical drops would roll down the free surface slope due to gravity.

In the current study, using detailed modeling supported by experiments, it will be shown that the liquid surface deforms due to a temperature gradient, and that a levitated drop dispensed on the liquid surface moves down the slope with an air gap underneath, and does not roll down. The drops that do not levitate are submerged, revealing only a lens shaped surface above the fluid surface. Since the sessile drop has been investigated extensively in the literature, in this paper, we focus on levitated droplets. First, we provide a theoretical foundation to solve the Marangoni convection in the absence of droplet and obtain solutions for deformation at the free surface and free surface velocity. Using Marangoni solution for the slope of the liquid layer height and surface velocity, we then provide a model based on force balance to iteratively solve for drag coefficient and velocity of the droplet. The droplet velocity profile is then compared with the experimental profiles for four temperature gradients.

2.2: Experimental setup

A thin layer of Perfluorotributylamine (FC-43, 3M) is formed in a rectangular acrylic mini-channel. The dimensions of the experimental channel are $D=2\text{mm}$ deep, $W=8.5\text{mm}$ wide and $L=55\text{mm}$ long. Thermal gradients were created by passing electric current through Nichrome wire heater (28 Gauge, $4.15\ \Omega/\text{ft}$) as heating element (Fig. 2.1). In order to obtain temperature field across the platform a high-resolution, high-speed infrared thermal imaging system was used. Due to thermal capacitance, the time scale for the droplets to acquire the temperature of the surrounding fluid is larger than the time scale over which droplets move along the length

of the platform; hence they are essentially not at the same temperature as the surrounding liquid.

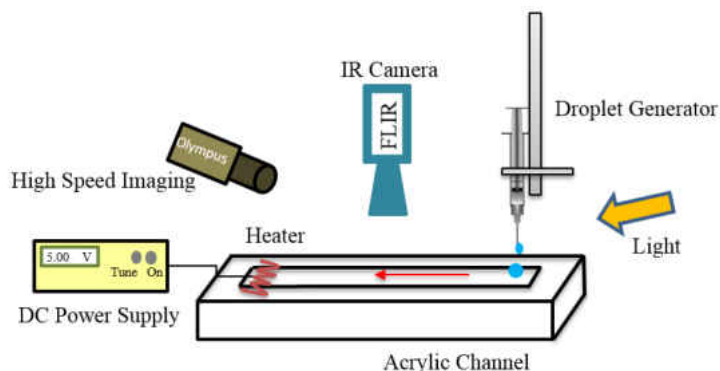


Figure 2.1: Schematic of experiment set-up.

Infrared thermal imaging measurement technique provides spatially and temporally resolved temperature of surfaces non-invasively. The infrared camera (SC 5000, FLIR) used in this study works based on InSb (Indium Antimonide – narrow band gap semiconductor sensor) with a spectral response range of $2.5\mu\text{m} - 5\mu\text{m}$ in wavelength. The detector array provides a 640×512 pixel digital image where each pixel is $15\mu\text{m} \times 15\mu\text{m}$. The temperature range used in the current experiment is $25\text{-}60\text{ }^\circ\text{C}$ and this uses an integration time of 1.17ms . The IR camera was operated at 100 fps with measurement accuracy of $\pm 1\text{ }^\circ\text{C}$. The IR camera captures surface temperature of the liquid depending on the intensity of thermal radiation recorded by the infrared sensor within the camera. The emissivity of the surface can be input into the software used for data processing. The emissivity used was 1.0 . For a change of emissivity of ± 0.03 , temperature changes by $0.3\text{ }^\circ\text{C}$. Through Fourier Transform Infrared Spectroscopy (FTIR) it was confirmed that the absorption coefficient does not change by more than 1% for the fluids used in this study. A set of precision dispensing needles with various tip size (36G - 23G) were used to release pendant

droplets of deionized water manually on the surface of FC-43. The physical properties of the fluids used in the experiments are given in Table 2.1.

Table 2.1: Physical properties of aqueous droplet and the fluorocarbon carrier liquid at room temperature.

Liquid	ρ [g/cm ³]	ν [centiStoke]	k [W/m°C]	β [10 ⁻³ ·(1/°C)]	σ [10 ⁻³ ·(N/m)]	$d\sigma/dT$ [10 ⁻³ ·(N/m)/°C]
FC-43	1.88	2.8	0.066	1.2	16	-0.099
Water	1	1	0.58	0.21	71	-0.2
FC-43 /Water	-	-	-	-	52	-0.14

Infrared thermal imaging measurement technique provides non-invasively resolved spatial and temporal temperature on fluid surfaces. This technique is used to make temperature measurements in the current study of thermocapillary migration of droplets on a free liquid surface. When a droplet is released from a certain height from the liquid surface, it can sustain the impact, preserve its spherical shape, and levitate on the surface. When one end of the test section is heated, Marangoni convection sets up a temperature gradient on the surface, which causes a surface tension gradient at the interface. This creates deformation of liquid surface with a downhill slope towards the maximum temperature. The spherical drops migrate from cold towards warmer regions against Marangoni convection and move towards the heated surface where maximum depression occurs. Despite the counter-current motion of the surface, the droplet moves down the surface slope due to gravity at a much higher speed than it would on a solid substrate. Increasing the thermal gradient leads to higher drift velocities for droplets

of the same size. The IR images (Fig. 2.2) show that the droplet increases in temperature as it moves towards the heater, but stays at a significantly lower temperature than the ambient.

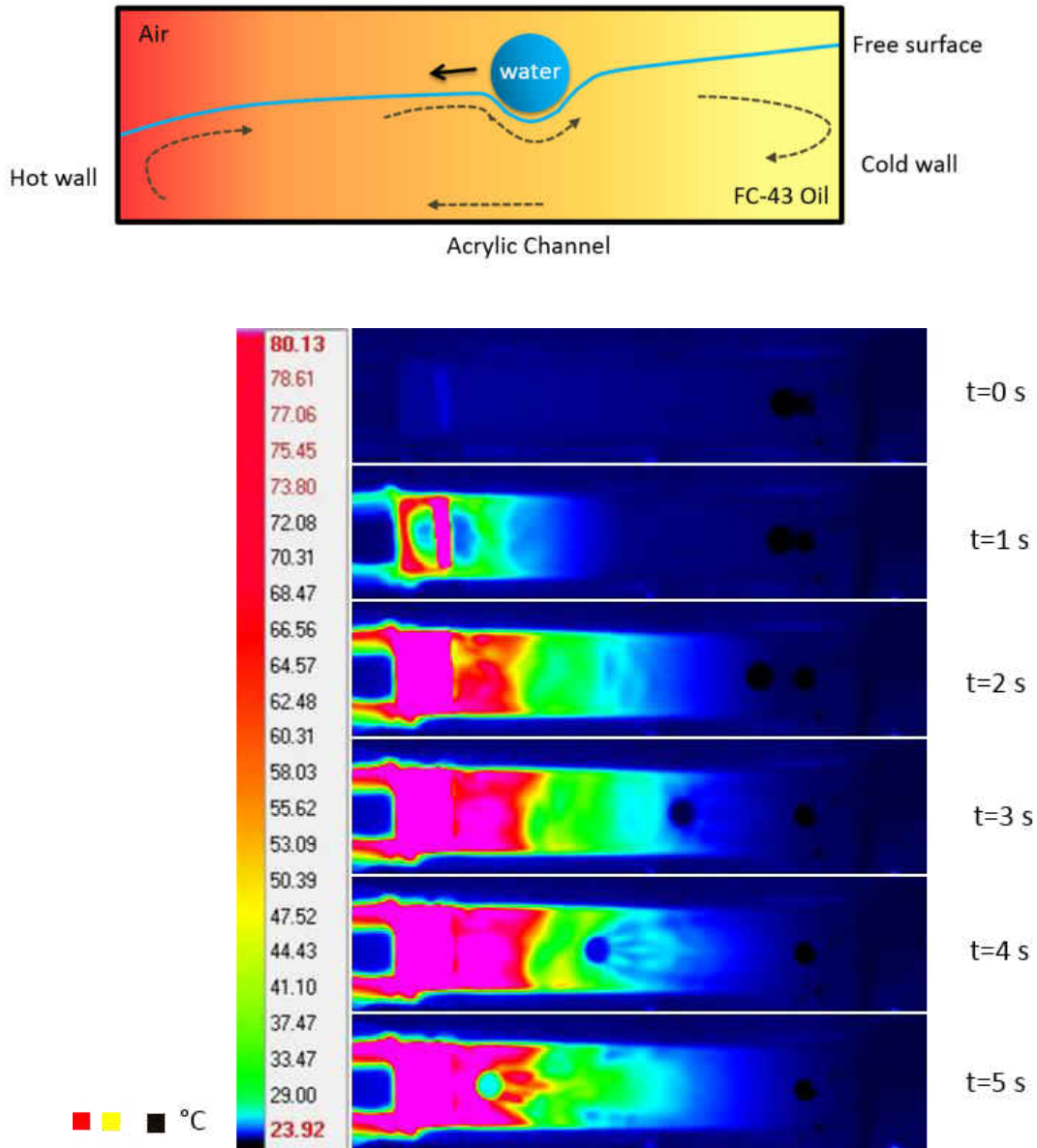


Figure 2.2: (Top) Schematic illustration of counter-current motion of a levitated droplet against the Marangoni flow. The dashed lines depict the Marangoni circulation inside the thin liquid (FC-43) film with a thickness of 2 mm. (Bottom) Motion of a levitated droplet ($d=1.5$ mm) toward the warmer region captured at 100 fps with IR camera. Average velocity was measured at 12.2 mm/s using sequential pictures from a high-speed camera at 2000 fps. The imposed thermal gradient is 0.89 °C/mm.

2.3: Results and discussion

2.3.1: Experimental levitation of spherical droplets

Some preliminary experiments were done to levitate a spherical droplet on a liquid surface and preserve its shape (Yakhshi-Tafti et al. 2010b). When the water droplet is released from a certain critical height, it is able to retain its spherical shape, while the liquid sheet below the droplet stretches. In order to create spherical droplets at the air-liquid interface, they were released as free falling droplets on to the liquid surface from different heights. Upon impact, an air gap develops between the drop and the surface that sustains the weight of the droplet. The entrainment and drainage of air in the thin gap between liquids is due to the relative motion of the fluid interfaces, which, in turn, is generated due to surface tension gradients across the interfaces. It has been shown that a droplet can be kept floating on the surface of a liquid pool by maintaining a temperature difference between the droplet and the liquid pool (Basu and Gianchandani 2007). Bearing action drags air in between the drop and liquid surface and the resultant pressure build-up supports the drop. Generally, non-coalescence of droplets is attributed to the existence of an air gap (Davanlou and Kumar 2015a; Thoroddsen et al. 2003; Sreenivas et al. 1999). Through thermocapillary effects or vibration effects (Gilet et al. 2007), a droplet can be kept levitating on the surface of a liquid pool. The fact that an active external source is required to prevent the droplet from collapsing into the underlying pool suggests that the air gap is continuously drained and replenished.

In this study, not only is the drop levitated above the liquid pool without collapsing or immersing but also is propelled by the imposed thermal gradients in the desired path. Thus, the pressure buildup due to entrainment of flow and the relative motion of fluidic interfaces

explains the longevity of the levitated droplets. Based on simple solutions to energy equation which show exponential decay in temperature, the current temperature field was normalized and curve-fitted to take the form of an exponentially decaying function: $\theta = a \cdot \exp(bx)$; typical values for coefficients from the current experimental data are $a = 1$ and $b = -1.7$. As shown in Fig. 2.3, the thermal gradient drops gradually away from the heater.

Experiments were carried out for migration of spherical droplets 3mm (volume $\sim 14 \mu\text{L}$) in transient and steady thermal gradient conditions. The temperature differences along the channel were 25° , 15° , 10° and 5°C . In transient condition, the platform was initially at room temperature ($\sim 19^\circ \text{C}$) and the heater was turned on and the thermal gradient experienced by the droplet was recorded by evaluating the curve fitted to temperature measurements along the motion path. The droplet does not move until it senses the thermal gradient. The droplet motion can be tuned to any temperature range as long as the required gradients are maintained. The droplet accelerates as it approaches steeper gradients of temperature, while moving towards the maximum temperature on the platform. The surface droplet temperature rises as it approaches the high temperature regions of the thermal gradient, as shown in Fig. 2.3a. This rise is more significant if droplet size is smaller or the conductivity of carrier liquid is higher. In order to develop a better understanding of the effect of thermal gradient and droplet size on the thermally-induced motion of spherical droplets, the problem was studied using steady thermal gradients. Four temperature profiles on the surface were measured by the IR camera (Fig. 2.3a) and the gradients computed (Fig. 2.3b).

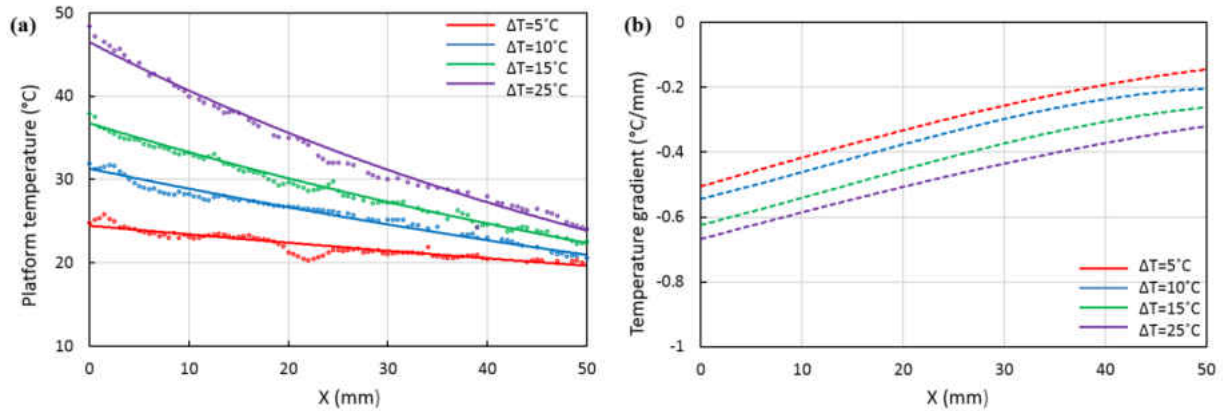


Figure 2.3: Motion of a spherical drop (3 mm diameter). a) Steady temperature distribution along the platform from the IR-camera, b) The corresponding thermal gradient which causes spherical drops to get attracted to higher temperature regions.

In the plots generated hereinafter, the origin is the heater location and X is the distance from the heater. Droplets follow the downhill surface slope towards the hottest extreme of a thermal gradient formed on the liquid platform where the free surface is most depressed. Equal-sized spherical droplets were dispensed at the cold end of the temperature gradient. Droplets accelerated in the direction of increasing temperatures. It was seen that the droplets subjected to higher ΔT 's gained higher drift velocities. These droplet velocity profiles are shown in Fig. 2.4 and later compared to the theoretical model.

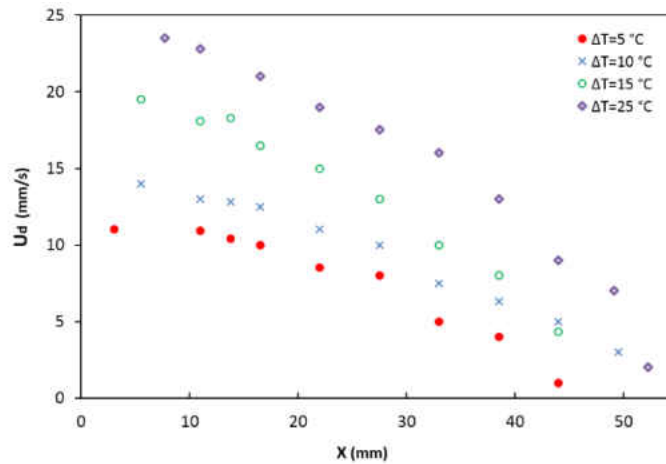


Figure 2.4: Experimental droplet velocity for a 3mm diameter droplet along the channel. Thermal gradients cause spherical drops to get attracted to high temperature regions. Steeper temperature gradient leads to higher droplet velocity along the axis.

In the next section, motion of droplets at the free surface of a thin liquid layer due to a lateral thermal gradient (Fig. 2.5) is modeled and compared to the experimental results.

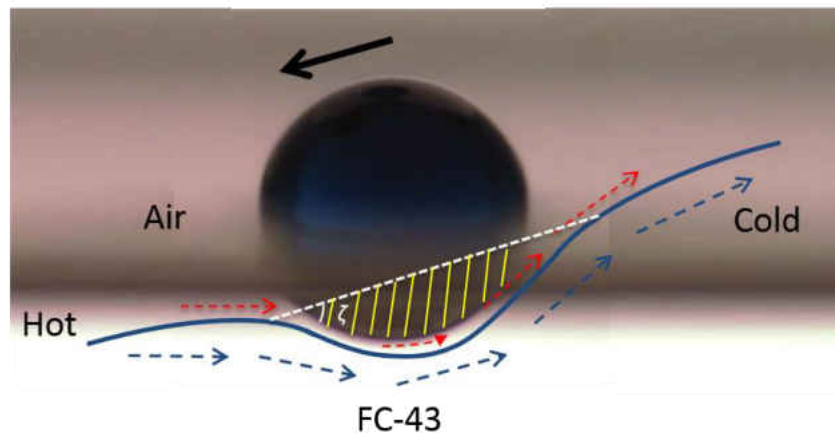


Figure 2.5: Photograph of the levitated droplet merged with the schematic. Deformation and airflow generated at the free surface of a thin immiscible liquid layer (exaggerated for clarity) propels a levitated droplet towards the hotter end of the test section.

2.3.2: Theoretical model for Marangoni convection in thin film

The solution methodology for motion of levitated droplets is divided into two parts. (1) Marangoni convection flow without the droplet, where the deformation slope on the liquid surface and surface velocity are solved. (2) These expressions of surface velocity and surface deformation are used in a separate first order differential equation to solve for droplet velocity. The free surface deforms such that the maximum depression occurs at the maximum temperature location and an outward moving flow develops on the free surface that carries fluid from the hot end to the cold extreme of the thermal gradient. This Marangoni convection problem without a droplet sitting on the surface was also discussed by Pimpitkar and Ostrach (1980) using the assumptions of high aspect ratio. Here, we solve the problem without using the high aspect ratio (thin liquid film) assumption. The governing dimensional equations used in this study are:

Continuity:

$$\frac{\partial u}{\partial x} + \frac{\partial v}{\partial y} = 0 \quad (2.1)$$

x - momentum:

$$\frac{\partial u}{\partial t} + u \frac{\partial u}{\partial x} + v \frac{\partial u}{\partial y} = - \left(\frac{1}{\rho} \right) \frac{\partial p}{\partial x} + \nu \frac{\partial^2 u}{\partial x^2} + \nu \frac{\partial^2 u}{\partial y^2} \quad (2.2)$$

y - momentum:

$$\frac{\partial v}{\partial t} + u \frac{\partial v}{\partial x} + v \frac{\partial v}{\partial y} = -g - \frac{1}{\rho} \frac{\partial p}{\partial y} + \nu \frac{\partial^2 v}{\partial x^2} + \nu \frac{\partial^2 v}{\partial y^2} \quad (2.3)$$

Energy equation:

$$\frac{\partial T}{\partial t} + u \frac{\partial T}{\partial x} + v \frac{\partial T}{\partial y} = \alpha \left(\frac{\partial^2 T}{\partial x^2} + \frac{\partial^2 T}{\partial y^2} \right) \quad (2.4)$$

These equations are normalized using the following scales to elucidate the roles of the different non-dimensional physical and geometric parameters. However, only the dimensional equations (2.1) through (2.4) with the appropriate boundary conditions are solved.

$$x^* = \frac{x}{L}, \quad y^* = \frac{y}{D}, \quad h^* = \frac{h}{D}, \quad A = \frac{D}{L}, \quad u^* = \frac{u}{U}, \quad v^* = \frac{v}{U.A}, \quad t^* = \frac{t}{\tilde{\tau}}, \quad \theta = \frac{T - T_C}{T_H - T_C}$$

$$p^* = [p - p_{atm} - \rho g(h - Y)]. \left(\frac{\mu U L}{d^2} \right)^{-1}$$

$$\text{where } U = \left| \frac{\partial \sigma}{\partial T} \right| A (T_H - T_C) \mu^{-1} \quad (2.5)$$

and $\tilde{\tau} = \frac{L}{\bar{v}}$ are the velocity scale and time scale respectively, A is the aspect ratio ($A = D/L$), and h is the interface height. Next the non-dimensional numbers that emerge upon normalizing are defined as:

$$\text{Bondnumber, } Bo = \frac{\rho g L^2}{U \mu} A \quad (2.6)$$

$$\text{Reynolds number, } Re = \frac{UL}{\nu} \quad (2.7)$$

$$\text{Marangoni number, } Ma = \left| \frac{d\sigma}{dT} \right| \frac{1}{\mu \alpha} L (T_H - T_C), \quad (2.8)$$

where α is the thermal diffusivity and ν is the kinematic viscosity.

$$\text{Prandtl number, } Pr = \frac{\nu}{\alpha} \quad (2.9)$$

The final non-dimensional governing equations are given as follows:

$$\partial u^*/\partial x^* + \partial v^*/\partial y^* = 0 \quad (2.10)$$

$$(d^2/v^* \cdot \tilde{\tau}) \frac{\partial u^*}{\partial t^*} + Re \cdot A^2 \left(u^* \frac{\partial u^*}{\partial x^*} + v^* \frac{\partial u^*}{\partial y^*} \right) = -\frac{\partial p^*}{\partial x^*} - Bo \cdot A^2 \frac{\partial h^*}{\partial x^*} + A \frac{\partial^2 u^*}{\partial x^{*2}} + \frac{\partial^2 u^*}{\partial y^{*2}} \quad (2.11)$$

$$(d^2 A^2 / v^* \cdot \tilde{\tau}) \frac{\partial v^*}{\partial t^*} + Re \cdot A^4 \left(u^* \frac{\partial v^*}{\partial x^*} + v^* \frac{\partial v^*}{\partial y^*} \right) = -\frac{\partial p^*}{\partial y^*} - Bo \cdot A^2 \frac{\partial h^*}{\partial y^*} + A^4 \frac{\partial^2 v^*}{\partial x^{*2}} + A^2 \frac{\partial^2 v^*}{\partial y^{*2}} \quad (2.12)$$

$$(d^2 p^* r / v^* \cdot \tilde{\tau}) \frac{\partial \theta}{\partial t^*} + Ma \cdot A^2 \left(u^* \frac{\partial \theta}{\partial x^*} + v^* \frac{\partial \theta}{\partial y^*} \right) = A^2 \frac{\partial^2 \theta}{\partial x^{*2}} + \frac{\partial^2 \theta}{\partial y^{*2}} \quad (2.13)$$

As mentioned earlier, only the dimensional equations (2.1) through (2.4) are solved. The non-dimensional equations (2.10- 2.13) show the role played by the thin liquid film (low aspect ratio) which would allow for possible simplification.

The main quantities sought from this model are dh/dx and the surface velocity, which will be used later in the second part of the modeling to obtain the velocity of the droplet that is levitated on the liquid surface. Also note that only in a thin layer of h , dh/dx will be prominent. The computational domain is rectangular with an equal amount of FC-43 and air volume above it, as shown in Fig. 2.6.

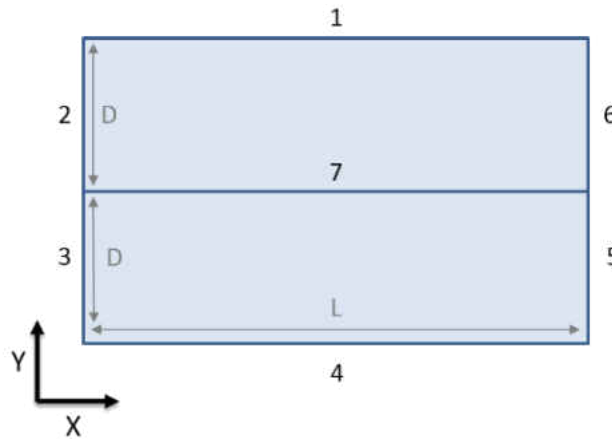


Figure 2.6: Computational domain.

The equations (2.1) – (2.4) are solved using the following initial conditions

$$t = 0: \quad u = 0; v = 0; T = T_C; h = D,$$

and the boundary conditions are given in Table 2.2.

Table 2.2: Boundary conditions.

Boundary	Boundary conditions
Wall 1	No Slip Thermal insulation: $-n \cdot (-k\nabla T) = 0$
Wall 2	No slip Thermal insulation: $-n \cdot (-k\nabla T) = 0$
Wall 3	Wetted Wall; Contact angle (Θ_w) Slip Length (β) $T = T_H$
Wall 4	No slip Thermal Insulation; $-n \cdot (-k\nabla T) = 0$
Wall 5	Wetted Wall; Contact angle (Θ_w) Slip Length (β) $T = T_C$
Wall 6	No slip Thermal Insulation
Wall 7	Moving Interface

The governing equations and boundary conditions for the fluid flow were implemented numerically using the commercial software package COMSOL Multiphysics. The two-phase laminar flow level-set method was used (similar to Son 2014) to capture the moving interface shared between the two fluids, and provides one additional conservation law to the governing equation as follows.

$$\frac{\partial \phi}{\partial t} + \nabla \cdot (u\phi) = \lambda \nabla \cdot (\eta \nabla \phi - \phi(1-\phi) \frac{\nabla \phi}{|\nabla \phi|}) \quad (2.14)$$

ϕ , λ , and η are the level-set variable, re-initialization parameter, and interface thickness, respectively. The level-set function (ϕ) prevents any discontinuities by assigning a dimensionless value between zero and one to each location within the domain at any given time step. This value represents the absolute volume fraction of each of the two phases at that specific grid node. When a location is chosen in the bulk of fluid 1 at a given time, the level-set function will be equal to zero. Conversely, at that same time instant in fluid 2, the level-set function will be equal to one. At the interface, the level-set function transitions from 0 to 1 in a continuous manner dependent on the interface thickness parameter (η). This parameter is typically set to be half the size of the largest element to prevent inaccurate representation of the interface. The profile is typically that of a smoothed step function. The function is also used to maintain continuity among all the physical material properties at the interface, and is implemented by modifying these properties to include the level-set function as follows:

$$\text{Density} \quad \rho = \rho_1 + (\rho_2 - \rho_1)\phi \quad (2.15)$$

$$\text{Viscosity} \quad \mu = \mu_1 + (\mu_2 - \mu_1)\phi \quad (2.16)$$

where the numbered subscripts denote phases 1 and 2, respectively (Olsson et al. 2007).

In order to represent the real physics on side walls of the acrylic channel (walls 3 and 5) which are in contact with FC-43, the contact angle is measured using the dynamic sessile drop method. The measured value was 137° with precision of $\pm 2^\circ$. The slip length was chosen to be equal to the mesh element size. The two-dimensional two-phase flow problem along with the above initial and boundary conditions for FC-43 with the overlying air layer is solved using COMSOL. The simulation contains two physical nodes 1) Heat transfer in fluids and 2)

Laminar two-phase flow, level set. The initial interface node in level set is used to define the initial position as a boundary condition on interior boundaries. During the initialization step, this boundary condition sets the level set function to 0.5. In the regions of interest, i.e., at the air/liquid interface and side walls a very fine mesh is applied (triangular with 65,000 elements). All fluids are considered incompressible and the temperature discretization is linear.

The simulation profiles of surface velocity given in Fig. 2.7 shows the extent to which the free surface velocity increases with temperature difference. At $X = 0$, the closest point to heater, the free surface height undergoes maximum depression. At the other end, $X = l$, the free surface displays the maximum height. Overall, four temperature gradients were applied across the channel and for each case the free surface profile and velocity were calculated. COMSOL calculates the volume fraction that needs to be converted to appropriate values of height. Volume fraction of each constituent (φ_i) is defined as the ratio of that constituent volume (V_i) to the volume of all constituents (V_{total}). Each of the phases is considered to have a separately defined volume fraction that sums up to unity.

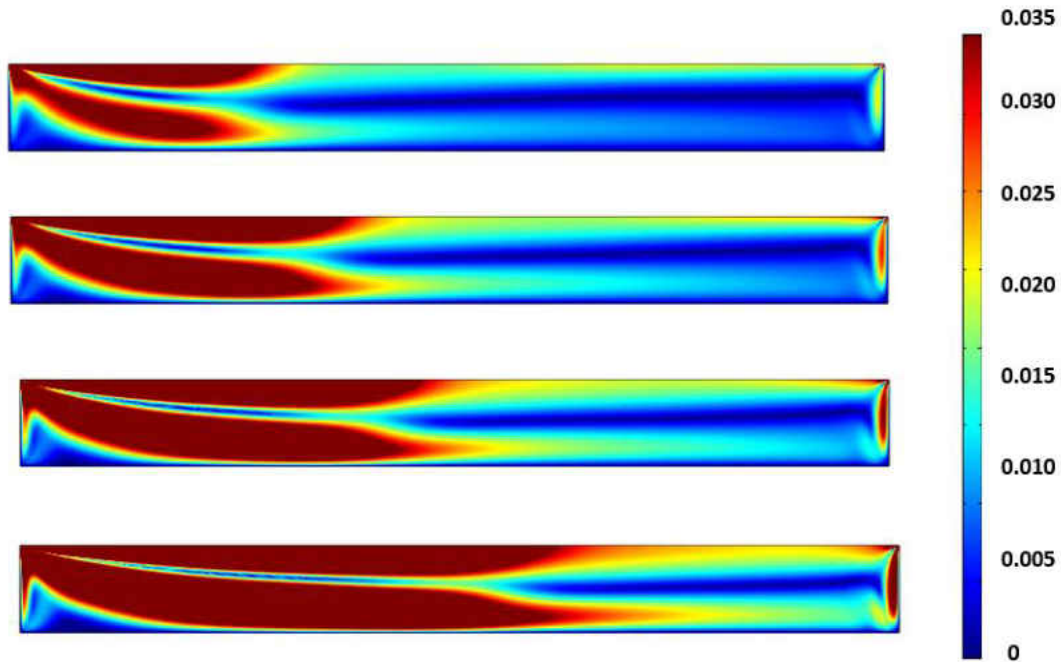


Figure 2.7: Surface velocity magnitudes (m/s) for the steady state case (from top to bottom); $\Delta T=5$ °C, $\Delta T=10$ °C, $\Delta T=15$ °C, $\Delta T=25$ °C. The colors represent velocity in m/s.

Fig. 2.8 shows the free surface velocity profiles from the numerical solution. Higher temperature difference leads to a higher surface velocity and larger surface depression near the heater. The surface velocity increases as ΔT increases in the channel towards $X=0$.

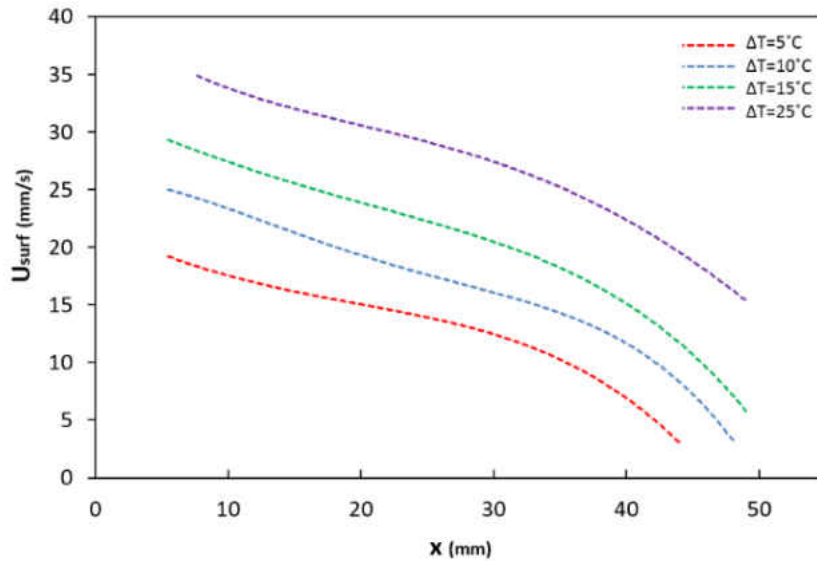


Figure 2.8: Numerical solution: free surface velocity variation along X for four temperature differences.

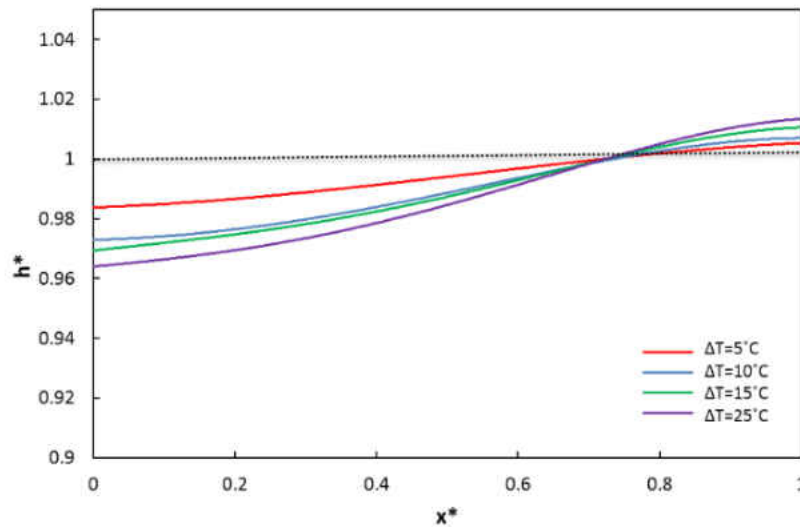


Figure 2.9: Non-dimensional free surface profile at steady state for various temperature gradients.

Figure 2.8 shows the local variation of the surface depth along the length of the channel at steady state in the numerical simulation. In order to plot this graph, the length of the channel is divided into 400 sections. In each of these sections, the volume fraction is converted into height and the best curve fit (within $R^2 \sim 0.99$) for all these points is obtained. The depression is

predicted by the numerical model in Figure 2.9 at steady state for $\Delta T=10\text{ }^{\circ}\text{C}$. In addition to the surface deformation, an outward moving flow develops near the surface. The free surface remains distorted as a balance between the viscous stress due to flow and the shear stress generated due to surface tension gradient. The flow develops from a Couette-like flow to a recirculation flow as time progresses. The warmer liquid close to the heater has lower surface tension and gets pulled towards the cooler liquid surrounding it which has a higher surface tension. During steady state, a recirculation cell forms. Figure 2.9 shows the surface deformation profile embedded onto the actual velocity vectors obtained using the COMSOL software for $\Delta T=10\text{ }^{\circ}\text{C}$ (Case 2 in Table 2.3).

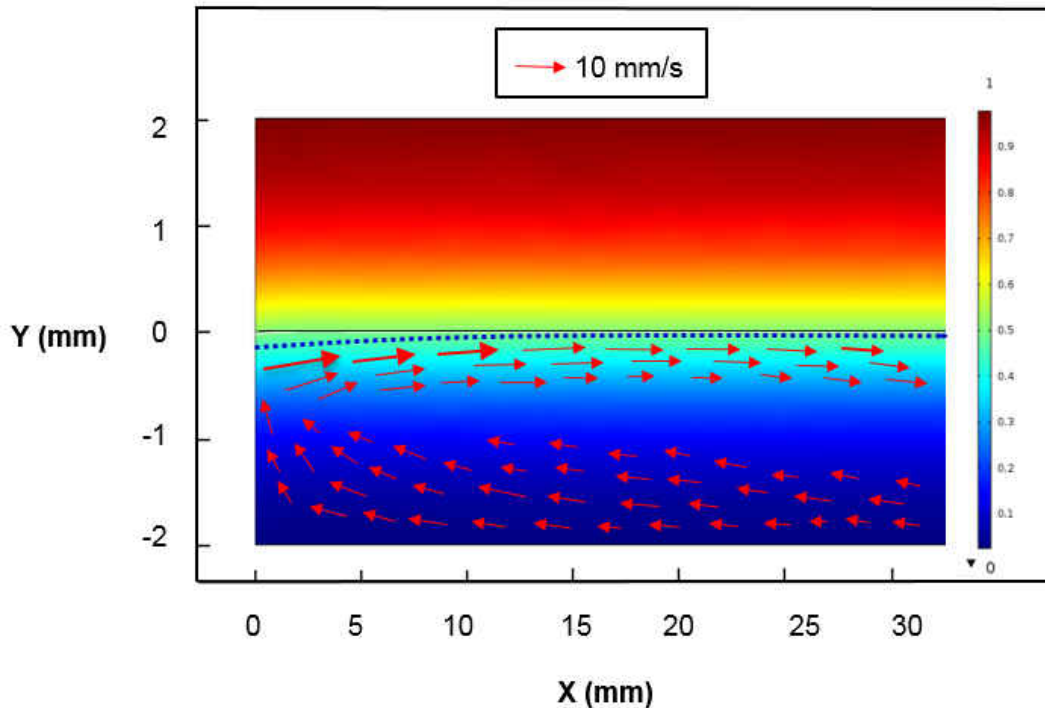


Figure 2.10: Deformation of the free surface due to an imposed thermal gradient (case 2 in Table 2.3) is shown in dotted blue line. The circulation results from Marangoni effects inside the carrier liquid and the arrows depict the velocity field where the average surface velocity for this specific temperature is 17 mm/s. *Note that the y-axis is stretched to show better clarity while the x-axis is limited to only 30 mm.*

The major outcomes that are predicted by the current model in this section are *deformation of the free surface and fluid velocity at the free surface*. In this first part of the solution procedure, Marangoni convection was solved for the given temperature differences in the current geometry, and expressions for surface velocity and dh/dx were obtained. These quantities, provided as functions of x , can now be normalized and used in the equation developed to solve for the levitated spherical droplet on the deformed surface of the thin liquid layer subject to lateral thermal gradients.

2.3.3: Model for the motion of levitated droplets

The attraction of the levitated droplets in the direction of increasing temperature can be explained based on the surface slope and the effect of gravity. Thermal gradients cause surface tension gradients at the free surface, causing deformation of the free surface with a downhill slope towards the maximum temperature, where maximum depression occurs as seen in section 2.3.3. Thus, droplets that are resting above the interface move down the surface slope due to gravity against Marangoni convection. The minimum temperature difference in the channel to levitate drops was found to be 5 °C. Lower values of temperature gradient cannot deform the free surface significantly that would move the droplet toward hotter regions. Low thermal conductivity as well as low ratio of surface tension gradient to temperature gradient of the liquid layer could be considered as the main reasons. In this problem, as the droplet advances towards the heater, it faces the liquid partly and the air partly (Figure 2.5). The drag force on the droplet due to air is negligible compared to that exerted by the liquid.

A simple analysis shows that the spherical droplet should indeed migrate down the free surface slope due to gravity. The droplet acceleration can be attributed to the free surface slope,

$dh^*/dx^* = \tan(\zeta) \sim \sin\zeta$ (for small slopes) where ζ is the angle the free surface makes with the horizon (see Figure 2.5). Droplet motion is affected by gravity and the opposing viscous drag exerted by the liquid front from the underlying FC-43 layer. From a force balance,

$$ma = -mg \sin \zeta + C_D \left(\frac{1}{2} \rho_f S \right) v_{rel}^2, \quad (2.17)$$

where a is the acceleration of droplets, m is drop mass, v_{rel} is the relative velocity of the droplet with respect to fluid velocity, g is the gravitational acceleration, ρ_f density of liquid film (FC-43), u_{surf} is the free surface velocity, u_d is the droplet velocity and S the exposed area of the droplet to the oncoming flow. The drag coefficient C_D is defined as:

$$C_D = \frac{2F_d}{\rho_f v_{rel} S} \quad (2.18)$$

F_d is the drag force. Writing $a = u_d \frac{du_d}{dx}$, eq. 2.17 can be rewritten as a first order differential equation for droplet velocity:

$$\frac{du_d}{dx} = -g \cdot \frac{dh}{dx} \frac{1}{u_d} + \frac{C_D}{m} \left(\frac{1}{2} \rho_f S \right) \frac{(u_d + u_{surf})^2}{u_d} \quad (2.19)$$

Note that dh/dx and u_{surf} are functions of x . Although the droplet is levitated and is surrounded by a very thin layer of air, macroscopically it has been assumed that a portion of the immersed droplet actually sees an oncoming the liquid substrate. The error due to this assumption is not significant. As seen in Fig. 2.5 of the levitated drop, the exposed area for the calculation of drag is a fraction of the total droplet frontal area. This is because the drop, while levitated, creates an obstruction in the thin layer to the oncoming flow. Hence, this

fraction can be represented by the parameter, f . Based on the images from experiments, the exposed area ($=f\pi R^2$) is marked by yellow hatched lines. For example, for a water drop (3 mm diameter) at the air interface of FC-43, $f \approx 0.2$. Experiments for $\Delta T = 5\text{-}25$ °C showed that for the same size droplet, the variation in f was not significant. The value of f was obtained by averaging 50 images. Normalizing eq. (19) using length and velocity scales established in Section 2.3.2,

$$\frac{du_d^*}{dx^*} = -C_1 \frac{dh^*}{dx^*} \frac{1}{u_d^*} + C_2 \frac{(u_d^* + u_{surf}^*)^2}{u_d^*}. \quad (2.20)$$

The dimensionless constants are

$$C_1 \equiv \frac{gAL}{U^2} = \frac{A}{Fr^2}, \quad (2.21)$$

Froude number is defined as:

$$Fr = \frac{U}{\sqrt{Lg}}, \quad (2.22)$$

C_2 is the modified drag coefficient given by

$$C_2 \equiv \frac{C_D}{m} \left(\frac{1}{2} \rho_f S \right) L = \frac{3 C_D f L}{8 r_{drop}} \frac{\rho_f}{\rho_{drop}}, \quad (2.23)$$

Eq. (2.20) is a first order differential equation with known values of dh^*/dx^* and u_{surf}^* from the Marangoni convection problem solved in Section 2.3.3. It requires the initial condition of $u_d^* = 0$ at $x^* = 1$. It is solved as an initial value problem in x using the normalized thermal gradients from the experimental conditions in Table 2.3 as prescribed conditions. Eq. 2.20 is non-

dimensional and the solution depends on constants C_1 and C_2 which represent the overall strength of the driving inertial and gravity forces and the retarding drag force. The first parameter C_1 is known since it is based on aspect ratio and Froude number, but the second parameter (C_2) contains the drag coefficient which is not known yet. This equation is solved numerically in the following manner. When the solution procedure begins at $x^*=1$, the drag coefficient is assumed, and fourth-order Runge-Kutta method is used to solve for u_d^* at every step until $x^*=0$ is reached. If the calculated u_d^* value at $x^*=0$ is zero within a tolerance of 10^{-9} , the solution is converged. If not, the iterative cycle continues with a new assumed value of C_D . At convergence, u_d^* is obtained as a function of x^* , and C_D is determined for the prescribed ΔT (and hence for a given Reynolds number).

The droplet velocity profiles from the numerical model were obtained for each of the four cases (see Table 3) in Figure 2.11. Droplets experiencing steeper thermal gradients have a higher drift velocity as they cause steeper slopes on the free surface. These higher gradients also result in smaller drag since the lubrication pressure buildup is directly proportional to the relative velocity at the interface of the fluids. This simple model is capable of predicting the thermally-induced motion of spherical droplets well. The velocity profiles are normalized by the average free surface velocity in Figure 2.12 for each condition given in Table 2.3, suggesting that the surface velocity is an appropriate quantity to normalize the droplet velocity. These four sets of numerical data are plotted together and curve-fitted, and all of numerical results fell into a single unified curve ($R^2=0.97$) with very good comparisons to the experimental data well within reasonable scatter.

Table 2.3: Main parameters of the theoretical-experimental model.

Case number	ΔT (°C)	Re	Bo $\times 10^4$	U (mm/s)	Fr $\times 10^3$	C_D	Average u_{surf} (mm/s)
1	5	3.7	11.07	3.42	4.65	13.1	12.79
2	10	7.3	5.53	6.84	9.31	6.69	16.84
3	15	11	3.69	10.26	13.96	5.2	21.1
4	25	18.3	2.21	17.1	23.27	3.34	26

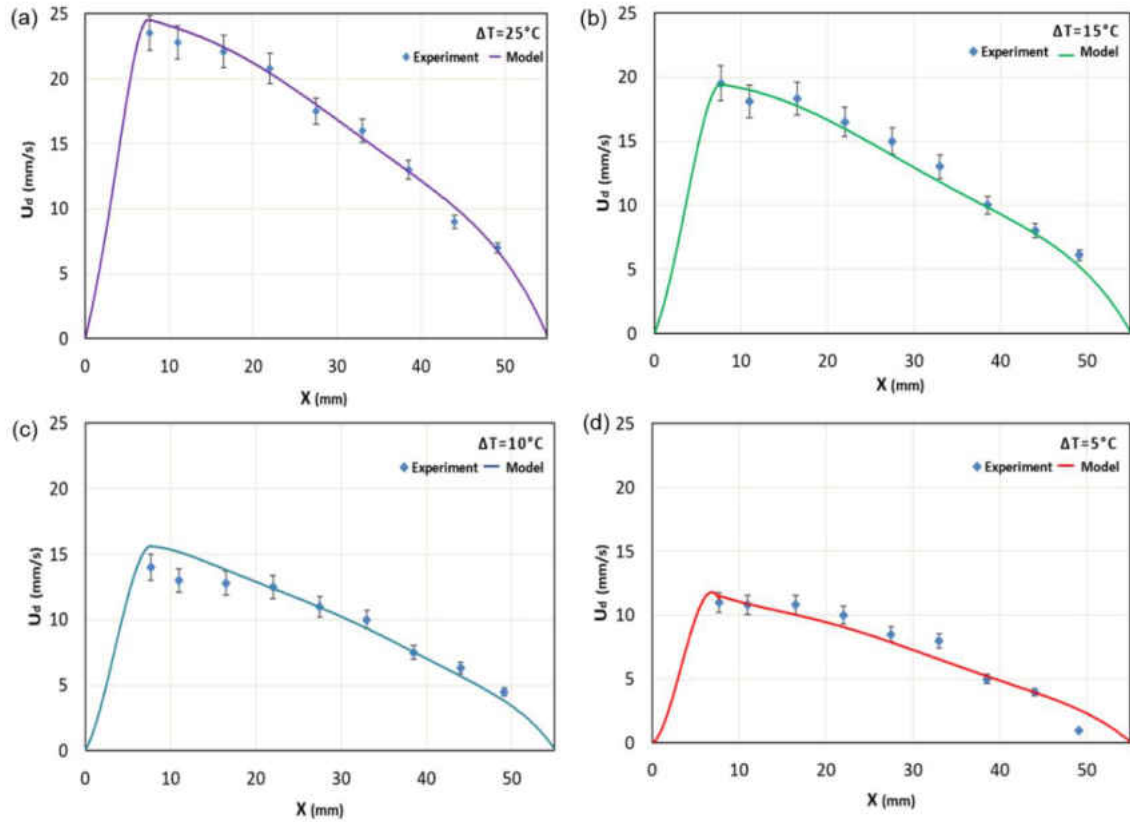


Figure 2.11: Dimensional drop velocity from experiments compared to the model predictions (solid line) for four temperature drops. (a) $\Delta T=25$ °C, (b) $\Delta T=15$ °C, (c) $\Delta T=10$ °C, and (d) $\Delta T=5$ °C.

As the thermal gradient gets steeper, velocity scale increases, Froude number becomes higher, and the drag coefficient, C_D , shows a decreasing trend (Table 2.3). This is so since the drag coefficient is inversely proportional to square of the velocity. This can be further explained by using the outcomes of the levitation pressure model proposed by Savino et al. (2003). Larger thermal gradients result in larger interfacial velocities which in turn result in larger lubrication

pressure buildup that reduces the overall interaction at the fluid interface; hence a lower apparent drag coefficient. Any tendency for the drop and liquid pool in the continuous and disperse phases to come into contact with each other locally, is countered by an increase in the bearing pressure (Sreenivas 1999), which is induced by shear stresses due to the relative motion of the air flowing between these two (Savino 2003). This balances the weight of the floating droplet at the liquid interface as long as the drops are in motion.

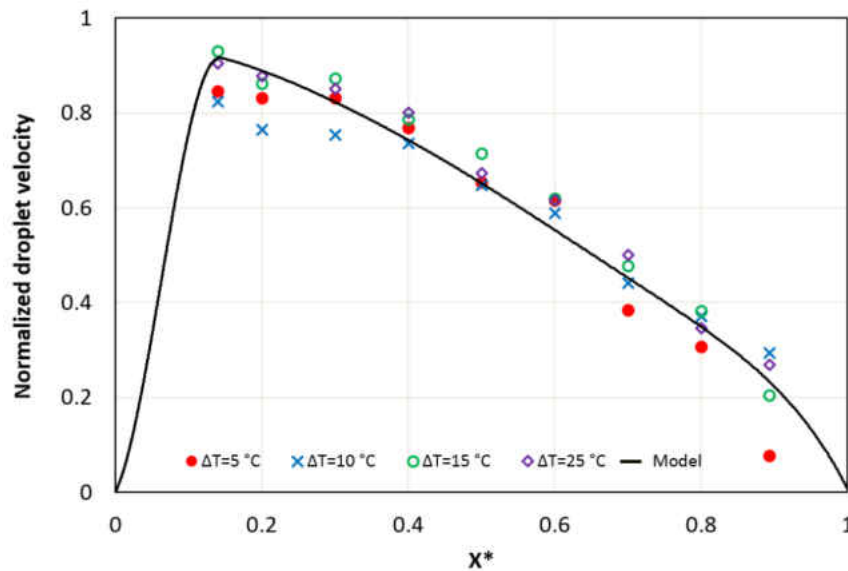


Figure 2.12: Droplet velocity normalized by surface velocity for various temperature drops. Symbols show experimental droplet velocity at the same X^* locations but different ΔT . The solid line is the curve-fit generated from the numerical results for 4 different cases.

Figure 2.13 shows the decrease of drag coefficient with increasing temperature drop in the channel. This can also be casted in terms of drag coefficient (C_D) and Reynolds number (Re_d) which is based on droplet diameter and scale velocity. Running the simulation for various ΔT 's a correlation for the drag coefficient in terms of Reynolds number may be developed as follows:

$$C_D = 29.14Re_d^{-0.71} \quad (2.24)$$

It is interesting to note that the drag coefficient of the levitated droplet for the same Reynolds numbers is about 66% to 22% higher than the fully immersed smooth sphere for a range of Reynolds numbers between 2 and 32. This could be explained based on the effective exposed area of droplet to oncoming flow (here FC-43) which is a part of the sphere which in this case is asymmetric. Thus, moving a levitated droplet against the Marangoni flow requires a larger force that can overcome the additional fluid drag.

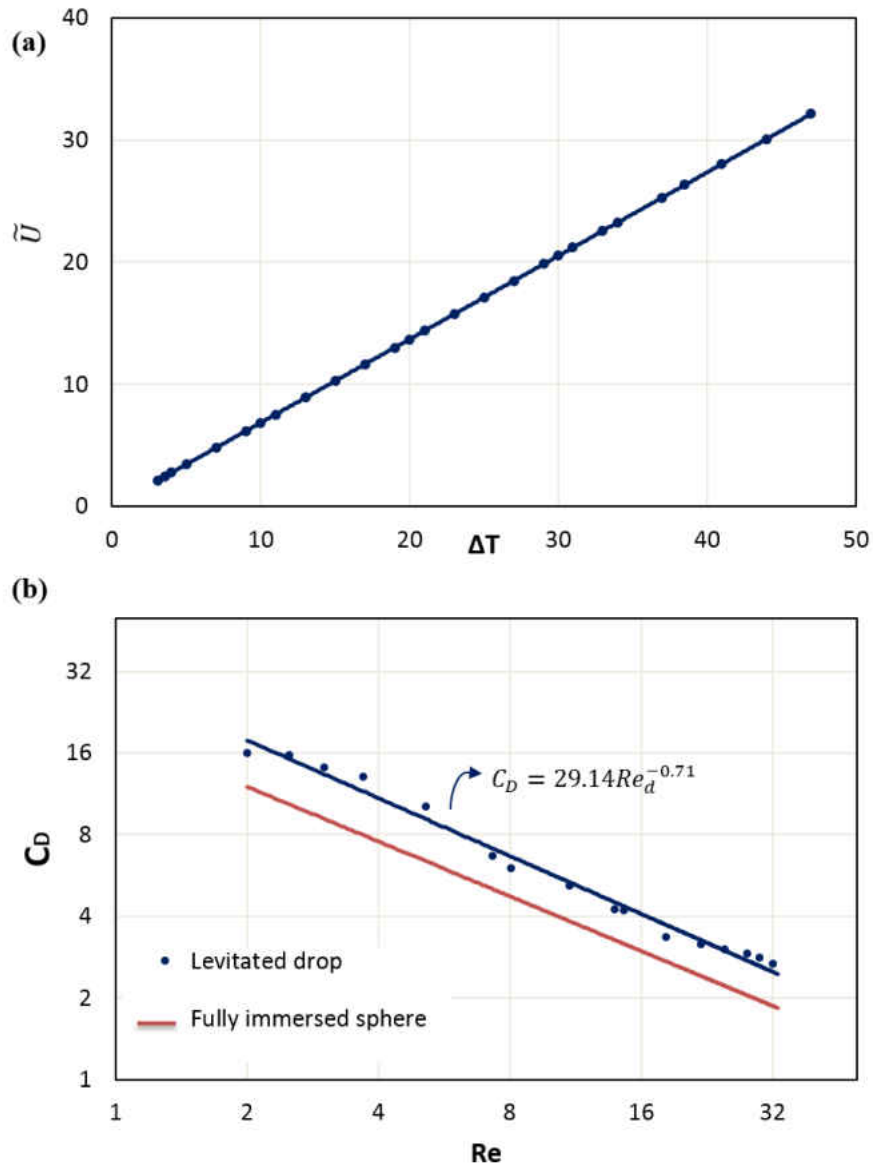


Figure 2.13: (a) Velocity scale variation with temperature drop in the channel, (b) Drag coefficient versus Reynolds number for levitated drop compared with the fully immersed case (Morrison 2013).

2.4: Conclusion

In this work, motion of a spherical droplet on the free surface of a thin liquid layer, caused by lateral thermal gradients, was investigated. While normally occurring lens-shaped droplets

(e.g. water on oil), move in the direction of decreasing temperatures, we showed that levitated droplets move in the opposite direction of Marangoni convection towards increasing temperatures. The droplet stays levitated on the surface since the buildup pressure balances the van der Waals attraction forces between the surface and droplet. When van der Waals forces become dominant, the air cushion in between them shrinks and finally the droplet would penetrate the liquid surface and submerge in the liquid.

The motion of these droplets is primarily governed by the dynamics of the underlying liquid film. When a thermal gradient is maintained across a thin liquid platform, two key phenomena occur: (1) the free surface gets deformed such that the high temperature regions become depressed, and (2) a flow develops on the free surface that carries the fluid from the hot end towards the cold side of the thermal gradient. These phenomena were used to explain the migration of the spherical droplets initially resting at the air-liquid interface of an immiscible liquid, subject to a thermal gradient.

Based on the dynamics of thin liquid films subject to thermal gradients, a theoretical model has been developed. First, the surface velocity and the slope of the depression of the free surface are solved from the governing equations for a Marangoni flow without levitating the droplet. Secondly, a force balance is used for the levitated droplet, which relies on the surface velocity and the surface slope. An iterative solution for the droplet velocity is determined from this equation, which compares well with the experimental velocity for four different temperature gradients. The solution also provides the drag coefficient on the droplet due to the liquid front from the Marangoni flow. This drag coefficient was found to be larger than that for a fully immersed sphere by 66% to 22% for Reynolds number between 2- 32.

CHAPTER 3: LIFETIME OF LEVITATED LIQUID DROPLETS

3.1: Introduction

The interaction of droplets with each other and the impact of them on surfaces have been the focus of many studies. Impinging droplets upon the surface of an immiscible liquid from critical heights above the target liquid can result in spherical-shape droplets that float at the air/liquid interface. It is important to mention that a levitated droplet is not in direct contact with the substrate. In fact a thin air film is between the droplet and the liquid substrate, which supports the droplet weight. When this underlying air film ruptures, the droplet undergoes transition, in which an unstable spherical-shape droplet converts into a stable partially submerged lens-shape configuration. The time that the droplet sits on the surface till the air film breaks and this droplet transforms to the oblate shape is called lifetime. As of yet, many aspects of this type of droplet impact phenomenon has remained unexplored, therefore it seems necessary to further study and deepen our understanding of this complicated problem. Study of levitated droplets is of great importance from application aspect as well. Such droplets show excellent controllability in response to thermal gradients, a property that makes them an interesting choice for sample manipulation.

After dispensing a droplet on a liquid substrate, which acts similar to an elastic membrane, the droplet starts to oscillate on the surface, but stays levitated above the interface (Davanlou and Kumar 2015a; Davanlou et al. 2014; Yakshi-Tafti 2010b)-. The impact behavior depends on physicochemical properties of liquids including density and miscibility of both mediums. One can distinguish 3 distinct scenarios: a) coalescence; if droplet and

liquid pool are of the same fluid, b) spreading; if a droplet of a wetting liquid is lighter than the liquid pool, c) sinking; if a droplet of an immiscible liquid is heavier than the liquid pool. However, in all these cases an overpressure in the air film between the droplet and the liquid interface can help support the weight of the droplet and keep it floating (Savino et al. 2003). The weight of a drop causes a depression at the interface, while the air constantly flows into the gap between the drop and the liquid surface. It is earlier shown that a levitated droplet is not as stable as a submerged droplet. As a result, the thin air film between the droplet and the liquid surface continuously shrinks and finally when it reaches a critical value, the droplet coalesces with the surface and transforms into a submerged droplet (Davanlou et al. 2013). The rupture of the air layer could be attributed to large van der Waals attraction force between the two media. The rupture position depends on the liquid viscosity and the impact velocity (Tran et al. 2013). Nakai et al. (2011) found that without external perturbation, the transition from levitation to submersion happens so quickly that one can hardly observe the droplet floating on the surface. However, it is possible to delay the coalescence and elongate the levitation time with few techniques such as hydraulic jump, vertical vibration of liquid surface or using chemicals like a detergent (Sreenivas et al. 1999). Monti and Dell'Aversana (1994) discovered that a temperature difference could help avoid coalescence between two neighboring droplets. Later, Savino and his group (2003) determined that surface tension gradient on a liquid surface due to temperature difference can result in Marangoni flow in that liquid, which helps the air to flow into the interstice under droplet and maintain the pressure of the air film that supports the droplet. Recently, Lee et al. (2012) used X-ray phase-contrast imaging to visualize the profile of an entrapped air film and its three stage evolution into a bubble during droplet impact. Richard et al. (2002) used high-speed

photography to measure the contact time of a bouncing drop during the shock. They quantified their observations by comparing the kinetic and surface energies of the drop using Weber number. Blanchette et al. (2009) studied the effects of surface tension gradients in coalescence of a droplet with a liquid reservoir of a miscible fluid. According to their results, depending on the reservoir to droplet surface tension ratio, the coalescence may be partial or total.

This paper experimentally investigates the parameters that can affect the lifetime of a non-coalescent droplet at the interface of an immiscible fluid such as droplet size, initial temperature and liquid properties. In this regard, a range of drop sizes of different fluids is generated and tested. The results are compared by developing a theoretical model. The model is in good agreement with experimental data.

3.2: Theoretical Background

When a droplet is released from a certain height, it can overcome the impact, and a spherical droplet will form which is not in direct contact with the pool. A thin layer of air separates the droplet from the carrier liquid (see Fig. 3.1). In the absence of an external perturbation, this film quickly diminishes and ruptures. The entrainment and drainage of air in this gap is attributed to the relative motion of the fluid interfaces, which in turn, is generated due to surface tension gradients across interfaces. The assumption that drainage of air within the thin gap is able to sustain the droplet weight, requires that there be a pressure buildup due to the motion of air within the gap (Gilet et al. 2007). The buildup of pressure due to the motion in the narrow gap between fluid interfaces can be understood and modeled using the theory of lubrication for low Reynolds number flows where the significant parameters are pressure, viscosity and the narrow

gap between the moving surfaces (Panton 1995). Thus, we assume that the air drains in and out of the gap with open boundaries. The time during which the droplet remains floating on the surface depends on the temperature of the droplet and surface. This lifetime is reported to be longer when the temperature difference between the two fluids is larger at the time of dispensing the droplet. In addition drainage time depends on viscosity of the pool liquid, i.e., when the drop weight cannot balance the viscous resistance forces, drainage occurs. By renewing the air film it is possible to keep a droplet levitated. The lifetime is restricted by the bursting of the film. Laser interferometry and infrared thermograph were used to measure the film thickness evolution (Tran et al. 2013). By using monochromatic sodium lamp and utilizing indirect methods, it is found that the bursting occurs, when the film is approximately $0.2 \mu\text{m}$ thick-. This suggests that van der Waals forces become dominant when the film shrinks to a minimum.

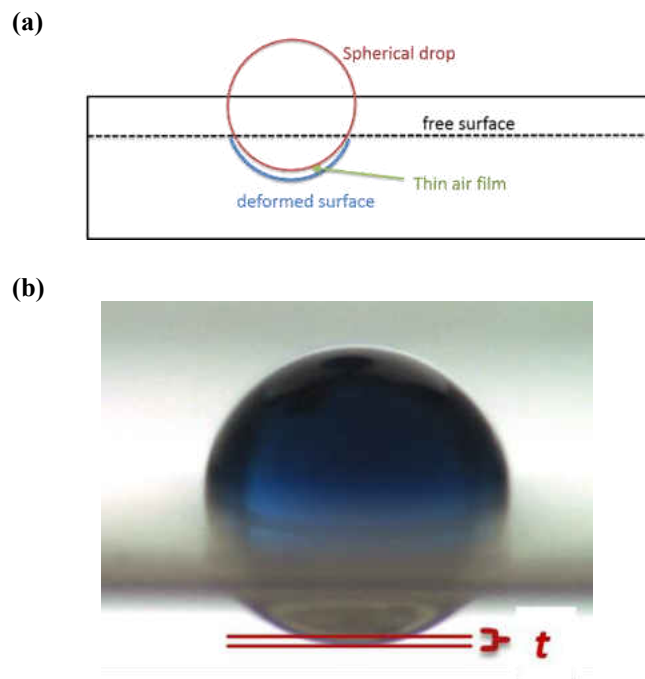


Figure 3.1: (a) Free surface profile of the liquid film in vicinity of the contact line, (b) A levitated drop from the side, the underlying air film is shown in red as t .

3.3: Experimental Work

Figure 3.2 shows the schematic of the experimental setup. In this work, the base medium is FC-43 oil. FC-43 at 20 °C has a density of 1.88 g/cm³, surface tension of 16 mN/m and viscosity of 2.8 cSt. The liquid is clear and non-flammable with melting and boiling points of -50 °C and 174 °C, respectively. Distilled water is used as the dispersed phase. Aqueous droplets with density of 1 g/cm³, surface tension of 71 mN/m and viscosity of 1 cSt are generated by manually pushing a high precision syringe. Silicon oil with a kinematic viscosity of 20 cSt has a density of 0.949 g/cm³ and surface tension of 20.6 mN/m. Different gauge needles are used to generate droplet of different sizes. The uniformity of droplets is monitored by using high-speed imaging (uncertainty of ±0.2 mm). Infrared thermal imaging provides non-invasive spatial measurement of the platform and the droplet (FLIR SC-5000). This device has measurement accuracy of 1 °C and operates in the range of 5-300 °C. A transparent glass container which has 60 cm² cross section and 70 cm height is filled initially with silicon oil and then with FC-43 to study the lifetime of miscible and immiscible fluids. A high-speed digital video camera (Olympus i-speed LT) is set at angle of 45° with respect to the liquid-liquid interface to avoid image distortion and ensure high quality imaging. The container is cleaned with acetone and methanol between experiments.

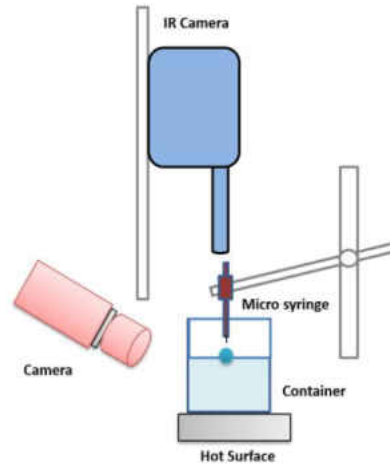


Figure 3.2: Schematic of experimental setup.

Measurement of the liquid surface tension is made by a bubble pressure tensiometer (SITA GmbH). The tensiometer can measure surface tension in a range of 10-100 mN/m and temperature range of 0-100 °C with a resolution of 0.1 mN/m. The surface tension values for the used fluids are tabulated in Table 3.1.

Table 3.1: Surface tension variation with temperature (± 0.1 mN/m).

Temperature (°C)	σ_{FC-43} (mN/m)	$\sigma_{\text{Silicon oil}}$ (mN/m)
5	17.3	24
10	17	23.6
15	16.6	23.1
20	16.2	22.8
25	15.9	22.3
30	15.4	22.2
35	15	21.1
40	14.7	21
45	14.2	20.1
50	13.6	19.6
55	13.3	19
60	12.9	18.6
65	11.4	18
70	11.1	16.5
75	10.9	16
80	10.6	15.6
85	10	15.1

3.4: Results and Discussion

The surface tension imbalance at the liquid/air interface due to temperature difference between the droplet and the pool liquid results in Marangoni motion that hinders the coalescence or submersion of the droplet. The experimental results show that due to the existence of a temperature difference between the droplet and the pool liquid, it is possible to suppress the rupture of the air film between the two media and postpone the coalescence. The induced flow inside the pool is directed towards the droplet which is colder than the pool (higher surface tension), and therefore it pulls the ambient air beneath the droplet. The minimum required temperature difference to avoid coalescence is found to be 2 °C. Figure 3.3 illustrates the transition from levitation to submersion for a liquid droplet floating at the liquid/air interface. Initially, the droplet weight is balanced with the overpressure in the air gap (Fig. 3.3a). As the temperature difference between two media decreases, the air film shrinks gradually (Fig. 3.3b). After steady-state condition is reached, the droplet will either coalesce with the pool if they are of the same fluid, or submerge if they are immiscible as depicted in Fig. 3.3c.

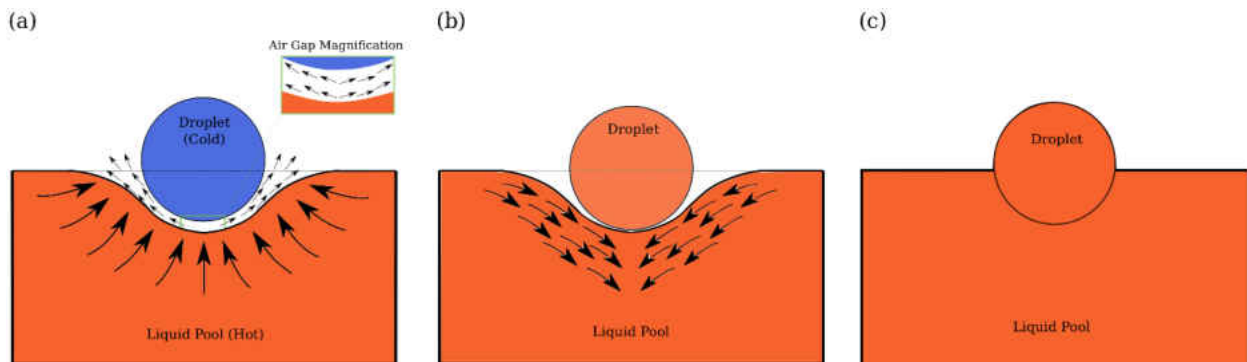


Figure 3.3: Levitation of a liquid droplet on the liquid pool of a distinct immiscible fluid. (a) Droplet floats above the air/liquid interface. The inset magnifies the interstice under droplet where the air gap is present. (b) As the temperature of the droplet rises, the air gap shrinks. (c) After thermal equilibrium, the droplet partially submerges within the pool. The vectors inside the liquid pool show the surface tension forces, while the vectors outside show the air flow. Droplet is 3 mm and $\Delta T= 10$ °C between two media.

For the experiments presented here, a droplet of 3 mm is released from a constant height, 1.5 times the droplet diameter. The temperature of the carrier liquid is varied from 21 - 81 °C, while the droplet temperature is kept constant at room temperature (21°C). Figure 3.4 illustrates the variation of droplet lifetime with temperature for a) water droplets on FC-43, and b) silicon oil droplets on the pool of same fluid. The results represent the average of 50 measurements. Although, temperature difference increases the levitation time of a drop, there is a significant difference between the lifetime of silicon oil droplets and water droplets. One can explain this by comparing the heat capacity of silicon oil and water. The heat capacity of water (4.182 kJ/kg.K) is approximately three times greater than that of silicon oil (1.460 kJ/kg.K), so the temperature of a silicon oil droplet reaches the pool temperature faster, consequently coalescence occurs earlier than for a similar water droplet (Monti and Dell’Aversana 1994). The results also show that the thickness of the pool does not play a role in levitation time of levitated drops. The release height is varied systematically for both heights. These results corroborated the earlier findings that within the critical height the trends in both liquids behave similarly as shown in Fig. 3.4.

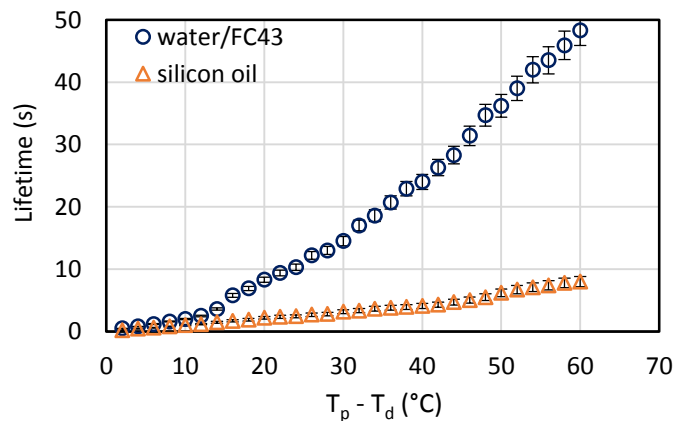


Figure 3.4: Variation of droplet lifetime with temperature for a 3 mm drop released at a height of 4.5 mm above the pool. $T_p - T_d$ is the difference of temperature between the pool liquid and the droplet at the time of landing. Droplet temperature rise will eventually lead to rupture of the air film.

Here, the observations are explained using a simple theoretical model. In order to simplify the problem, a few assumptions are made; a) the possible Marangoni effect inside the droplet is neglected, b) a levitated droplet is a perfect sphere. To avoid coalescence of a levitated droplet with the pool, the total pressure over the contact area between the droplet and liquid surface, S , must be equal to the weight of the droplet, i.e.,

$$\Delta p S = \rho g V \quad (3.1)$$

where ρ is the density of the droplet, g is the gravity acceleration, V is the volume of the droplet, and Δp is the pressure increase that is defined based on the lubrication theory concept (Gilet et al. 2007):

$$\Delta p = \frac{\mu_a v_m}{b^2} R \quad (3.2)$$

v_m is the Marangoni velocity which defined as (Savino et al. 2003):

$$v_m = \sigma_T (T_p - T_d) / \mu_p \quad (3.3)$$

t is the thickness of the air film, R is the radius of the droplet, μ_a is the viscosity of the air and μ_p is the viscosity of the pool. We assume that the contact area is:

$$S = \frac{1}{4} \pi R^2 \quad (3.4)$$

Now, the film thickness can be cast as:

$$t = \sqrt{\frac{3 \sigma_T \mu_a}{16 \rho g \mu_p} (T_p - T_d)} \quad (3.5)$$

Figure 3.5 shows the behavior of the film thickness as the temperature between the pool liquid and the droplet ($T_p - T_d$) changes. Interestingly, the film thickness shows an increase when ($T_p - T_d$) increases. This increase of film thickness for the water droplets floating on FC-43 pool is much faster than silicon oil droplets on its own pool. This result explains the longer lifetime of water droplets compared to the silicon oil. The larger film thickness for the water droplet is due to large difference between water viscosity and silicon oil viscosity (~ 20 times). The air gap is the main reason of drop levitation, and has significant influence on droplet lifetime. It is theoretically shown that temperature has a direct relationship with the film thickness. A droplet remains floating as long as its weight balances the viscous resistance forces.

Even though the developed model is simple, it is capable of explaining the physics of the problem reasonably well. Based on this model the surface tension gradient with temperature, temperature difference between media, density of the droplet and viscosity of the pool are the prominent factors in the film thickness.

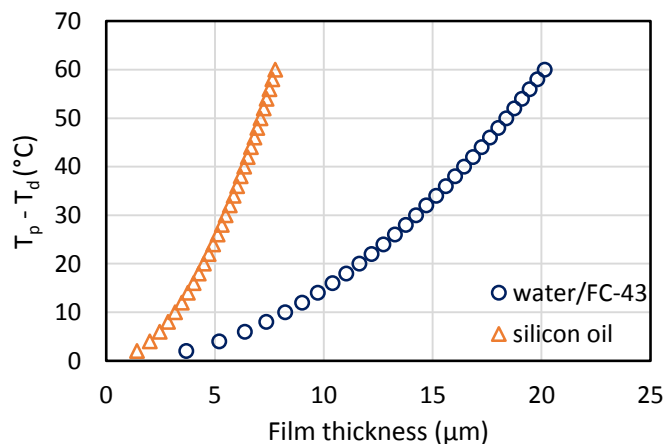


Figure 3.5: Theoretical relationship between film thickness and temperature difference for silicon oil droplets on a silicon oil pool and water droplets on a FC-43 pool.

In addition, consideration of the effect of vapor pressure is important. Generally, the vapor pressure increases with temperature. Here, partial evaporation of droplets due to temperature rise could play a role in increasing the lifetime. At high temperatures, evaporation of both media can form a vapor film between the pool and the droplet surface, thus it is critical to compare the vapor pressure values. At room temperature, water has vapor pressure of 2.3 kPa while a 20 cSt silicon oil has vapor pressure value below 0.13 kPa. Since the water droplet has a larger vapor pressure than silicon oil, it can counteract the gravity force and stay levitated for a longer time.

In order to study the size effect on droplet lifetime, we conducted similar experiments on droplets of various sizes. It is found that the size of a levitated droplet can significantly affect its lifetime. As shown in Fig. 3.6, by increasing the diameter, the lifetime increased monotonically, the reason is it takes a longer time for a larger droplet to reach the pool temperature compared to a smaller droplet. Nevertheless, beyond a certain value ($T_p - T_d \sim 60$ °C), the changes were not significant as in the earlier stage.

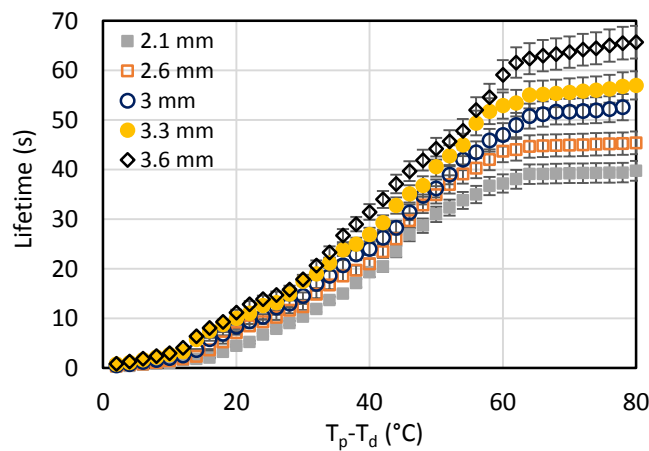


Figure 3.6: Effect of droplet size on its lifetime (droplet: water; pool: FC-43).

3.5: Summary

In this section, the parameters affecting droplet levitation time are investigated experimentally. It is shown that the film thickness increases as the temperature difference between the droplet and the liquid pool increases therefore longer levitation times could be achieved. Comparing water drops with silicon oil 20 cSt shows the importance of heat capacity and viscosity of involved fluids in the life span. The lifetime of water drops is approximately two times greater than silicon oil drops. Additionally, the effect of droplet size is tested. It is found that larger droplets last longer floating at the air/liquid interface than smaller droplets under the same condition. As a larger droplet requires more time to reach the isothermal condition, it should have a longer lifetime. In other words as long as we maintain a temperature difference between two mediums, the weight of the droplet is compensated by the pressure buildup due to the existence of an air gap. Lastly, the possible role of vapor pressure is discussed.

In the future, the aim is to extend the current study to more types of fluids to account for other physicochemical properties that may affect the resting time of levitated droplets, and also take advantage of advanced visualization techniques to detect the air gap variation with temperature and time. Other areas such as drug delivery and lab-on-a-chip devices can potentially benefit from the outcome of this research.

CHAPTER 4: THERMALLY INDUCED COLLISION OF DROPLETS IN AN IMMISCIBLE OUTER FLUID

4.1: Introduction

The emergence and advancement of digital microfluidics have facilitated the design of novel systems that can perform fluidic operations (Squires and Quake 2005). A variety of methods of droplet actuation have been developed including Marangoni convection, dielectrophoresis, electrowetting-on-dielectric (EWOD), acoustic-driven and optoelectrowetting. Among these, Marangoni convection is a promising technique that has gained wide attention for droplet-based microfluidic system. Surface tension gradients on very thin liquid films can set up motion due to unbalanced forces at the interface. This is called the Marangoni effect. The possibility of manipulating droplets in an open structure, contact-free, without droplet pinning and surface contamination are some of major advantages of thermocapillary actuation (Yakhshi Tafti et al. 2010; Zhao et al. 2011). In several applications, drop-drop interactions play a central role in the performance of the system (Christopher 2009). For instance, separation and analysis of components of a mixture, or transport and mixing of chemical reagents to form new compounds are critical to drug delivery. Recently, Javadi et al. (2013) showed the feasibility of fabrication of a bidirectional capillary micropump by engineering the surface properties through electrowetting. So far, droplet interactions in air and collision of droplets on solid surfaces have been studied vastly in the literature. The collision behavior of liquid droplets floating on liquid substrates opens up interesting possibilities and as yet, remains unexplored.

The coalescence of liquid droplets is ubiquitous in nature and is of great interest to wide range of processes, such as rainfall (Rayleigh 1879; Adam et al. 1968; Brazier-smith et al. 1971; 1971; Abott 1973), droplet combustion (Nikolopoulos et al. 2009), ink-jet printing (Soltman and Subramanian 2008), microfluidics (Armani et al. 2005) and separation of emulsions (Hirato et al. 1991). Collision of binary droplets in air is a well-established phenomenon that is studied in depth by different authors (Ashgriz and Poo 1990; Orme 1997; Jiang et al. 1992; Qian and Law 1997; Brenn and Ashgriz 2011; Tang et al. 2012). In a benchmark paper, Qian and Law (1997) reported five distinct regimes of drop-drop interactions for hydrocarbon and water, namely (I) coalescence after minor deformation, (II) bouncing, (III) coalescence after substantial deformation, (IV) coalescence followed by separation for near head-on collisions, (V) coalescence followed by separation for off-center collisions. Based on their results, the droplet velocity, fluid properties and impact parameter were found to be the determining factors in the collision outcome (Orme 1997; Brenn and Ashgriz 2011). In addition, coalescence of sessile droplets on a substrate (sometimes mentioned as confined droplet collision) was the focus of few recent studies, in which the coalescence is realized by condensation, addition of volume to one droplet or using pressurized air (Narhe et al. 2004; Sellier and Treluyer 2009; Karpitschka and Riegler 2010; Nilsson and Rothstein 2011). The focus of these works was the dynamics of meniscus bridge upon early stages of coalescence (Karpitschka and Riegler 2010; Eggers et al. 1999; We et al. 2004), contact angle hysteresis (Nilsson and Rothstein 2011) and timescales (Choi and Lee 2014). Recently, Thoroddsen et al. (2008) and Kavehpour (2015) reviewed the coalescence process of liquid drops on thin liquid layers and dry surfaces. Also wetting and

spreading of fluids on solid surfaces discussed using contact angle, surface heterogeneity and contact lines (Bonn et al. 2009; Gharabaghi and Aghazadeh 2014)

In this dissertation, for the first time, we investigate the coalescence phenomenon of two levitated droplets. When a droplet is released from a certain height (typically 1.5 - 4 times its diameter), it can overcome the impact, preserve its spherical shape, and stay levitated on the surface (Yakhshi-Tafti et al. 2010b; Davanlou et al. 2014). This can be seen in Fig. 4.1 of Non-dimensional release height versus Bond number (Bo) for several droplet diameters in the range of 1.4mm to 3.9mm. This gives rise to Bo in the range of ~ 2 to ~ 10 , i.e., buoyancy force changes from a similar magnitude of surface tension force to an order of magnitude higher. The droplet at higher Bo may not be levitated if it is not released from a height very close to 1.5 times. At high Bond numbers, the droplet may not stay levitated. The levitated droplet is not in direct contact with the free liquid surface due to the existence of an air gap of a few microns thick between two media (Savino et al. 2003; Couder et al. 2005; Tran et al. 2013). A submerged droplet, also called a sessile droplet, on the other hand, is partially engulfed in the carrier fluid and has a lens-shape configuration. In order to trigger the movement of droplets, a thermal gradient on the surface is created by passing current through embedded heaters. This leads to a surface tension gradient, and deformation at the liquid/air interface thus creating motion of droplets towards the heating source (Yakhshi-Tafti et al. 2010a). Although at first this might seem counter-intuitive, the surface slope due to gravity counteracts the Marangoni force inside the liquid film, consequently the droplets migrate towards the heater. In the case of submerged sessile drops, they behave like tracers and their movement is in the direction of Marangoni flow, away to the heating source.

Understanding the physics of droplet collision on liquid films is beneficial, as many biochemical reactions take place in such environments rather than solid substrates. In addition, the droplet transport is faster and it would be possible to handle the biochemical reagents in a simple but practical manner. There has been no study of natural or passive coalescence of droplets on a thin film.

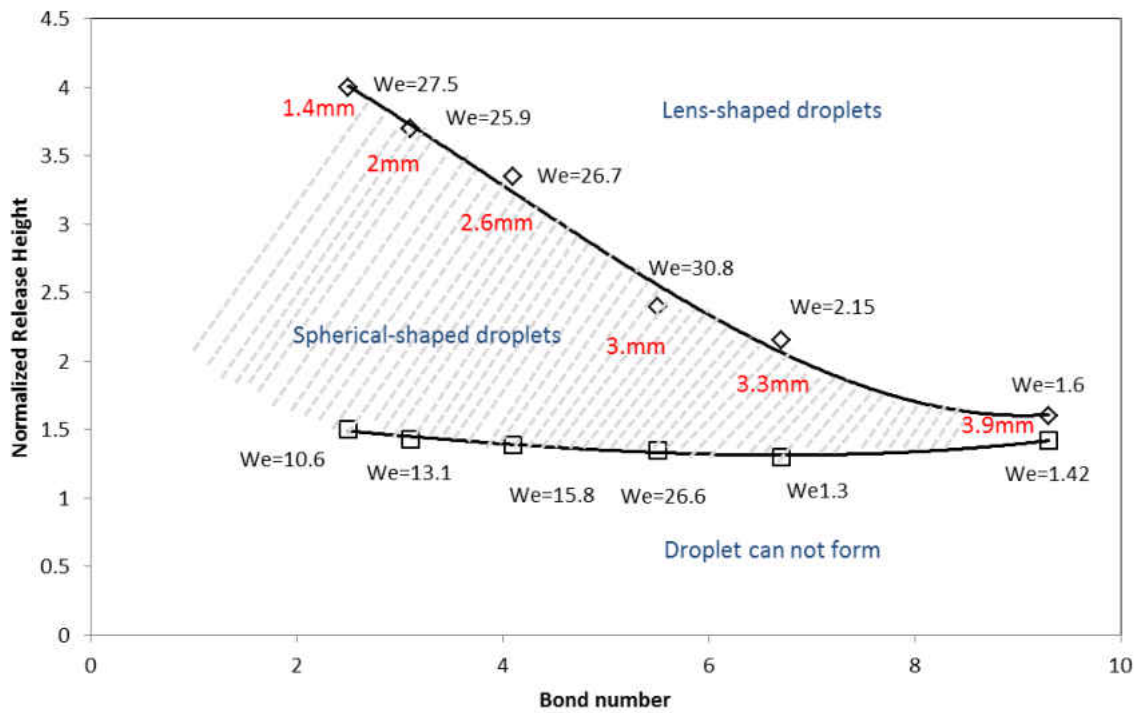


Figure 4.1: Normalized release height as a function of Bond number ($Bo = \frac{\rho g H^2}{\sigma}$, where H is the releasing height). Droplet diameters are indicated in red. Weber number is calculated as $We = \rho U^2 D_{drop} / \sigma$, where U is the impact speed which is a function of release height given as $U = \sqrt{2gH}$.

We address the collision of droplets levitated on Marangoni flow of a second immiscible liquid. Non-dimensional numbers such as Weber number and impact number are used to explain the phenomenon. Later, we used a combination of different fluids to study the effect of viscosity

on coalescence. The results in this work reveal that by creating a thermal map, it is possible to transport droplets to desired locations precisely, and also to drive droplets naturally to coalescence and mix them. The current work provides an opportunity for better understanding of thermo-coalescence phenomenon and an optimal design of droplet-based systems.

4.2: Methods

A double-sided 96 x 64 mm² board is used as the main platform. The laminate is 1.57 mm FR-4 epoxy glass with 36 g of copper. Pads are plated with a tin/lead solder. The solder mask layers are green LPI and the etching resolution is 0.15 mm. A custom made acrylic sheet is used to create a sealed container for liquid film on top of the printed circuit board (PCB). The sheet is mounted on the board using screws and adhesive sealant. The wires are back soldered to the board. As the board does not have the typical green solder mask, the yellowish color of FR-4 laminate is dominant.

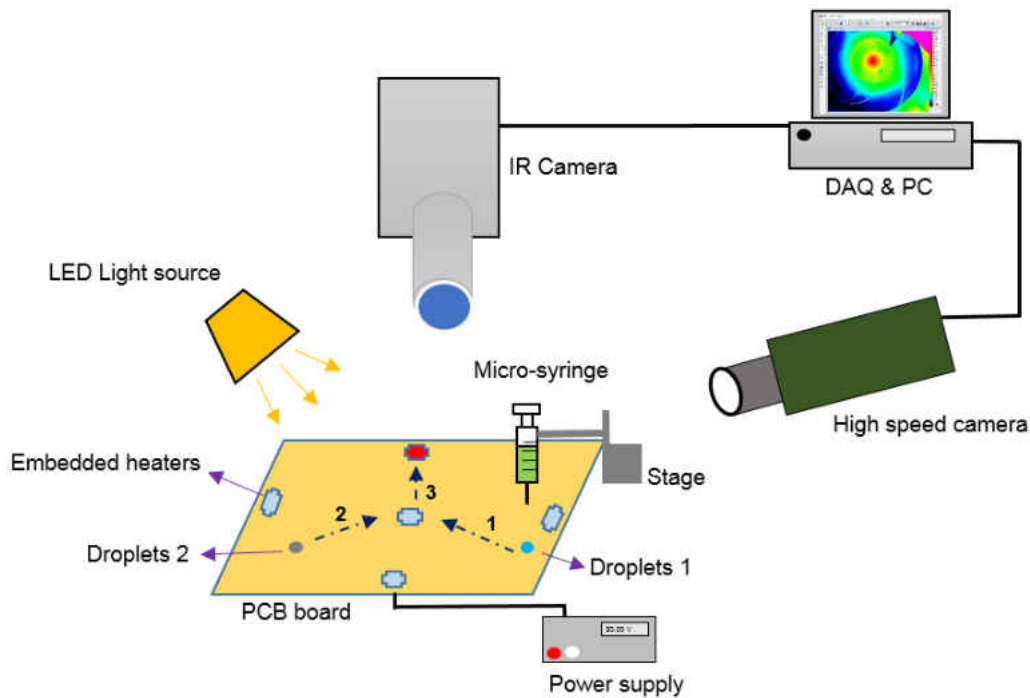


Figure 4.2: The experimental setup to study the collision of droplets on thin liquid films due to Marangoni effect. The micro-heaters are made out of copper. Light source and cameras are aligned with the droplet migration. An infrared camera is used to monitor the temperature variation of droplets and the carrier liquid. Droplets are produced from a precision needle that is kept at a constant height from the film.

Fluorinert FC-43 (SynQuest Laboratories, Cat. No. 3132-2-43) is used as carrier liquid for droplet transport. FC-43, is a chemically inert and thermally stable liquid. The thickness of the liquid film is 2 mm at room temperature. Droplets are made of Potassium Hydroxide (LabChem, Cat. No. LC19275-1) and Phenolphthalein (Ricca Chemical Co., Cat. No. 5600-16). The properties are summarized in Table 4.1. The platform is cleaned with acetone and methanol between experiments.

Table 4.1: Physical properties of tested liquids. Some of the properties are taken from Wehking et al. (2013).

Liquid	ρ [g/c m ³]	ν [centiStoke]	σ [mN/m]	γ [mN/m]
Fluorinert (FC-43)	1.88	2.8	16	-
Water	1	1	71	52
Potassium hydroxide	1	1.05	72.1	-
Phenolphthalein	1.3	2.05	29.5	-
Ethanol	0.79	1.52	22	17.8
Silicon oil 20 cSt	0.95	20	20.6	5.42
Silicon oil 50 cSt	0.96	50	20.8	5.68
Silicon oil 100 cSt	0.96	100	20.9	5.51

Figure 4.2 shows the experimental setup. The setup includes a PCB board with embedded heaters, a micropositioning system, electric power supply, imaging acquisition equipment and a droplet generator. Droplets are generated by gently pressing the plunger of a micro-syringe (Terumo). The inner-diameter of the needles are $\sim 0.210 - 0.108$ mm generating droplets with diameter $\sim 2.5 - 3.6$ mm. The syringe is positioned in a stage and kept at a constant height ~ 1.5 times the droplet diameter over the film. The droplets of size 3mm are released from the needle tip due to a gravity driven pinch-off. A DC power supply (HC3002, TE) is used to pass electric current through the embedded titanium strips and generate heat due to its electric resistance. The applied voltage is between 20 - 40 V. Imaging hardware used in the setup includes a high-speed camera (i-Speed 2, Olympus), 2000 frames per second (fps) and resolution of 576 x 432, a magnification zoom lens (Zoom 7000, Navitar), a digital SLR

camera (DS126071, Canon) and a LED light source (LG). The impact parameter and impact velocity are obtained through analysis of the high-speed video images using MATLAB. In order to track the temperature profile of the film and droplet, an infrared thermal imaging system is used. The IR-camera (SC5000, FLIR) can take images over 380 fps at full resolution of 640 x 512 pixels. The temperature range used in the current experiment is 22-67°C and with an integration time of 1.17ms. The video images are analyzed using Altair software developed by FLIR systems.

4.3: Results

First we study the motion of a levitated droplet on a liquid surface due to thermocapillary effect. Due to the applied temperature gradient inside the liquid film Marangoni flows will form that circulate the carrier liquid. This phenomenon is accompanied with liquid surface deformation. As a result the droplet migrates towards the hot side of platform. Figure 1a shows the droplet trajectory as a result of an applied 20 °C temperature difference between both sides of the platform. In order to create a sharp surface gradient, an electric pulse is given to the embedded resistor. In Fig. 4.3b the temperature profile of the carrier liquid along the symmetry line of the platform is plotted. The data are acquired from the infrared camera.

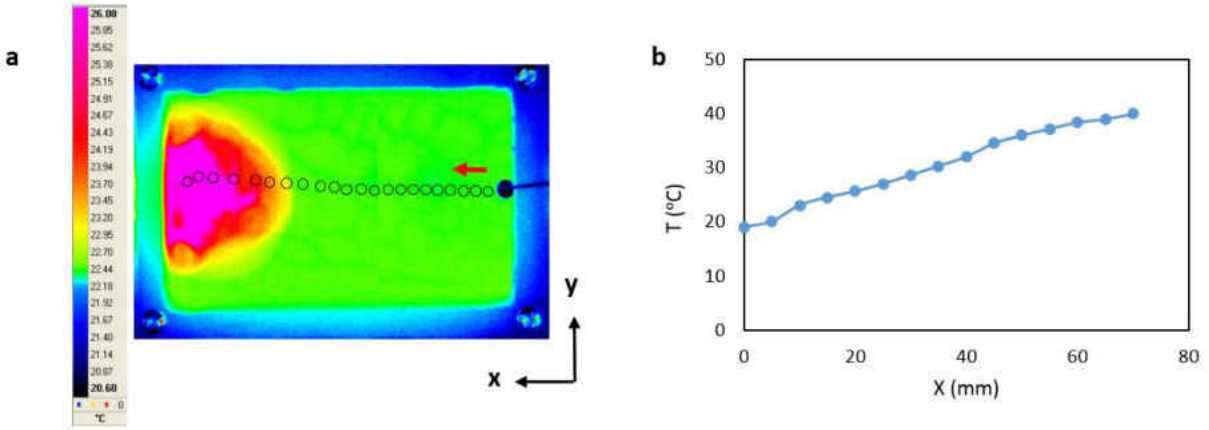


Figure 4.3: (a) The trajectory of a 3mm droplet for a temperature drop, ΔT , of 20°C across the channel is shown on an infrared image. The black circles represent the position of the droplet at every 14 frames; (b) Liquid film's temperature profile along the y-axis symmetry line of the channel from IR measurements. The heater is turned on right after the droplet is released.

Figure 4.4 shows the effect of an imposed thermal gradient along the channel on droplet velocity. Droplet velocity is measured by analyzing the trajectory of droplet motion while it migrates towards the heater using IR camera images, and it is calculated by measuring the distance a droplet migrated after 12 consecutive frames. The temperature difference is measured for the new droplet position at the beginning of each 12 frame interval with respect to the drop dispensing point. The velocity values are cross-validated using high speed imaging for the same motion. The calculated uncertainty of the measurement was ~4% for velocity and ~2% for ΔT . The procedure is repeated for $\Delta T = 40$ °C. Average velocities of the levitated droplets and sessile droplets which move in opposite directions are plotted against the velocity scale, given by

$$\tilde{V} = \frac{|\sigma_T| |\nabla T| R}{\mu} \quad (4.1)$$

where μ is the dynamic viscosity, R is the droplet radius, σT is the rate of change of interfacial tension with temperature, and ∇T , the temperature gradient imposed on the thin film (Hadland et al. 1999). Typically, spherical-shape droplets gain higher drift velocities in magnitude, although they migrate against the induced Marangoni flow. The lens-shaped droplets act similar to tracer particles. The size effect is favorable for spherical-shaped drops as they can reach higher drift velocities for the same temperature difference (ΔT), with the sessile droplets displaying the opposite effect due to larger drag for larger droplets (not shown here). Although all cases follow these trends reasonably well, the sessile drop velocities are significantly lower compared to the velocity scale, while the levitated droplet have similar values.

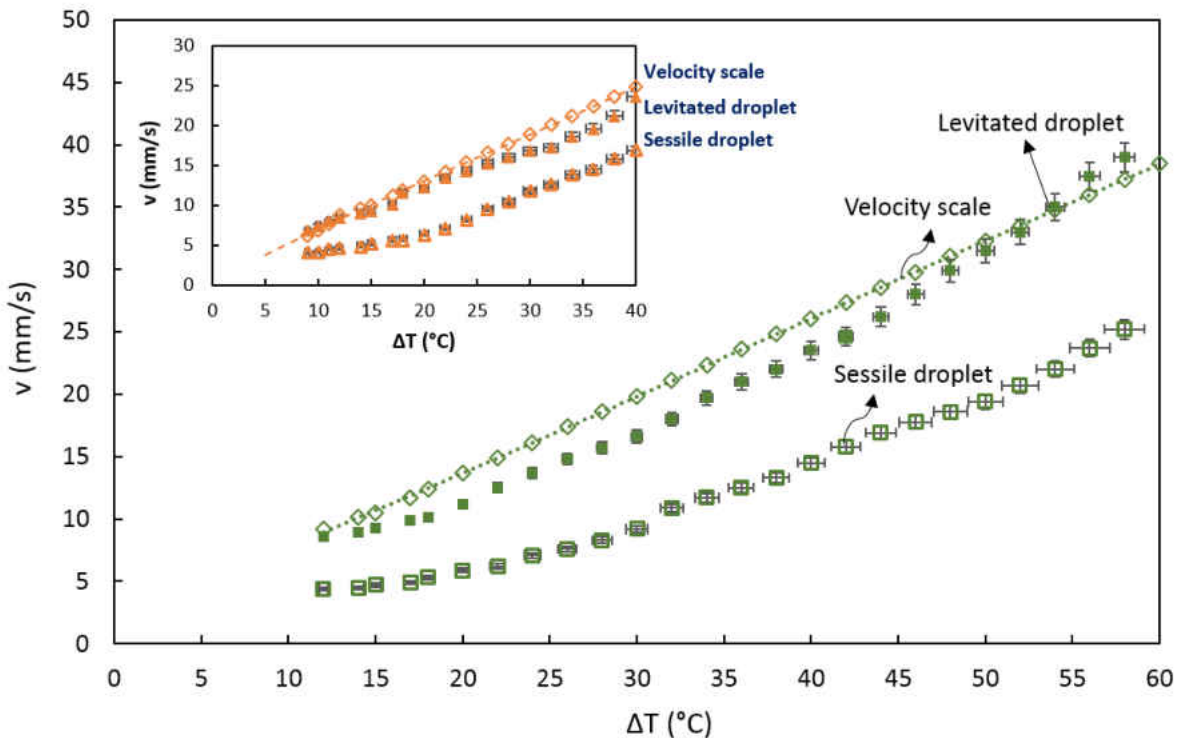


Figure 4.4: Variation of droplet velocity with temperature difference ($\Delta T=60$ °C). Velocity scale (theoretical), sessile drop velocity and spherical drop velocity (experimental) for a 3 mm water drop are shown. The velocity scale data are curve-fitted to show the trend. The inset shows experimental results compared to velocity scale for $\Delta T=40$ °C.

The droplets are released from a constant height (~ 1.5 times their diameter) on a thin film of Fluorinert oil so that the droplets can levitate. The collision of droplets is realized through thermocapillary effect, i.e. surface tension gradient which is caused by thermal gradient at the interface. Fig. 4.5 shows the transport of two equal-sized droplets to the center of the platform at different times along different paths. When the central heater is turned on, surface deformation occurs that allows the levitated droplet to move against the Marangoni flow underneath, floating towards the heater where the deformation is maximum (Frames 1-3). Once the droplet reaches the heater, the heater functions as a thermal trap, and the droplet remains stagnant at the center part of the platform (Frame 7). When the second droplet is released (Frames 4-6), this droplet also moves to the central heater where the surface depression is maximum, head-on collision ($b \approx 0$) occurs at the central heater in Frame 7, since it has higher power compared to the other embedded heaters. In order to illustrate the mixing phenomenon, the first droplet dispensed is potassium hydroxide and the second one phenolphthalein which is used as a pH-indicator. Both droplets are initially colorless, but when phenolphthalein is in contact with basic solutions ($\text{pH} > 8.2$), it turns pink. After 5.01 s, the two droplets coalesce, mix and form a larger levitated droplet that has a pink color. This large drop is at first thermally trapped at the heater. However, when the droplet temperature reaches the liquid film temperature, the spherical droplet ruptures the air layer underneath, submerges in the carrier liquid, and transforms to a more stable lens-shape sessile configuration.

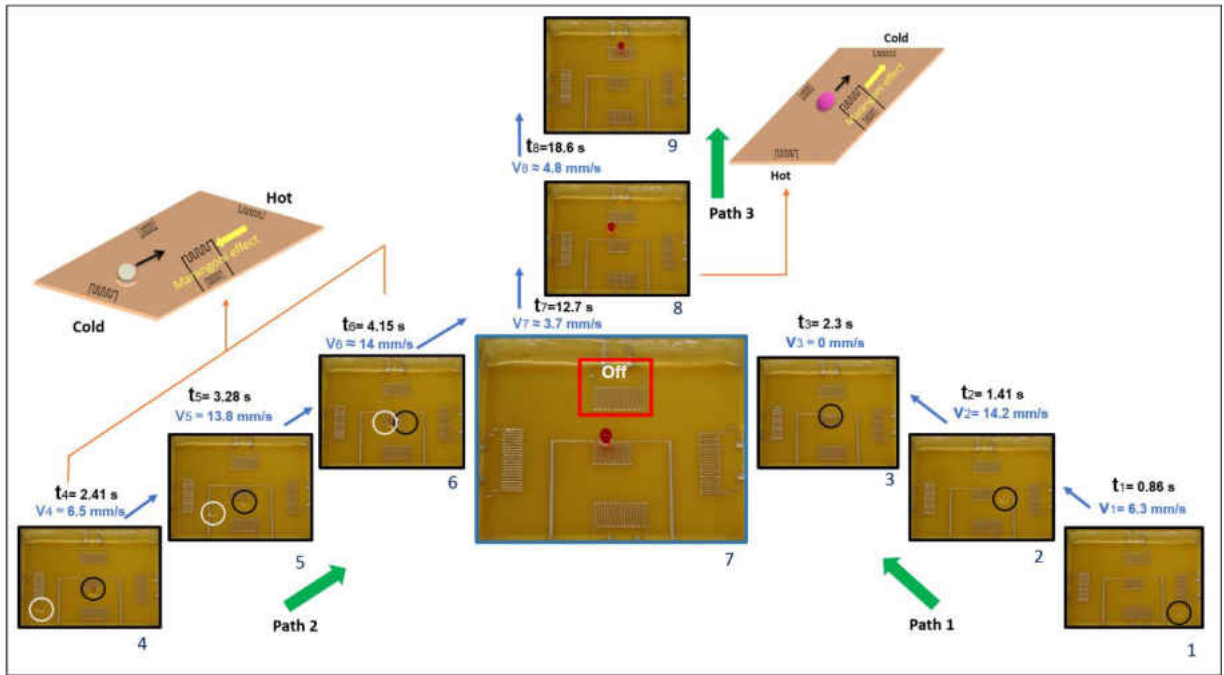


Figure 4.5: Transport and coalescence of levitated droplets. Initially, all heaters except the one shown as ‘off’ are active. The first droplet of potassium hydroxide is levitated at one end of the printed circuit board, and is allowed to flow through Path 1. After it migrates to the more powerful central heater, a second levitated droplet, phenolphthalein, is allowed to flow through Path 2 under the same condition. The drops collide and mix into a larger pink droplet. With continuous heating, the air layer underneath the droplet is ruptured, and the droplet sinks and becomes a sessile drop without being pinned. The sessile drop then moves towards lower temperature through Path 3. This dual migration of droplet moving towards or away from the heat source is governed by the thermocapillary effect due to the drop shape effect. The inset on the left shows the schematic for the migratory behavior of the levitated droplet against Marangoni convection. The inset on the right shows the schematic for the larger coalesced sessile droplet moving away from the heat source in the direction of the maximum temperature gradient.

Since all heaters are active from the beginning of the experiment except the one on top (as indicated by ‘off’ in Frame 7), a local cold spot is created in that region, and as pointed out earlier, a lens-shape drop follows Path 3 and migrates to the colder region that has higher surface tension forces. The sessile drop moves preferentially to the top instead to one of the other heaters (at low intensity) because of the maximum temperature gradient in this direction. Now, the question is whether the collisions occurring on a thin film will have similar outcome as collisions

under free flying condition. In the next section, we will investigate droplet migration due to Marangoni effect and the possible scenarios when impact parameter and Weber number

Weber number (We) is the ratio of the inertial force to the surface tension force, and the impact parameter (b) represents the relative distance between the centers of the two droplets. These non-dimensional parameters are typically used to explain the collision process of the droplets. For equal-size droplets, We and b are defined as $We=2\rho Rv^2/\gamma$ and $B/2R$, respectively, where ρ is the droplet density, γ is the interfacial tension between the droplet and thin film, v is the relative velocity and B is the projected distance between the droplet centers in the direction normal to vector v . We will now investigate the post collision regimes of a water droplet as impact parameter and droplet velocity vary. Velocities are low in Marangoni flow, and the range of Weber numbers reported here is two orders of magnitude smaller than for unconfined forced droplet collisions in air. Figure 4.6 shows the reported interaction of water droplets in air classified into three regimes, while the inset depicts the observed regimes in the current study.

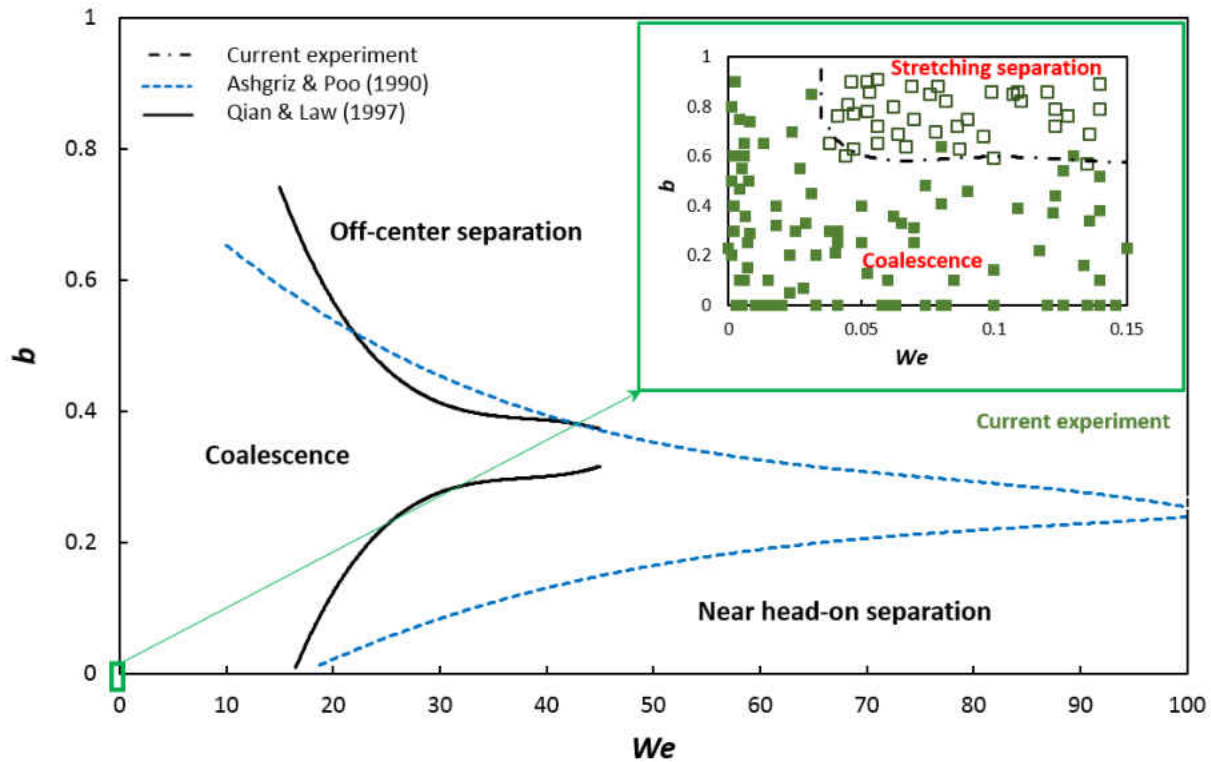


Figure 4.6: Analytically obtained regions of coalescence, reflexive separation, and stretching separation for equal-sized water droplets based on Ashgriz and Poo (1990) and Qian and Law (1997). The inset shows that collision of drops on a thin film leads to two distinct regimes at very low Weber numbers ($2.5 \text{ mm} \leq D \leq 3.6 \text{ mm}$). Each square shows one experiment.

At low impact velocities, i.e., low We , the collision of droplets results in an immediate coalescence even if occurs at high impact parameters. At higher impact velocities, beyond $We \sim 0.04$, the impact parameter determines the outcome of the collision. For $b > 0.6$, stretching separation rather than coalescence could be the dominant regime. The results include the collisions of a stationary droplet with an incoming droplet as well as two moving droplets.

At low impact velocities in the coalescence regime, the two droplets form a single drop and subsequently mix as seen in Figure 4.5 using the pH indicator. The coalescence phenomenon advances in three successive stages: 1) approach and collision of drops from an initially large

separation, 2) film drainage that occurs when the separation distance is asymptotically small compared to the drop radii, 3) film rupture as a result of instabilities. The coalescence can only occur if the air film thickness reaches the critical value of 10^2 A° or less (Wu et al. 2004). In this case, they form a larger droplet with a mass equal to sum of the mass of primary droplets. Yi et al. (2014) reported that the rise in droplet temperature increases the probability of coalescence after the collision of droplets. Figure 4.5 shows the coalescence of 3 mm levitated droplets at a camera speed of 2000 fps, where different collision stages are noticeable. As the drops collide, they attain a dumbbell shape initially. When the ambient fluid between them is pushed away, they first become tubular and later into a stable larger spherical droplet.

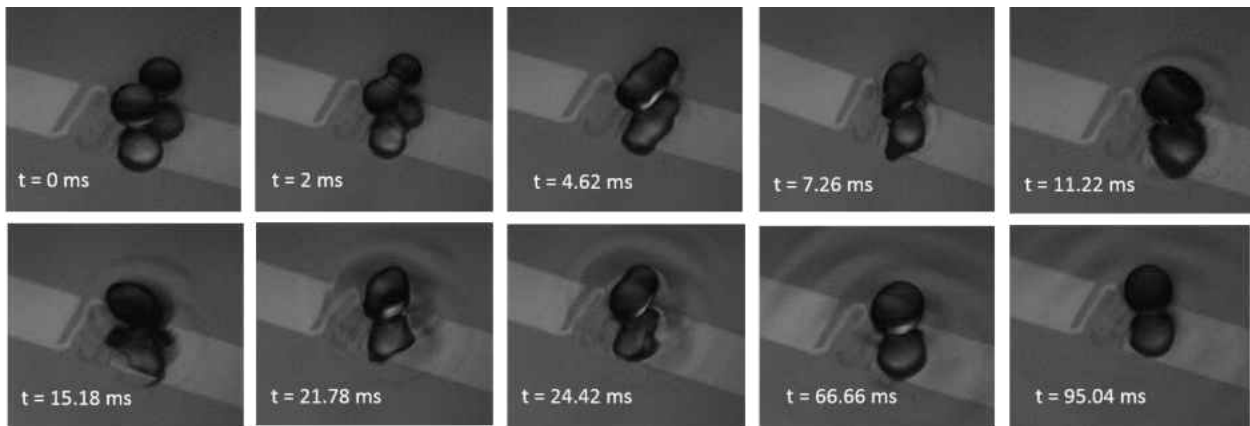


Figure 4.7: A sequence of high-speed images show the stages of head-on collision that lead to permanent coalescence ($\Delta T=20^\circ\text{C}$, $D=3 \text{ mm}$, $We=0.012$). Both the droplets and their reflection are seen until they coalesce.

Reflexive separation is known to occur for near head-on collisions, while stretching separation (also called off-center separation) occurs at moderate to large impact parameters (Ashgriz and Poo 1990). In stretching separation, after droplets collide temporarily to a combined mass form and eventually separate into two or more drops. This is attributed to the

competition between the kinetic energy of the untouched part of the drop and the surface energy of the interacting part (Ashgriz and Poo 1990; Munnannur and Reitz 2007). Stretching separation may follow by fragmentation in which satellite drops form.

The two major modes that are observed in collision of levitated drops are shown in Figures 4.8a and 4.8b. In these snapshots one droplet is colored with blue dye to better show the interactions. Coalescence is facilitated by surface tension forces at low impact velocities (Fig. 4.8a). At low impact parameters, the relatively high kinetic energy (higher ΔT 's) helps the impacting droplet to break the air film faster compared to lower ΔT 's. For stretching separation, there is no obvious formation of liquid bridge between the droplets (Yi et al. 2014). After collision, a minor deformation occurs and each droplet is seen to its own path while it is still levitated (Fig. 4.8b).

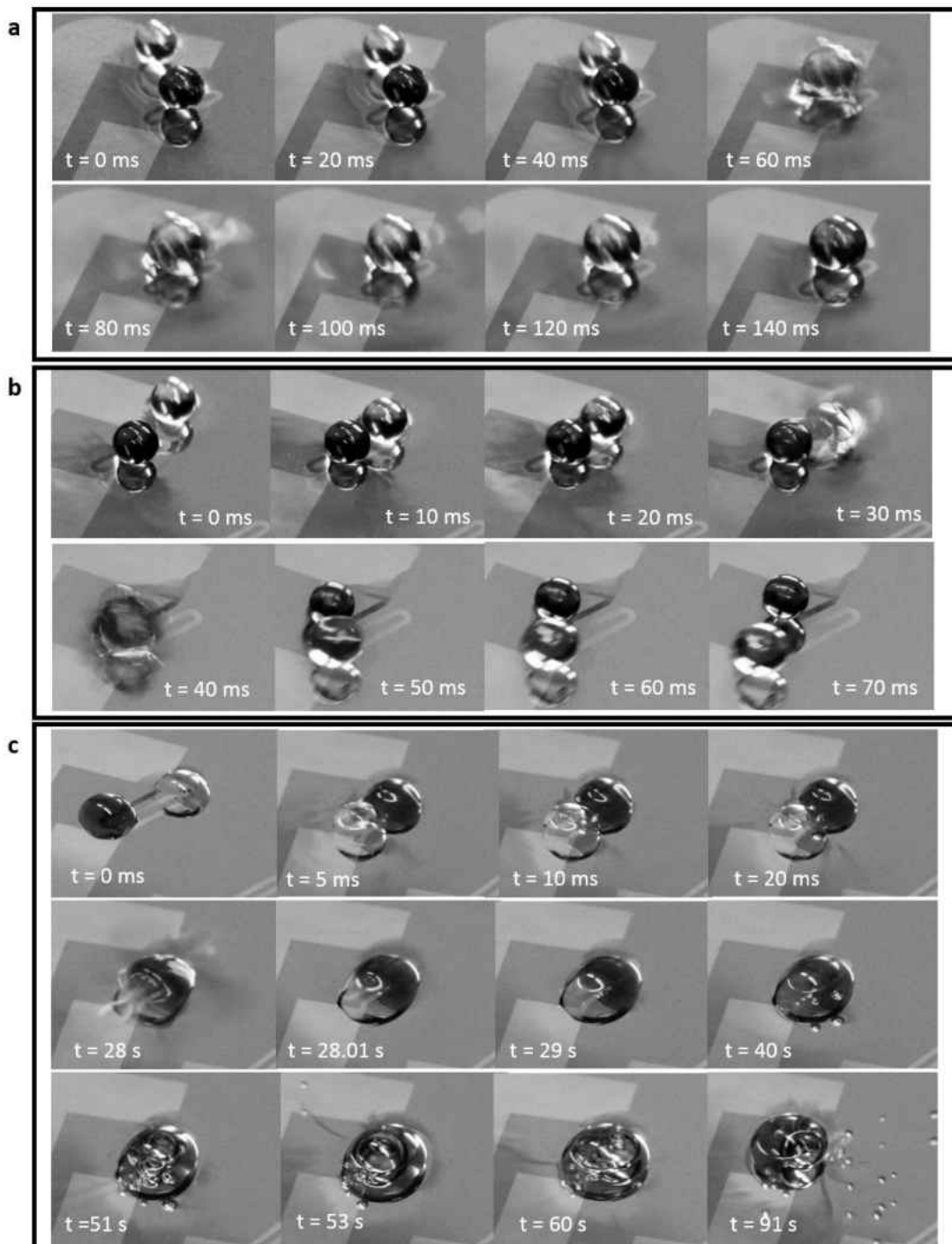


Figure 4.8: Snapshots of the collision of identical droplets for $\Delta T = 20$ °C. (a) coalescence of spherical-shaped water droplets ($D= 3$ mm, $v= 10.2$ mm/s, $We= 0.012$); (b) stretching separation of spherical-shaped water droplets ($D= 3$ mm, $v= 10.2$ mm/s, $We = 0.012$); (c) coalescence of sessile water droplets on a liquid substrate ($D= 2.5$ mm, $v= 14$ mm/s, $We= 0.0067$).

The coalescence of the sessile droplet is independent of their impact parameter. Such droplets that are partially submerged may convert to pinned droplets if either the thickness of liquid film below them shrinks significantly due to a large imposed thermal gradient or the size of the formed droplet is so large that it touches the solid substrate. In Figure 4.8c, the coalesced droplet gets pinned, evaporates after a few seconds and undergoes a phase transition. The rise of the droplet temperature will increase the vapor pressure. The accumulation of vapor around the droplet helps push out air at the interface upon impact, therefore the possibility of coalescence after collision increases (Qian and Law 1990; Li et al. 2014). In this study, we used liquids such as silicon oil and water at atmospheric pressure, which have relatively low vapor pressure. It is also important to mention that the process of coalescence of levitated droplets typically occurs in milliseconds (Figure 4.8a). The low thermal conductivity of the carrier liquid ($0.066 \text{ W/m}^\circ\text{C}$) helps avoid an excess temperature rise in floating drops. Therefore, the vapor pressure effect was seen to be minimal for the pair of fluids used in our study. Compared to the coalescence of levitated drops, the coalescence time for sessile droplets is three orders of magnitude greater. This is comparable to reported values in the literature (Arkhipov et al. 1978; Wang et al. 2008) for sessile drops on super hydrophobic surfaces. However, due to lower impacting velocities, in the current experiments, other types of interaction such as the rebound or disruption of the coalesced droplets were not observed.

4.4: Discussion

Viscosity has a major effect on the transport velocity of the levitated droplets and hence coalescence. Here, the thermocapillary effect causes surface deformation of the liquid film, however a lower viscosity fluid can reach higher velocities. For the same ΔT , when the viscosity

is larger, the collision kinetic energy (CKE) is lower due to low velocities. In general, when the droplets coalesce, the coalesced droplet has a smaller surface area than the sum of two pre-collision droplets (Ashgriz and Poo 1990), thus there is a decrease in surface energy from pre- to post-collision. In this case, the surface energy stays the same since the original droplet size is the same. However, CKE reduces due to higher viscosity, promoting coalescence (Figure 4.9). In addition, earlier coalescence occurs since both CKE and final surface energy (which is the difference between pre- to post-collision surface energy) are dissipated through work done during the breakage of the air film (Orme 1997). In Figure 4.9, the coalescence process is facilitated easier at higher viscosities, thus shifting the transition line upwards, indicating that the impact parameter i.e., the separation distance, can be higher for higher viscosity fluids to merely graze and coalesce.

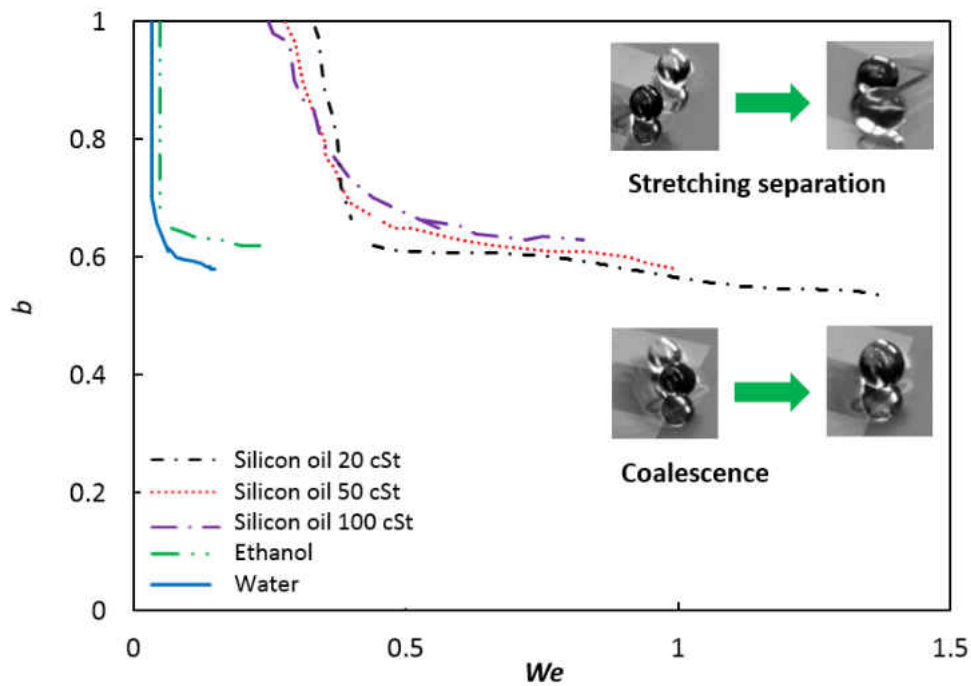


Figure 4.9: Impact number vs. Weber number for silicon oil drops ($D=3\text{ mm}$) of various viscosities. Increase in viscosity leads to higher chance of coalescence even at slightly larger impact numbers.

In summary, our recent discovery (Yakhshi-Tafti 2010a) that levitated droplets float in the opposite direction of surface velocity of a liquid layer undergoing Marangoni convection is exploited to naturally coalesce droplets on liquid substrates. The collision behavior of identical drops is studied experimentally as a result of a thermal gradient on a thin film. The existence of the transition line between coalescence and stretching separation in this passive mode of transport is similar to what was observed in the literature for force coalescence at significantly higher Weber numbers (Ashgriz and Poo 1990; Orme 1997; Jiang et al. 1992; Qian and Law 1999). This study offers new insight to thermo-coalescence and demonstrates how natural coalescence could be used to transport, mix and collect reagents in an efficient manner. The results can be employed to enhance performance of self-cleaning surfaces, thermal diodes and micro-total analysis systems. As future work, the role of Marangoni effect on droplet mixing will be studied.

CHAPTER 5: PASSIVE MIXING ENHANCEMENT OF MICROLITER DROPLETS IN A THERMOCAPILLARY ENVIRONMENT

5.1: Introduction

Droplet-based microfluidics with its capability to manipulate discrete units of fluid has many lab-on-a-chip applications. In such systems, sample transport, filtration, collision and mixing are some of the main operations that should be addressed (Samie et al. 2013). Specifically, the coalescence and mixing of droplets are of great importance in microchemistry, biological applications, and inkjet printing (Castrejon-Pita et al. 2013; Beebe et al. 2002). Mixing and internal dynamics of coalescing droplets on solid surfaces with focus on wettability gradient of the substrate have been published in the literature (Yeh et al. 2013 and 2014; Castrejon-Pita et al. 2013). In microfluidics, owing to laminar flow conditions the mixing of liquids is difficult to realize (Yakshi-Tafti et al. 2008; Paik et al. 2003). The two dominant fluid mixing mechanisms in micro scale are (a) molecular diffusion and (b) chaotic advection (Yeh et al. 2013; Grigoriev et al. 2006). Generally, molecular diffusion is a slow process which is governed by viscous forces (Strook et al. 2002). On the other hand, chaotic mixing is faster but it requires stirring process that stretches and folds the fluid in the entire domain, which is practically hard to achieve on open-surface platforms (Aref 1984). Wiggins and Ottino (2004) reviewed the mathematical foundation of chaotic mixing in detail. Serpentine channel design is one of the solutions to enhance the mixing phenomenon (Yakshi-Tafti et al. 2008 and 2011, Song et al. 2003; Stone and Stone 2005; Liu et al. 2000), however such designs have their own challenges in terms of complexity and multiplexity.

So far, fast mixing of droplets have been achieved in different ways. Hosokawa et al. (1999) used the interfacial force during droplet impact to generate internal motions inside droplets. Wu and Nguyen (2005) employed two-phase hydraulic focusing to achieve rapid mixing in microchannels. Electrokinetic mixing in microfluidic devices was applied by Chang and Yang (2007). In their work, electrowetting-on-dielectric (EWOD), dielectrophoresis (DEP), and electroosmosis (EO) were extensively discussed and compared. Nevertheless, using these methods, mixing can still take up to few seconds. Our earlier papers (Davanlou and Kumar 2015a and 2015b) have discussed the motion and drag coefficient of levitated droplets which travel against the thermocapillary flow underneath. In addition, we showed the possibility of natural coalescence of droplets at desired locations by precisely routing them through the Marangoni effect (Davanlou and Kumar 2015a). Because of the applied thermal gradient on liquid layer which is located under droplets, the surface temperature of the floating droplets increases as they are transported towards the heater. This temperature rise causes an additional internal circulation inside droplet attributed to Marangoni flows. Note that initially upon coalescence of droplets, due to the released surface energy a pair of recirculation cells occurs inside the merged droplets which improves the fluid mixing (Yeh et al. 2013).

In this brief communication, we investigate the role of thermocapillary flow underneath two equal-sized colliding droplets that have different compositions. By creating a temperature difference of 0 - 30°C between the heater and the droplet loading location, droplets are actuated with different velocities. The mixing progress is quantitatively studied through analyzing the images from merging till the full mixed state is reached. An appropriate time scale for this

problem is developed and implemented to find a universal correlation for mixing time as a function of Reynolds number.

5.2: Experimental Setup

The platform of this experiment, shown in Fig. 5.1, is fabricated on a 96 x 64 printed circuit board (PCB). Copper is used to make the desired heater patterns on top of the board. A power supply (TE, model HC3002) provides the electric potential required for creating certain thermal gradients. A camera (Prosilica, model GE680C) with 388 frames per second (fps) and resolution of 320 x 240 pixels is used to capture the events while an infrared camera (FLIR, model SC5600) monitors the temperature of the platform. The infrared camera can reach up to 380 fps at full resolution of 640 x 512 pixels. A combination of precision needles with micro-syringe are used to generate droplets (2.5 – 3.6 mm in diameter). The droplets are made of potassium hydroxide (KOH, 0.01 M; LabChem) and phenolphthalein (C₂₀H₁₄O₄, 0.5% (w/v) in 50% (v/v) Alcohol, Ricca Chemical Co.). The potassium hydroxide droplet has a density of 1000 Kg/m³, viscosity of 1.05 cSt and surface tension of 72.1 mN/m and phenolphthalein droplet has a density of 1300 Kg/m³, viscosity of 2.75 cSt and surface tension of 29.1 mN/m. Collision of these two droplets causes a color change due to the chemical reaction that takes place inside the coalesced droplet. Spatio-temporal analysis of this color change through an in-house developed MATLAB code is used to study the progress of mixing phenomenon.

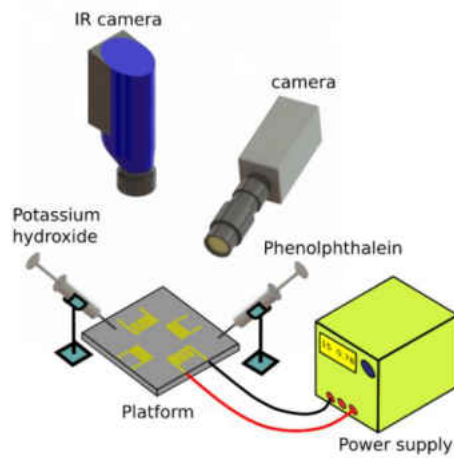


Figure 5.1: Schematic diagram of the experimental setup. Phenolphthalein (HIn) is a pH-indicator that turns pink in a base solution like potassium hydroxide.

5.3: Results and Discussion

We study the head-on collision and the subsequent mixing of levitated droplets due to an imposed thermal gradient on the liquid substrate. The experiment is devised such that a droplet of potassium hydroxide is dispensed first while enough time is given so that it migrates toward the heater due to liquid surface deformation. Then a second droplet of similar size but made of phenolphthalein is dispensed. The latter droplet moves to the same heater where the first droplet is already trapped, hence the droplets coalesce and a chemical reaction inside the larger droplet takes place, turning its color pink. The droplets are released from a height ~ 1.5 times their diameter, a minimum requirement to levitate the droplet with an air gap between the droplet and the liquid underneath (Davanlou and Kumar 2015a).

The mixing phenomenon has been quantitatively studied in the literature by employing optical diagnostic tools such as laser-induced fluorescence (LIF) (Carroll and Hidrovo 2013; Yeh et al. 2013), particle image velocimetry (PIV) (Ortiz- Dueñas et al. 2010), and spontaneous

Raman scattering (SRS). Here, with the aid of high-speed color imaging and image processing, the mixing phenomenon is investigated by monitoring the color changing reaction that occurs inside the coalesced droplet. Nilsson and Rothstein (2011), and Yakhshi-Tafti et al. (2011) have used a similar approach in order to measure the degree of mixing of two droplets. The process is divided into the following steps: a) the images undergo a color enhancement process, b) the image type is converted from RGB to gray scale, c) suitable filters are applied to cancel or reduce the noise, d) a new scale is used to determine the image contrast, varying from 0 to 1, e), the light reflection from the background surface is eliminated by applying appropriate thresholds. This assures that only the droplet and not the surrounding is analyzed. Fig. 5.2 visually shows these steps. The details of image processing algorithm is explained in Refs (Yakhshi-Tafti et al. 2011; Davanlou 2014).

In our algorithm, I is the measure of mixing, where $I=0$ is designated for the parts that are fully mixed and $I=1$ for the non-mixed portions. The deviation of gray intensity around the darkest gray pixel (completely mixed region) is calculated for the pixels of the selected cross section (Stroock et al. 2002):

$$\sigma = \left[\frac{1}{n} \sum_{i=1}^n (I_{min} - I_i)^2 \right]^{1/2} \quad (5.1)$$

where n is the number of the cross sectional pixels, I_i is gray intensity of pixel i of the selected cross section and I_{min} is the minimum gray intensity. If there is no mixing, the standard deviation is $\sigma = I$, while $\sigma = 0$ represents full mixing as all pixels attain uniform gray intensity. The level of mixing in percentage is calculated as:

$$M (\%) = (1 - \sigma) \times 100 \quad (5.2)$$

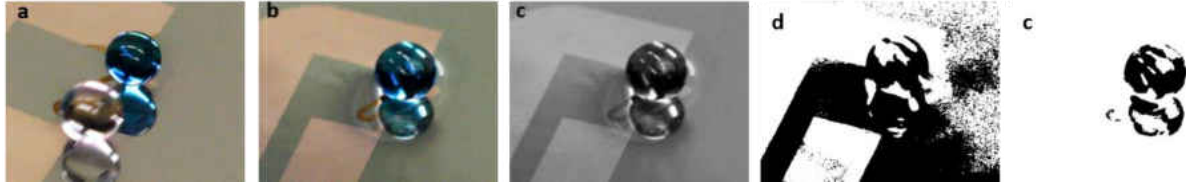


Figure 5.2: (a) Head-on collision of droplets. After coalescence due to chemical reaction the color change occurs. Image processing of the coalesced droplet can be divided into: (b) mixing is captured as a color image; (c) conversion of this color image into a grayscale image; (d) conversion of the grayscale image into a binary image; (e) background subtraction and quality improvement on the binary image.

The photographs shown in Figure 5.2 are captured schematically in Figure 5.3 to illustrate the coalescence and mixing mechanisms. When the droplets collide, the resulting coalesced droplet deforms in the vertical and horizontal directions as shown in Figure 5.3d and 5.3f, which leads to internal circulation of the fluid inside the droplet. Due to this circulation, the mixing percentage increases and is further enhanced when the droplet temperature rises as it is heated by the liquid surface (Figure 5.3g).

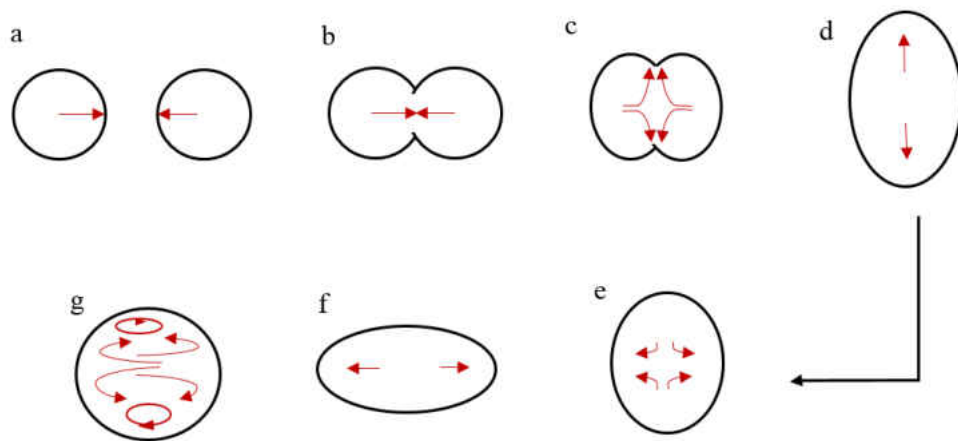


Figure 5.3: Schematic diagram of collision and mixing of two equal-sized droplet.

Figure 4a illustrates the change in mixing efficiency of droplets when they collide due to a temperature difference. The variation of the liquid film temperature measured by the IR camera is shown in Figure 4b. Initially, in order to obtain the mixing percentage without a thermal rise (i.e., $\Delta T = 0\text{ }^{\circ}\text{C}$), the droplet is placed on the substrate. Then, the second droplet is released on top of it so that coalescence and mixing occur. Also as the droplet size reduces, the mixing percentage increases. Since a two-dimensional image is analyzed, our technique of mixing analysis uses an arithmetic mean of all the pixels in its depth at a given pixel coordinate. To avoid introducing high uncertainty in measurements, for each case of an imposed temperature drop, 10 cases are separately analyzed and averaged. The average value of mixing percentage is plotted against the temperature drop for each experiment in Figure 5.4. The repeatability of measurements is above 93%. It is important to note that the chemical reaction between potassium hydroxide and phenolphthalein is different from normal mixing because of the released heat of reaction as well as the distinct product from the collision which has its own physicochemical properties (Yeh et al. 2014). Fig. 5.4c schematically shows the Marangoni convection inside a liquid film and the levitated droplet moving against this Marangoni flow. Using infrared thermography, the rise of droplet surface temperature is tracked as it migrates towards the hot region. Fig. 5.4d provides the droplet surface temperature for three dropsizes. As expected, the smaller drop is seen to have a higher temperature in the substrate temperature range of $5\text{ }^{\circ}\text{C} \leq \Delta T \leq 30\text{ }^{\circ}\text{C}$.

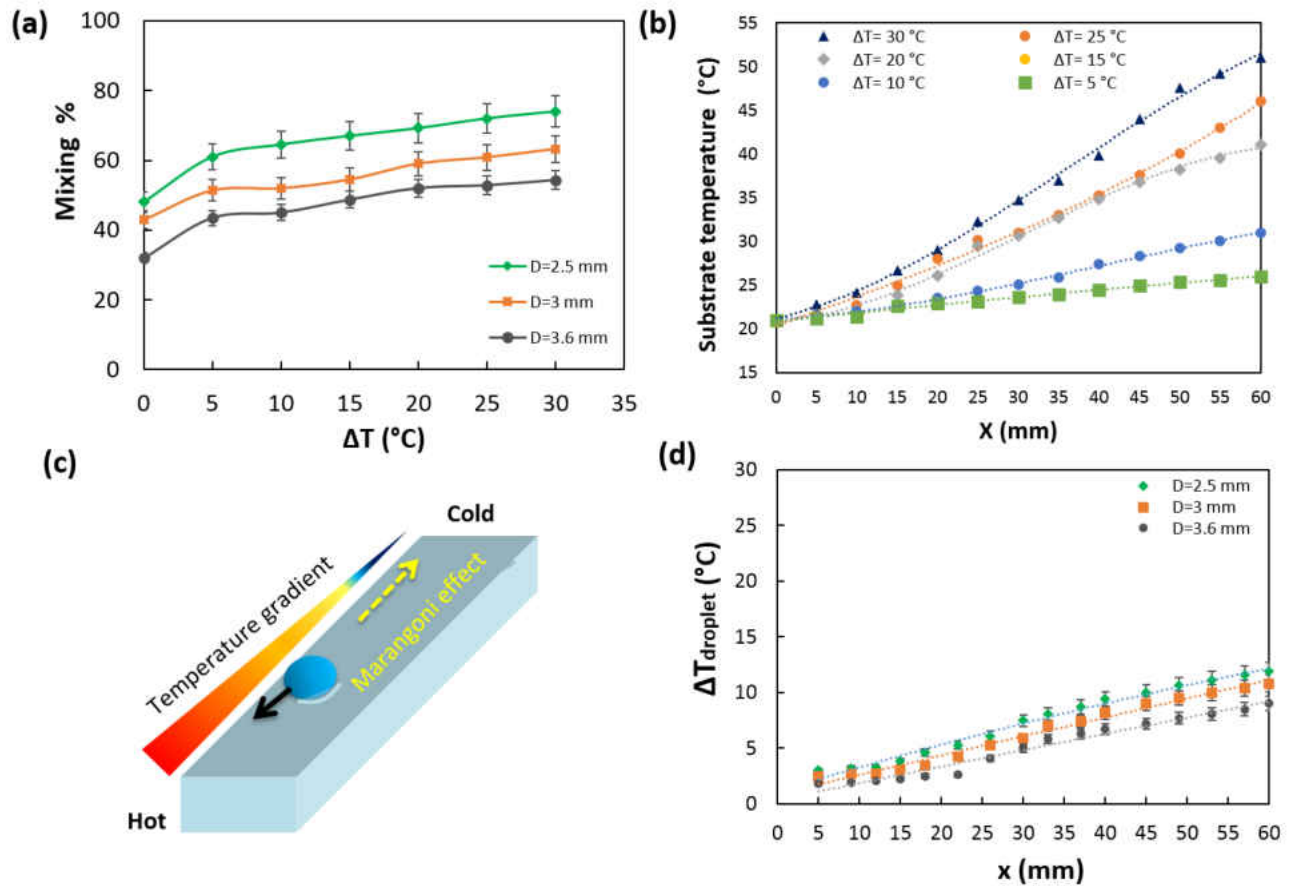


Figure 5.4: (a) The variation of mixing efficiency with temperature for three different diameters at 100 ms, (b) platform surface temperature increases almost linearly due to a $\Delta T=30$ °C, (c) The schematic depicts the counter-motion of the droplet towards the heat source against Marangoni flow in the liquid substrate. The initial temperature of the liquid substrate is measured using the IR-camera immediately prior to droplet release, (d) Variation of droplet surface temperature as it migrates towards the heater.

This problem has several relevant time scales. Schmidt number, $Sc = \nu/D = Pe/Re$, can be used to compare the viscous diffusion with molecular diffusion, i.e., the ratio of Péclet number to Reynolds number. The mass diffusivity of water is equal to $D \approx 10^{-10} \text{ m}^2 \cdot \text{s}^{-1}$ and the kinematic viscosity is $\nu \approx 10^{-6} \text{ m}^2 \cdot \text{s}^{-1}$ which results in $Sc \approx 10^4$. This shows that the time scale due to viscous diffusion is small. Thermal kinetic energy is the main source of random motion of solute

molecules in molecular diffusion. The relevant time scale for molecular diffusion and convection are:

$$\tau_{Diff} \sim \frac{L_{ch}^2}{D} \quad (5.3)$$

$$\tau_{Conv} \sim L_{ch} / \tilde{U} \quad (5.4)$$

where L_{ch} is the characteristic length scale and \tilde{U} is the velocity scale, which will be defined later. The Péclet number can be obtained by dividing the mass diffusion time scale by convective time scale:

$$\frac{\tau_{Diff}}{\tau_{Conv}} = \frac{L_{ch}^2/D}{L_{ch}/\tilde{U}} = \frac{\tilde{U} L_{ch}}{D} = Pe = Re \cdot Pr \quad (5.5)$$

Re and Pr represent Reynolds and Prandtl numbers respectively that defined as:

$$Re = \frac{\tilde{U} L_{ch}}{\nu}, \quad (5.6)$$

$$Pr = \frac{\nu}{\alpha} \quad (5.7)$$

where α is the thermal diffusivity. Table 5.1 summarizes the group of dimensionless numbers for this problem.

Table 5.1: The range of dimensionless numbers at different ΔT s. The data is sorted according to the droplet size and volume. The Reynolds number is based on droplet diameter.

Drop size (mm)	Volume (μL)	Re	Pr	Pe x 10^4	Sc x 10^4
2.5	8.18	25- 81.4	6.99	25 - 83	1
3	14.1	43.2- 108	6.99	43.2 - 108	1
3.6	24.4	56.1- 164.1	6.99	56.16 – 164.2	1

The change of mixing with respect to time is plotted in Fig. 5.5a for $\Delta T = 25$ °C. It is shown that the mixing advances with time however, after ~ 80 ms the curve reaches an asymptotic value

(for all cases). A similar trend is observed for different size droplets while smaller droplets undergo higher mixing rates. Fig 5.5b shows that the mixing time decreases with increase in Reynolds number, however, the time required to achieve the final mixing percentage remains almost the same (~ 120 ms) for all cases.

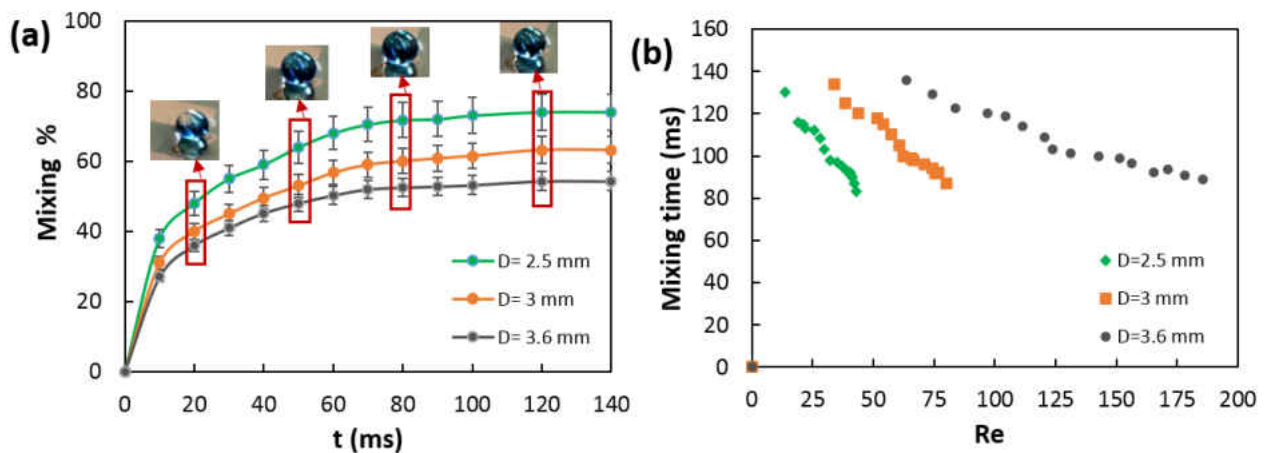


Figure 5.5: (a) Mixing progress with time for different drop sizes at $\Delta T= 25$ °C. (b) Dependence of Reynolds number with mixing time.

By using Eq. 6 and changing ΔT from 10 - 30 °C, Reynolds number and mixing time for head-on collision of droplets are determined. The results show that regardless of the size, with increase in droplet inertia, the time required for mixing reduces. Mixing is considered to be complete when the time after which the change in mixing percentage is less than 0.1%. The results indicate a significantly higher Reynolds number for larger droplets due to their larger relative velocity for the same ΔT , despite the fact that the mixing efficiency reduces with size. Note that the mixing time is in the order of milliseconds which is *8 order of magnitudes smaller than typical diffusion time scale*. This explains why the mixing mechanism is predominantly

governed by convection rather than diffusion. Therefore, it is reasonable to conclude that a higher thermal gradient helps in rapid mixing of droplets as it elevates the kinetic energy of molecules inside the droplet.

The non-dimensional mixing time versus Reynolds number is plotted in Fig. 6. The mixing time is normalized using a convection time scale $\tau \sim \frac{L}{\tilde{U}}$, where L is the average distance between drops and the hot spot where they collide and \tilde{U} is the velocity scale casts as $\tilde{U} = \frac{|\sigma_T||\nabla T|r}{\mu}$ with ∇T be the temperature gradient, r the drop radius, and σ_T the rate of change of interfacial tension with temperature (Davanlou and Kumar 2015a). A logarithmic correlation of mixing time normalized by the convection time scale given as a function of Reynolds number fits the data very well with $R^2=0.98$ in the Reynolds number range of 20 to 160.

$$\frac{t}{\tau} = 0.04\ln(\text{Re}) - 0.11 \quad (5.8)$$

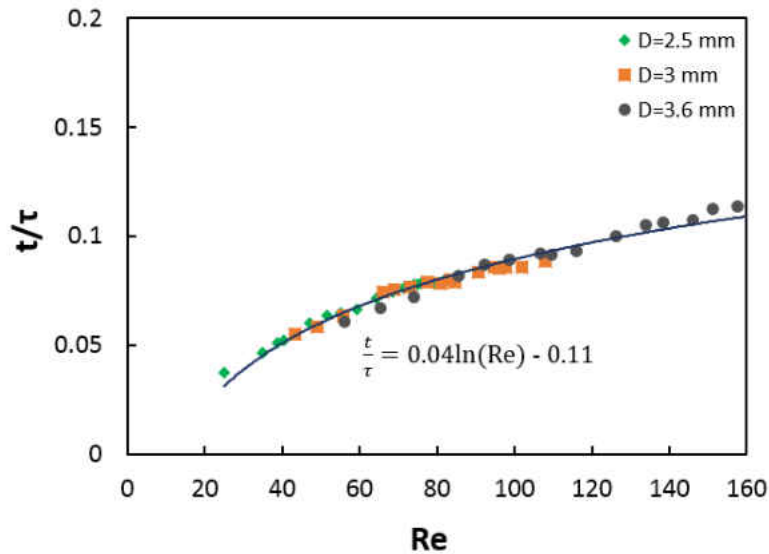


Figure 5.6: Normalized mixing time with convection time scale versus Reynolds number.

5.4: Summary

Recent work by the authors has shown that a droplet can be levitated on an immiscible liquid substrate, and upon application of a temperature drop on the substrate, the droplet travels toward the general direction of the heater and gets pinned at the heater. This work uses this concept to levitate two droplets of equal size at different chemical composition, and allows chemical reaction to take place upon collision. The mixing percentage at every instant is calculated by evaluation of color image processing. The temperature gradient on the substrate heats up the droplet and enhances the mixing. This mixing percentage increases with increasing temperature. Mixing rates as high as 74% is found to be reachable within 120 ms. For all cases, an increase in droplet inertia (Reynolds number) shortens the mixing time. However, the time required to achieve the saturated level of mixing is found to be nearly the same. The results also suggest that the reduction in droplet size favorably enhances the mixing percentage. Thus, utilizing a thermocapillary environment allows the use of droplets as microreactors in digital microfluidic applications to perform rapid and efficient mixing of reagents.

CHAPTER 6: APPLICATIONS

6.1: Applications

6.1.1: Introduction

In this final chapter, we propose that using thermocapillary application on an open-surface platform for droplet manipulation is suitable for biological and chemical technology. This silicon-based platform takes advantage of microfabricated titanium heaters and a controlling unit. The droplets are dispensed on a thin layer of an inert fluid (FC-43). A surface tension imbalance occurs inside of the liquid film, by generating a local heat flux at the interface. The surface tension gradient leads to a surface deformation. Therefore, the levitated droplets actuate and migrate towards the heated region of the surface which is undergoing depression. This simple principle is used to transport and mix droplets at the desired locations. Compared to the traditional approach, the suggested platform is capable of a continuous and quick delivery of droplets without sample evaporation or pinning. Even though the droplets were manipulated by heat, our study concluded that the temperature increase inside of the droplets is controllable. This discovery is significant in case of droplets carrying bio-samples, because they will not be affected. The performance of the platform is verified using a glucose calorimetric assay. The ability of this contact-free approach in precise and fast actuation of droplets could be extended to drug delivery, cell manipulation and analytical chemistry within a submillimeter size.

6.1.2: Design and fabrication

The platform design is made using a 3 inch silicon wafer with a 500 nm layer of the silicon dioxide as insulator on top of the wafer. A 1 μm layer of titanium is deposited as heater element. The fabrication process starts with wet oxidation on the silicon wafer. This step was done in 1000 $^{\circ}\text{C}$ for two hours. The procedure is followed with titanium deposition on top of the oxide layer using e-beam evaporation technique. The thickness of the titanium layer is 1 μm . This thickness is chosen in order to reduce the risk of electro-migration failure, which generally occurs from thinning of the titanium layer. The fabrication procedure is shown in Figure 6.1.

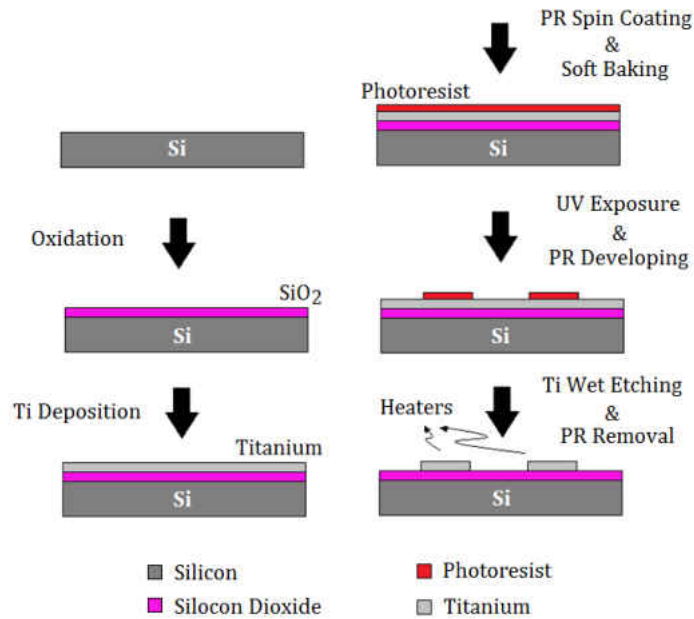


Figure 6.1: The fabrication procedure of the silicon wafer with embedded microheaters.

The next step is photoresist (PR) processing in order to pattern the titanium. The substrate is coated with hexamethyldisilazane (HMDS) at 4000 rpm for 60 s in order to enhance the quality and uniformity of photoresist. Shipley S1813 Positive resist is spin coated at 3000 rpm for 30 s. The PR was then soft baked at 105 $^{\circ}\text{C}$ for 180 seconds on a hot plate. The sample was exposed to

UV with a clear-field chrome mask on top using EVG 620 mask aligner. This process was done in gentle contact continuous mode in the G-line with the energy dose of 13 mW/cm^2 for 8.8 s. Then the PR is developed in concentrated resist developer MFTM-CD-26 for 70 s. Post development is then performed at $125 \text{ }^\circ\text{C}$ for 720 s.

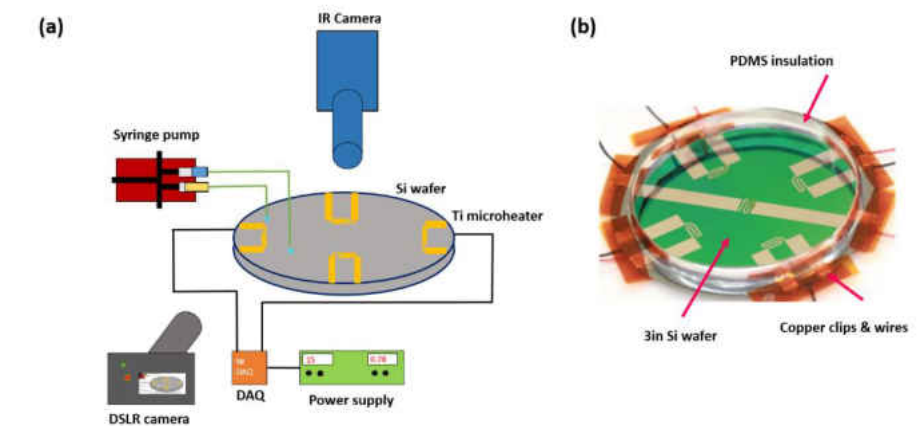


Figure 6.2: Schematic of the experimental setup.

Figure 6.2 shows the schematic of the experimental setup as well as the fabricated silicon-based platform. Heater patterns are covered with PR at this point since a positive photoresist has been used along with a clear field mask. The wet etching process was performed at room temperature for 100 s to achieve titanium pads with the heaters on chip. Titanium wet etchant is an acidic mixture consisting of one part hydrofluoric acid, and one part hydrogen peroxide, diluted in 20 parts of deionized water. Finally, the photoresist is stripped off using acetone. Methanol and distilled water are used to clean the wafer from any contamination. In final step, the silicon chip was air dried.

6.1.3: Transferring, trapping and mixing of biological assays

By considering the critical height, water droplets are released on a thin film of fluorinert oil. In order to generate thermal gradients, short electric pulses (< 2 s) are supplied to embedded heaters. Based on the Joule heating principle, the internal resistance of titanium strips converts electric energy into heat energy. The generated heat leads a deformation at the air/liquid interface causing water droplets to migrate towards the heat. By engineering the heaters, it is possible to transport droplets of various sizes or types from one end to another end of the platform. Figure 3 shows the sequence of this phenomenon with simultaneous color and infrared snapshots. The regions in green are at room temperature while red shows the location of heater. Figure 4a demonstrates the influence of input voltage variation on temperature difference between cold and hot spots after 10 s. As the applied voltage increases the difference in temperature between hot and cold spots increases.

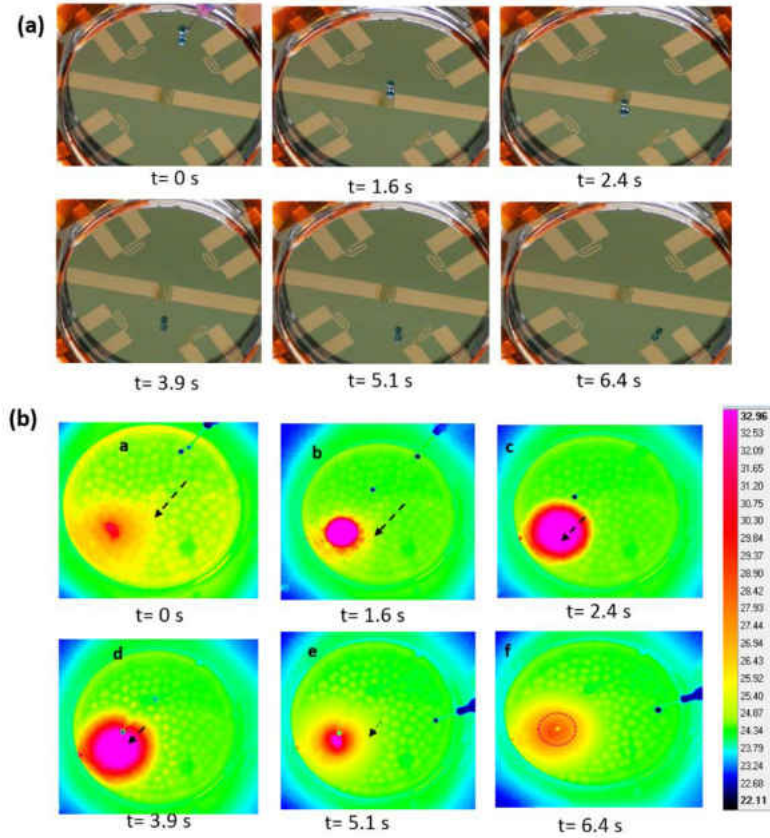


Figure 6.3: A 3mm water droplet migrates towards the heat source. (a) Snapshot of droplet transport, (b) Infrared images of the same phenomenon.

In order to evaluate the influence of thermal gradient on droplets we use Fourier number, which is the ratio of diffusive transport rate to storage rate, $= \alpha t / L^2$, where α is the thermal diffusivity, t is the characteristic time and L is the length through which conduction occurs. Typically for a spherical object L is $r/3$, where r is the radius. For a 3 mm water droplet, with a thermal diffusivity of 0.143×10^{-6} after 10 s the Fourier number is relatively small ($Fo = 2.54 \times 10^{-3} < 1$) also the ratio of thermal penetration depth ($\delta_p \propto \sqrt{\alpha t}$) to length is $\delta_p / L \ll 1$ ($\approx 7.56 \times 10^{-4} \ll 1$). These values indicate that the depth of droplet is not affected by heat. Therefore it is a valid assumption to state that the droplet core is not affected during its

transport to the hot region (Bejan 1993). Our calculations verify that the tested platform is reliable method for actuation and transfer of biological assays. In biological applications temperature can damage cells or other sensitive biofluids, as the inner temperature droplets containing such fluids will not be increased.

Applying a thermal gradient promotes a surface deformation, accordingly storing droplets and particles due to the effect of gravity is possible. Figure 6.4 schematically shows the trapping mechanism. The trapping is interesting because droplets containing reagents or samples need to be collected at a certain point on a chip. Turning off the heater allows the trapped particles to be released and move to a new location (Basu and Gianchandani 2008). However, trapping of the droplets for a long period of time is still a challenge due to the limited lifetime of levitated droplets as the temperature difference between the droplet and the liquid surface underneath tend to decrease with time.

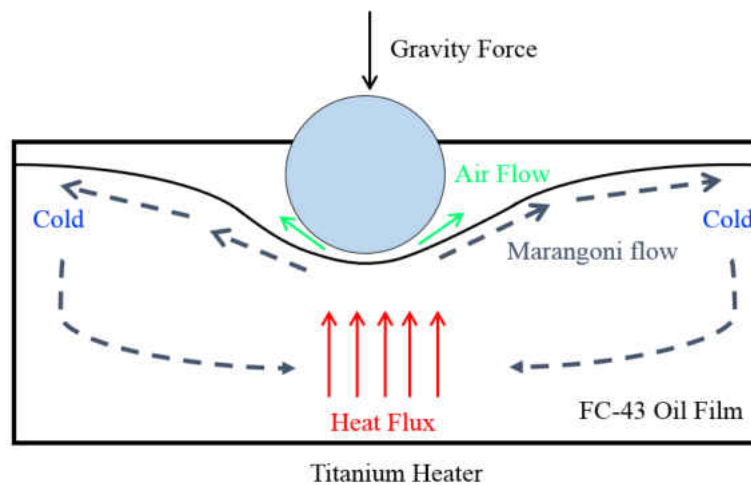


Figure 6.4: Trapping of a drop is realized through applied thermal gradient.

After the demonstration of a droplet actuation and trapping, a similar approach is applied for assaying and manipulating of biological reagents (Banerjee et al. 2015; Srinivasan et al. 2004). We conducted the glucose oxidaseperoxide reaction to verify the performance of our microfluidic device.

Glucose (sugar) is a carbohydrate that is considered as the main source of energy in cells. The glucose level in blood needs to be monitored in a regular basis to avoid an unbalance in blood sugar, which in advanced cases may result in diabetes (persistent hyperglycemia) disease. The biological reagents are prepared as following. One part of sodium phosphate (250 mM) was diluted with four parts of purified water. The diluted buffer is stored at 4°C. Then 6 ml of the prepared buffer is mixed with 1vial of glucose colorimetric enzyme mixture. Required amounts of 1000 mg/dL glucose is mixed with buffer to produce 50 mg/dL concentration of glucose assay. The droplet of enzymatic assay is mixed with the glucose at the desired location (determined with green in Fig. 6.5a), due to the color change qualitative detection of glucose is possible (Glucose Colorimetric Assay Kit Booklet, 2015).

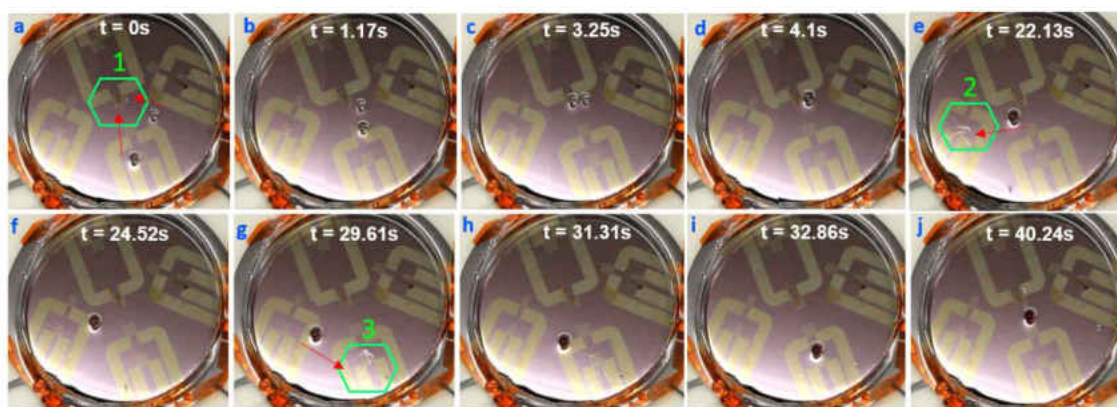


Figure 6.5: Demonstration of mixing and further manipulation of glucose and enzyme drops after coalescence at selected times.

In mixing these compounds, both the droplets are generated simultaneously. The central heater is turned on for 2 s after droplets were released (Fig. 6.5a), due to the developed surface deformation, droplets were transported towards the central heater, where they coalesced and mixed (Fig. 6.5b-d). Then heater 2 is turned on for 2 s, as a result the droplet is attracted towards it (Fig. 6.5e). The same procedure is repeated with heater 3 (Fig. 6.5f-g). The initial color change in the reaction product appeared only after 12 s and it took ~ 32 s so that the color gradient with time tends to zero. Since an enzyme mixture has a lyophilic effect, the tip of the needle is dipped into glycerin before droplet generation to avoid direct contact between the enzyme and carrier fluid which was an oil (biofouling). This approach along with typical detection techniques such as fluorescence microscopy could be used to determine the concentration of glucose in a mixture. The proposed platform could be used for manipulation of other types of biochemical assays that have a similar or smaller size.

CHAPTER 7: SUMMARY AND OUTLOOK

7.1: Conclusions

In this dissertation, the motion of a spherical droplet on a free surface of a thin liquid layer, caused by lateral thermal gradients, is investigated. While normally occurring lens-shaped droplets (e.g. water on oil), move in the direction of decreasing temperatures, it is demonstrated that levitated droplets move in the opposite direction of Marangoni convection towards increasing temperatures. The droplet stays levitated on the surface since the buildup pressure balances the van der Waals attraction forces between the surface and droplet. When van der Waals forces become dominant, the air cushion in between them shrinks and finally the droplet would penetrate the liquid surface and submerge in the liquid.

The motion of these droplets is primarily governed by the dynamics of the underlying liquid film. When a thermal gradient is maintained across a thin liquid platform, two key phenomena occur: (1) the free surface gets deformed such that the high temperature regions become depressed, and (2) a flow develops on the free surface that carries the fluid from the hot end towards the cold side of the thermal gradient. These phenomena were used to explain the migration of the spherical droplets initially resting at the air-liquid interface of an immiscible liquid, subjected to a thermal gradient. Based on the dynamics of thin liquid films subject to thermal gradients, a theoretical model has been developed. First, the surface velocity and the slope of the depression of the free surface are solved from the governing equations for a Marangoni flow. Then, using the solution for the surface velocity and surface elevation gradient, a force balance is used to model the motion of the levitated droplet. The

resulting model is an initial value problem in the form a second order nonlinear partial differential equation. The droplet velocity was obtained using a fourth order Runge-Kutta solver. In addition, the theoretical solution provides the drag coefficient on the droplet due to the liquid front from the Marangoni flow. This drag coefficient is found to be larger than that for a fully immersed sphere by 66% to 22% for Reynolds number between 2- 32.

In addition, the collision behavior of identical drops is studied experimentally as a result of a thermal gradient on a thin film. The existence of the transition line between coalescence and stretching separation in this passive mode of transport is similar to what was observed in the literature for force coalescence at significantly higher Weber numbers. A similar concept is used to levitate two droplets of an equal size at different chemical compositions, and allows for a chemical reaction to take place upon collision. The mixing percentage at every instant is calculated by evaluation of color image processing. The temperature gradient on the substrate heats up the droplet and enhances the mixing. This mixing percentage increases with increasing temperature. Mixing rates as high as 74% is found to be reachable within 120 ms. For all cases, an increase in droplet inertia (Reynolds number) shortens the mixing time. However, the time required to achieve a saturated level of mixing is found to be nearly the same. The results also suggest that the reduction in droplet size favorably enhances the mixing percentage. Thus, utilizing a thermocapillary environment allows for the droplets to work as microreactors in digital microfluidic applications to perform rapid and efficient mixing of reagents.

This study offers new insight into the intricate dynamic of droplets and thermo-coalescence. It also demonstrates how the natural coalescence is used to transport, mix and collect reagents

more efficiently. These results can be engineered to enhance performance of self-cleaning surfaces, thermal diodes and micro-total analysis systems.

7.2: Outlook and future directions

As discussed in this thesis, thermocapillary effect is a promising actuation mechanism with stability that can be simply applied for manipulation of droplets in different systems. This thesis clarifies the underlying physics which govern the levitation of droplets above a thin liquid film. With this understanding, future innovations in microfluidic technology can be applied. In the following sections, the main challenges and potentials of thermocapillary actuation of samples are addressed.

- 1) It is observed that droplets levitated on a liquid surface in some cases react differently to collision. For instance, droplets of the same fluid may be grouped together to form conglomerate configuration. More research needs to be done on this area to understand why the coalescence is not taking place even at low impact velocities. Another example is the encapsulation of droplets. Under certain conditions, the droplet after impact is enclosed by the other one which is typically larger in size. These conditions, such as viscosity ratio, surface tension ration and size have never been studied. Therefore finding the margins under which coalescence, encapsulation or conglomerate configuration may occur would be interesting for the design micro-reactors and virtual shells for sensitive reagents.

- 2) Based on the presented results, thermal manipulation and thermo-coalescence is a promising solution to overcome the challenges that exist in mixing at low Reynolds number flows, strong inertial and convective forces are absent. Thus further extension of this methodology to micro and nanochannels will create a new and practical approach to reach rapid and efficient mixing schemes.
- 3) From an application point of view, so far the utilization of the thermocapillary effect, has resulted in two types of tests: i) actuation, transfer and mixing of chemical reagents (KOH and pH-indicator), ii) transfer, mixing and trapping of biological assays (glucose and enzyme). In the next level, the conventional laboratory operations could be implemented on custom designed platforms to meet specific requirements. For example, desired type of cell can be encapsulated inside a droplet by generating a spherical-shaped levitated droplet from HBSS (Hanks' balanced salt solution) or RPMI buffer that contains cells. The fluorescence beads can be added to the solution and then visualized under a fluorescence microscope or a white light microscope. Since these beads are taken up by cells, the detection and study of cells is feasible. Special attention is required to prepare the sample and generate droplets. However, compared to a traditional approach this method simplifies the handling and detection of cells for biologists to analyze the cell behavior.

In Fig. 7.1 we show a proof of concept for cell manipulation by generating droplets containing macrophages in a RPMI solution with fluorescence particles. Macrophage is a type of white blood cell that ingests foreign material. We managed to maneuver these droplets to desired locations similar to what is shown for glucose and

KOH-phenolphthalein solution. Then these droplets are collected and tested using fluorescence microscopy to see the cell population as well the effect of temperature on them. The cells that absorbed the fluorescence particles change their shape to spherical. This result confirms the potential of thermal manipulation of cells without negative influence on their characteristic. This approach can open up new avenues in testing efficiency of new drugs, cell and bead encapsulation and tissue fabrication.

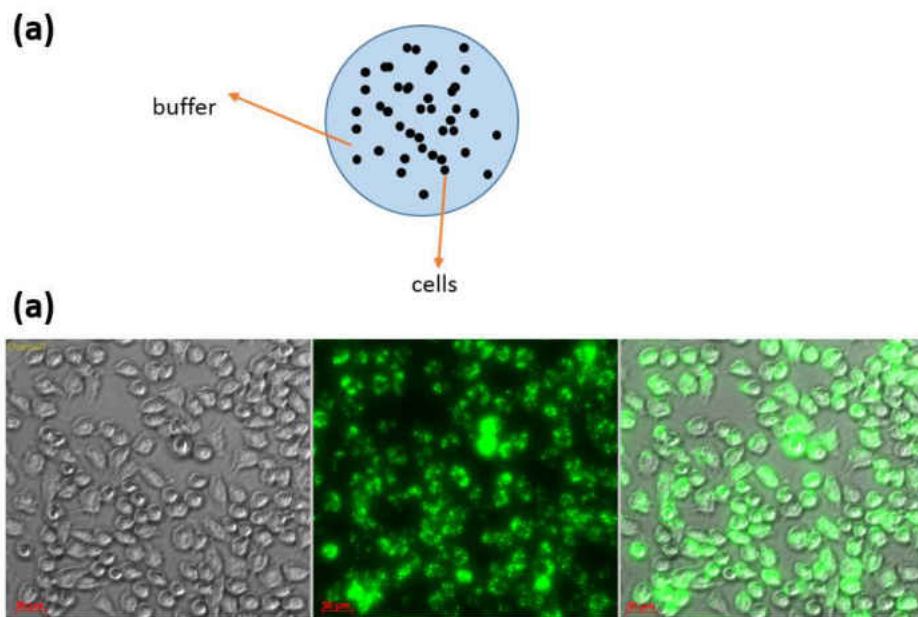


Figure 7.1: (a) Schematic of a generated droplet where cells are within RPMI medium. (b) White light image of a 2mm droplet containing the cell buffer, fluorescence image and overlap of earlier two images (from left to right).

**APPENDIX: THEORETICAL MODEL FOR MARANGONI FLOW
INSIDE THE THIN FILM AND DROPLET MOTION**

Governing Equations

Equations in section 2.3.2 have been normalized by Pimputkar and Ostrach³⁶. Following their work and using proper scales:

$$x^* = \frac{x}{L}, \quad y^* = \frac{y}{D}, \quad h^* = \frac{H}{D}, \quad A = \frac{D}{L}, \quad u^* = \frac{u}{U}, \quad v^* = \frac{v}{U.A}, \quad t^* = \frac{t}{\tau}, \quad \theta = \frac{T - T_C}{T_H - T_C}$$
$$p = [p - p_{atm} - \rho g(H - Y)]. \left(\frac{\mu U L}{d^2} \right)^{-1}$$

The non-dimensional numbers are defined as:

$$Bo = \rho g L^2 \left\{ \left| \frac{\partial \sigma}{\partial T} \right| (T_H - T_C) \right\}^{-1} \xrightarrow{U = \frac{\partial \sigma}{\partial T} A (T_H - T_C) \mu^{-1}} Bo = \frac{\rho g L^2}{U \mu} A$$

$$Ma = \left| \frac{d\sigma}{dT} \right| \frac{1}{\mu \alpha} L (T_H - T_C)$$

$$Pr = \frac{\nu}{\alpha}$$

$$Re = \frac{UL}{\nu}$$

Model for the Motion of Levitated Droplets

In section 2.3.3, Equation 2.17 can be rewritten as following:

$$m \frac{du_d}{dx} = -\frac{mg}{u_d} \cdot \frac{dh}{dx} + \frac{C_D}{2} (\rho_f S) \frac{(v_{rel})^2}{u_d}$$

$$\frac{du_d}{dx} = -\frac{g}{u_d} \cdot \frac{dh}{dx} + \frac{C_D}{2m} (\rho_f S) \frac{(u_d + u_{surf})^2}{u_d}$$

$$\frac{\tilde{U}}{L} \frac{du_d^*}{dx^*} = -\frac{g}{u_d^* \tilde{U}} \cdot \frac{D}{L} \cdot \frac{dh^*}{dx^*} + \frac{C_D}{2m} (\rho_f S) \frac{(u_d^* \tilde{U} + u_{surf}^* \tilde{U})^2}{u_d^* \tilde{U}}$$

$$\frac{du_d^*}{dx^*} = \frac{-gD}{\tilde{U}^2} \frac{dh^*}{dx^*} \frac{1}{u_d^*} + \frac{C_D}{2m} (\rho_f LS) \frac{(u_d^* + u_{surf}^*)^2}{u_d^*}$$

Assuming:

$$C_1 = \frac{gAL}{\tilde{U}^2} = \frac{A}{Fr^2}$$

$$C_2 = \frac{C_D}{2m} (\rho_f SL) = \frac{3}{8} \frac{C_D fL}{r_{drop}} \frac{\rho_f}{\rho_{drop}}$$

$$\frac{du_d^*}{dx^*} = -C_1 \frac{dh^*}{dx^*} \frac{1}{u_d^*} + C_2 \frac{(u_d^* + u_{surf}^*)^2}{u_d^*}$$

LIST OF REFERENCES

- Raghuram, S., Raghavan, V., Pope, D. N., & Gogos, G. (2012). Numerical study of Marangoni convection during transient evaporation of two-component droplet under forced convective environment. *International Journal of Heat & Mass Transfer*, 55, 7949–7957.
- Son, G. (2014). A sharp-interface level-set method for analysis of Marangoni effect on microdroplet evaporation. *International Journal of Heat & Mass Transfer*, 58, 156-165.
- Brochard, F. (1989). The motion of bubbles in a vertical temperature gradient. *Langmuir*, 5, 432-438.
- Brzoska, J.B., Brochard-Wyart, F., & Rondelez, F. (1993). Motions of droplets on hydrophobic model surfaces induced by thermal gradients. *Langmuir* 9, 2220-2224.
- Grigoriev, R. O., Schatz, M. F., & Sharma, V., (2006). Chaotic mixing in microdroplets. *Lab Chip* 6, 1369 – 1372.
- Xie, J. C., Lin, H., Zhang, P., Liu, F., & Hu, W. R., (2005). Experimental investigation on thermocapillary drop migration at large Marangoni number in reduced gravity. *Journal Colloid Interface Sci.*, 285, 737-743.
- Zhang, L., Subramanian, R. S., & Balasubramaniam, R. (2001). Motion of a drop in a vertical temperature gradient at small Marangoni number: the critical role of inertia. *Journal Fluid Mechanics*, 448, 197-211.
- Dell'Aversana, P., Monti, R., & Gaeta, F. S. (1995). Marangoni flow and coalescence phenomena in microgravity. *Advances in Space Research*. 16, 95-103.
- Monti, R. (2001). *Physics of fluids in microgravity*. London: U.K., Taylor and Francis.
- Greco, E. F., & Grigoriev, R. O., (2009). Thermocapillary migration of interfacial droplets, *Physics of Fluids*, 21, 042105.
- Samareh, B., Mostaghimi, J., & Moreau, C. (2014). Thermocapillary migration of a deformable droplet. *International Journal of Heat & Mass Transfer*, 73, 616-626.
- Wegener, M. (2014). A numerical parameter study on the impact of Marangoni convection on the mass transfer at buoyancy-driven single droplets. *International Journal of Heat & Mass Transfer*, 71, 769-778.

- Wegener, M., Paul, N., & Kraume, M. (2014). Fluid dynamics and mass transfer at single droplets in liquid/liquid systems. *International Journal of Heat & Mass Transfer*, 71, 475-495.
- Wu, Z. B. (2014). Thermocapillary migration of a droplet with a thermal source at large Reynolds and Marangoni numbers. *International Journal of Heat & Mass Transfer*, 75, 704-709.
- Davanlou, A., Cho, H. J., & Kumar, R. (2014). Motion of spherical droplets against Marangoni flow in a thin liquid film. *Journal of Heat Transfer*, 136, 080915-1.
- Yakhshi-Tafti, E., Cho, H. J., Kumar, R. (2010). Droplet actuation on a liquid layer due to Thermocapillary motion: Shape Effect. *Applied Physics Letters*, 96, 264101.
- Yakhshi-Tafti, E., Cho, H. J., & Kumar, R. (2010). Impact of drops on the surface of immiscible liquids. *Journal of Colloid and Interface Sciences*, 350, 373-376.
- Basu, A. S., & Gianchandani, Y. B. (2007). Shaping high-speed Marangoni flow in liquid films by microscale perturbations in surface temperature. *Applied Physics Letters*, 90, 034102.
- Davanlou, A., & Kumar, R., (2015). Thermally induced collision of droplets in an immiscible outer fluid. *Scientific Reports* 5, 9531; doi:10.1038/srep09531.
- Thoroddsen, S. T., Etoh, T. G., & Takehara, K. (2003). Air entrapment under an impacting drop. *Journal of Fluid Mechanics*, 478, 125-134.
- Sreenivas, K. R., De, P. K., & Arakeri, J. (1999). Levitation of a drop over a film flow. *Journal of Fluid Mechanics*, 380, 297-307.
- Gilet, T., Vandewalle, N., & Dorbolo, S. (2007). Controlling the partial coalescence of a droplet on a vertically vibrated bath. *Physical Review E*, 76 035302.
- Pimputkar, S. M., & Ostrach, S. (1980). Transient thermocapillary flow in thin liquid layers. *Physics of Fluids*, 23, 1281-1285.
- Olsson, E., Kreiss, G., Zahedi, S. (2007). A conservative level set method for two phase flow II. *Journal of Computational Physics*, 225, 785–807.
- Savino, R., Paterna, D. & Lappa, M. (2003). Marangoni flotation of liquid droplets. *Journal of Fluid Mechanics*, 479, 307-326.
- Morrison, F. A. (2013). *An Introduction to Fluid Mechanics*. New York: Cambridge University Press.

- Squires, T. M., & Quake, S. R. (2005). Microfluidics: Fluid physics at the nanoliter scale. *Review of Modern Physics*, 77, 977-1026.
- Beebe, D. J., Mensing, G. A., & Walker, G. M. (2002). Physics and applications of microfluidics in biology. *Annual Review of Biomedical Engineering*, 4, 261–86.
- Yakhshi-Tafti, E., Cho, H. J., & Kumar, R. (2010). Droplet actuation on a liquid layer due to thermocapillary motion: Shape effect. *Applied Physics Letters*, 96, 264101.
- Zhao, Y., Liu, F., & Chen, C. H. (2011). Thermocapillary actuation of binary drops on solid surfaces. *Applied Physics Letters*, 99, 104101.
- Christopher, G. F., et al., (2009). Coalescence and splitting of confined droplets at microfluidic junctions. *Lab Chip*, 9, 1102-1109.
- Javadi, A., Habibi, M., Taheri, F. S., Moulinet, S. & Bonn, D. (2013). Effect of wetting on capillary pumping in microchannels. *Scientific Reports* 3, 1412; doi:10.1038/srep01412.
- Rayleigh, L. (1879). On the Capillary Phenomena of Jets. *Proceeding of Royal Society London A*, 29, 71-97.
- Adam, J. R., Lindblad, N.R., & Hendrick, C.D. (1968). The Collision, Coalescence, and Disruption of Water Droplets. *Journal of Applied Physics*, 39, 5173-5180.
- Brazier-Smith, P. R., Jennings, S. G. & Latham, J. (1971). Accelerated rates of rainfall. *Nature* 232, 112–113.
- Abbott, C. E., (1973). *Review of Geophysics Space Phys.* 15, 363-374.
- Nikolopoulos, N., Nikas, K. S. & Bergeles, G. (2009). A numerical investigation of central binary collision of droplets. *Computers and Fluids*, 38, 1191–1202.
- Soltman, D. & Subramanian, V. (2008). Inkjet-printed line morphologies and temperature control of the coffee ring effect. *Langmuir* 24, 2224–2231.
- Armani, M., Chaudhary, S., Probst, R., Walker, S. & Shapiro, B. (2005). Control of microfluidic systems: two examples, results, and challenges. *International Journal of Robust Nonlinear Control*, 15, 785–803.
- Hirato T., Koyama K., Tanaka T., Awakura Y., & Majima H. (1991). Demulsification of water-in-oil emulsion by an electrostatic coalescence method. *Material Transactions*, 32, 257–63.

- Ashgriz, N. & Poo, J. Y. (1990). Coalescence and separation in binary collisions of liquid drops. *Journal of Fluid Mechanics*, 221, 183–204.
- Orme, M. (1997). Experiments on droplet collisions, bounce, coalescence and disruption. *Progress in Energy and Combustion Science*, 23, 65–79.
- Jiang, Y.J., Umemura, A., & Law, C.K. (1992). An experimental investigation of the collision behavior of hydrocarbon droplets. *Journal of Fluid Mechanics*, 234, 171-190.
- Qian, J. & Law, C. K. (1997). Regimes of coalescence and separation in droplet collision. *Journal of Fluid Mechanics*, 331, 59–80.
- Brenn, G. & Ashgriz, N. (Ed.). (2011). *Droplet Collision Handbook of Atomization and Sprays: Theory and Applications*. Springer: U.S., 157–181.
- Tang, C., Zhang, P. & Law, C. K. (2012). Bouncing, coalescence, and separation in head-on collision of unequal-size droplets. *Physics of Fluids*, 24, 022101.
- Narhe, R., Beysens, D. & Nikolayev, V. (2004). Contact Line Dynamics in Drop Coalescence and Spreading. *Langmuir*, 20, 1213-1221.
- Sellier, M. & Treluyer, E. (2009). Modeling the coalescence of sessile droplets. *Biomicrofluidics*, 3, 022412.
- Karpitschka, S. & Riegler, H. (2010). Quantitative experimental study on the transition between fast and delayed coalescence of sessile droplets with different but completely miscible liquids. *Langmuir* 26, 11823–11829.
- Nilsson, M. A. & Rothstein, J.P. (2011). The effect of contact angle hysteresis on droplet coalescence and mixing. *Journal of Colloid and Interface Sciences*, 363, 646-654.
- Eggers, J., Lister, J. R. & Stone, H. A. (1999). Coalescence of liquid drops. *Journal of Fluid Mechanics*, 401, 293-310.
- Wu, M., Cubaud, T., & Ho, C. M. (2004). Scaling law in liquid drop coalescence driven by surface tension. *Physics of Fluids*, 16, L51.
- Choi, S. B. & Lee, J. S. (2014). Film drainage mechanism between two immiscible droplets. *Microfluidics and Nanofluidics*, 17, 675- 681.
- Thoroddsen, S. T., Etoh, T.G., & Takehara, K. (2008). High-speed imaging of drops and bubbles. *Annual Review of Fluid Mechanics*, 40, 257-285.
- Bonn, D., Eggers, J., Indekeu, J., Meunier, J. & Etienne, R. (2009). Wetting and spreading.

Review of Modern Physics, 81, 739-805.

- Gharabaghi, M. & Aghazadeh, S. (2014). A review of the role of wetting and spreading Phenomena on the flotation practice. *Current Opinion Colloid Interface Science*; doi:10.1016/j.cocis.2014.07.004.
- Yakhshi-Tafti, E., Cho, H. J. & Kumar, R. (2010). Impact of drops on the surface of immiscible liquids. *Journal of Colloid and Interface Sciences*, 350, 373-376.
- Davanlou, A, Cho, H. J., & Kumar, R. (2014). Motion of spherical droplets against Marangoni flow in a thin liquid film. *Journal of Heat Transfer*, 136, 080915-1.
- Savino, R., Paterna, D. & Lappa, M. (2003). Marangoni flotation of liquid droplets. *Journal of Fluid Mechanics*, 479, 307-326.
- Couder, Y., Fort, E., Gautier, C-H., & Boudaoud A. (2005). From bouncing to floating: noncoalescence of drops on a fluid bath. *Physical Review Letters* 94, 177801.
- Tran, T., Maleprade, H., Sun, C. & Lohse, D. (2013). Air entrainment during impact of droplets on liquid surfaces. *Journal of Fluid Mechanics*, 726, R3.
- Hadland, P. H., Balasubramaniam, R., Wozniak, G. & Subramanian, R. S. (1999). Thermocapillary migration of bubbles and drops at moderate to large Marangoni number and moderate Reynolds number in reduced gravity. *Experiments in Fluids*, 26, 240-248.
- Yi, N. et al. (2014). Temperature-Induced Coalescence of Colliding Binary Droplets on Superhydrophobic Surface. *Scientific Reports*, 4, 4303; doi:10.1038/srep04303.
- Munnannur, A. & Reitz, R. D. (2007). A new predictive model for fragmenting and non-fragmenting binary droplet collisions. *International Journal of Multiphase Flow*, 33, 873-896.
- Arkhipov, V. A., Ratanov, G. S. & Trofimov, V. F. (1978). Experimental investigation of the interaction of colliding droplets. *Journal of Applied Mechanics and Technical Physics*, 2, 73-77.
- Wang, F. C., Feng, J. T., Zhao, Y. P. (2008). The head-on colliding process of binary liquid droplets at low velocity: High-speed photography experiments and modeling. *Journal of Colloid and Interface Sciences* 326, 196-200.
- Wehking, J. D., Gabany, M., Chew, L., & Kumar, R. (2013). Effects of viscosity, interfacial tension, and flow geometry on droplet formation in a microfluidic T-junction. *Microfluidics and Nanofluidics*, 16, 441-453.

- Aref, H. (1984). Stirring by chaotic advection. *Journal of Fluid Mechanics*, 1-21.
- Beebe, D.J., Mensing, G.A., & Walker, G.M. (2002). Physics and applications of microfluidics in biology. *Annual Review of Biomedical Engineering*, 261-286.
- Carroll, B., & Hidrovo, C. (2013). Experimental investigation of inertial mixing in colliding droplets. *Heat Transfer Engineering*, 120-130.
- Castrejón-Pita J., Kubiak K., Castrejón-Pita A., Wilson, M., & Hutchings, I. (2013). Mixing and internal dynamics of droplets impacting and coalescing on a solid surface. *Physical Review E*: 023023.
- Chang, C.C., & Yang, R.J. (2007). Electrokinetic mixing in microfluidic systems. *Journal of Microfluidics and Nanofluidics*, 501-525.
- Davanlou, A. (2014). Integration of fiber-optic sensors in measuring machines. *Journal of Measurement*, 25-32.
- Davanlou, A. & Kumar, R. (2015a). Thermally induced collision of droplets in an immiscible outer fluid. *Scientific Reports*, doi: 10.1038/srep09531.
- Davanlou, A. & Kumar, R. (2015b). Counter-current motion of a droplet levitated on a liquid film undergoing Marangoni convection. *International Journal of Heat and Mass Transfer*. <http://dx.doi.org/10.1016/j.ijheatmasstransfer.2015.05.036>.
- Grigoriev, R.O., Schatz, M.F., & Sharma, V. (2006). Chaotic mixing in microdroplets. *Lab on a Chip*, 1369-1372.
- Hosokawa, K., Fujii, T., & Endo, I. (1999). Handling of picoliter liquid samples in a poly (dimethylsiloxane)-based microfluidic device. *Analytical chemistry*, 4781-4785.
- Liu, R.H., Stremler, M.A., Sharp, K.V., Olsen, M.G., Santiago, J.G., Adrian, R.J., Aref, H., & Beebe, D.J. (2000). Passive mixing in a three-dimensional serpentine microchannel. *Journal of Microelectromechanical Systems*, 190-197.
- Nilsson, M.A., & Rothstein, J.P. (2011). The effect of contact angle hysteresis on droplet coalescence and mixing. *Journal of Colloid and Interface Science*, 646-654.
- Ortiz-Dueñas C., Kim, J., & Longmire, E. K. (2010). Investigation of liquid–liquid drop coalescence using tomographic PIV. *Experiments in Fluids*, 111-129.

- Paik, P., Pamela, V.K., Pollack, M.G., & Fair, R.B. (2003). Electrowetting-based droplet mixers for microfluidic systems. *Lab on a Chip*, 28-33.
- Samie, M., Salari, A., & Shafii, M.B. (2013). Breakup of microdroplets in asymmetric T junctions. *Physical Review E*: 053003.
- Song H, Bringer MR, Tice JD, Gerdtz CJ and Ismagilov RF (2003) Experimental test of scaling of mixing by chaotic advection in droplets moving through microfluidic channels. *Applied Physics Letters*, 4664-4666.
- Stone, Z., & Stone, H. (2005). Imaging and quantifying mixing in a model droplet micromixer. *Physics of Fluids* (1994-present):063103.
- Stroock, A.D., Dertinger, S.K., Ajdari, A., Mezić, I., Stone, H.A., & Whitesides, G.M. (2002). Chaotic mixer for microchannels. *Science*, 647-651.
- Wiggins, S., & Ottino, J.M. (2004). Foundations of chaotic mixing. *Philosophical Transactions of the Royal Society of London Series A: Mathematical, Physical and Engineering Sciences*, 937-970.
- Wu, Z., & Nguyen, N.T. (2005). Rapid mixing using two-phase hydraulic focusing in microchannels. *Biomedical Microdevices*, 13-20.
- Yakhshi-Tafti E, Cho H.J. & Kumar, R. (2008). Effect of laminar velocity profile variation on mixing in microfluidic devices: the sigma micromixer. *Applied Physics Letters*, 143504.
- Yakhshi-Tafti E., Cho, H.J., & Kumar, R. (2011). Diffusive mixing through velocity profile variation in microchannels. *Experiments in Fluids*, 535-545.
- Yeh, S.I., Fang, W.F., Sheen, H.J., & Yang, J.T. (2013). Droplets coalescence and mixing with identical and distinct surface tension on a wettability gradient surface. *Microfluidics and Nanofluidics*, 785-795.
- Yeh, S.I., Sheen H-J and Yang, J.T. (2014). Chemical reaction and mixing inside a coalesced droplet after a head-on collision. *Microfluidics and Nanofluidics*, 1-9.
- Yakhshi-Tafti, E., Cho, H. J., & Kumar, R. (2010). Impact of drops on the surface of immiscible liquids. *Journal Colloid Interface Science*. 350, 373-376.

- Davanlou, A., Cho, H. J. & Kumar, R. (2014). Motion of spherical droplets against Marangoni flow in a thin liquid film. *Journal of Heat Transfer*, 136, 080915-1.
- Savino, R., Paterna, D., & Lappa, M. (2003). Marangoni flotation of liquid droplets. *Journal of Fluid Mechanics*, 479, 307-326.
- Davanlou, A., Shabani, R., Cho, H.J., & Kumar, R. (2013). Is Thermocapillary Enough for Droplet Actuation? *MicroTAS*, Freiburg-Black Forest, Germany, Oct. 27-31.
- Tran, T., Maleprade, H., Sun C., & Lohse, D. (2013). Air entrainment during impact of droplets on liquid surfaces. *Journal of Fluid Mechanics*. 726, R3.
- Nakai, T., Ueno, T., Kanzawa, K., & Goto, T. (2011). Temperature Dependence of the lifetime of a droplet on a liquid surface. *Journal of Robotics and Mechatronics*, 23, 386-391.
- Sreenivas, K. R., De P. K., & Arakeri, J. (1999). Levitation of a drop over a film flow. *Journal of Fluid Mechanics*, 380, 297-307 1999.
- Amarouchene, Y., Cristobal, G., & Kellay, H. (2001). Noncoalescing drops. *Phys. Rev. Letters*, 87 (20), 206104.
- Monti, R., & Dell-Aversana, P. (1994). Microgravity experimentation in non-coalescing system. *Microgravity Q*, 4, 123-133.
- Lee, J. S., Weon, B. M., Je, J. H., & Fezzaa. K. (2012). How does an air film evolve into a bubble during drop impact? *Physical Review Letters* 109, 204501.
- Richard, D., Clanet, C., & Quéré, D. (2002) Surface phenomena: Contact time of a bouncing drop. *Nature*, 417, 811-811.
- Blanchette, F., Messio, L., & Bush, J. W. M. (2009). The influence of surface tension gradients on drop coalescence. *Physics of Fluids*, 21, 072107.
- Gilet, T., Vandewalle, N., & Dorbolo, S. (2007). Controlling the partial coalescence of a droplet on a vertically vibrated bath. *Physical Review E* 76, 035302.
- Panton, R. L. (1995). *Incompressible Flow*, 2 ed. John Wiley and Sons, Inc. New York.
- Dell'Aversana, P, Tontodonato, V., & Carotenuto, L. (1997). Suppression of coalescence and wetting: the shape of the interstitial film. *Physics Fluids* 9, 2475–2485.
- Monti, R., Savino, R. & Tempesta, S. (1998). Wetting prevention by thermal Marangoni effect: Experimental and numerical simulation. *Europe Journal of Mechanics B Fluids* 17, 51–77.

- Sackmann, E. K., Fulton, A. L., & Beebe, D. J. (2014). The present and future role of microfluidics in biomedical research. *Nature*, 507, 181-189.
- Wang, Z., & Zhe, J. (2011). Recent advances in particle and droplet manipulation for lab-on-a-chip devices based on surface acoustic waves. *Lab on a Chip*, 11, 1280-1285.
- Pipper, J., Inoue, M.L., Ng, F.P., Neuzil, P., Zhang, Y., & Novak, L. (2007). Catching bird flu in a droplet. *Nature Medicine*, 13, 1259-1263.
- Zhang, Y., Park, V, Liu, K., Tsuan, J., Yang, S., & Wang, T. H. (2011). A surface topography assisted droplet manipulation platform for biomarker detection and pathogen identification. *Lab on a Chip*, 11, 398-406.
- Huang, C. J., Fang, W. F., Ke, M. S., Chou, H. Y. E., & Yang, J. T. (2014). A biocompatible open-surface droplet manipulation platform for detection of multi-nucleotide polymorphism. *Lab on a Chip*, 14, 2057.
- Jebrail, M. J., Bartsch M. S., & Patel, K. D. (2012). Digital microfluidics: a versatile tool for applications in chemistry, biology and medicine. *Lab on a Chip*, 12, 2452–2463.
- Wu, T., & Suzuki, Y. (2011). Engineering superlyophobic surfaces as the microfluidic platform for droplet manipulation. *Lab on a Chip*, 11, 3121-3129.
- Hu, W., & Ohta, A. T. (2011). Aqueous droplet manipulation by optically induced Marangoni circulation. *Microfluidics and Nanofluidics*, 11, 307-316.
- Long, Z., Shetty, A. M., Solomon, M. J., & Larson, R. G. (2009). Fundamentals of magnet-actuated droplet manipulation on an open hydrophobic surface. *Lab Chip*, 9, 1567-1575.
- Kotz, K. T., Noble, K. A., & Faris, G. W. (2004). Optical microfluidics. *Applied Physics Letters*, 85, 2658.
- Zhao, Y., Fang, J., Wang, H., Wang, X., & Lin, T. (2010). Magnetic liquid marbles: manipulation of liquid droplets using highly hydrophobic Fe₃O₄ nanoparticles. *Advanced Materials*, 22, 707-710.

- Lehmann, S. Hadjidj, V. K. Parashar, C. Vandevyver, Rida A., & Gijs, M. (2006). Two-dimensional magnetic manipulation of microdroplets on a chip as a platform for bioanalytical applications. *Sensors and Actuators B: Chemical*, 117, 457-463.
- Nguyen, N. T., Beyzavi, A., Ng, K. M., & Huang, X. (2007). Kinematics and deformation of ferrofluid droplets under magnetic actuation. *Microfluidics and Nanofluidics*, 3, 571-579.
- Millman, J. R., Bhatt, K. H., Prevo B. G., & Velev, O. D. (2005). Anisotropic particle synthesis in dielectrophoretically controlled microdroplet reactors. *Nature Materials*, 4, 98-102.
- Schwartz, J. A., Vykoukal J. V., & Gascoyne, P. R. C. (2004). Droplet-based chemistry on a programmable micro-chip. *Lab on a Chip*, 4, 11-17.
- Jones, T. B., Gunji, M., Washizu M., & Feldman, M. J. (2001). Dielectrophoretic liquid actuation and nanodroplet formation. *Journal of Applied Physics*, 89, 14441-14448.
- Park, S., Teitell, M. A., Chiou, P. Y. (2010). Single-sided continuous optoelectrowetting (SCOEW) for droplet manipulation with light patterns. *Lab on a Chip*, 2010, 10, 1655-1661.
- Friend J., & Yeo, L. Y. (2011). Microscale acoustofluidics: Microfluidics driven via acoustics and ultrasonics. *Reviews of Modern Physics*, 83, 647-704.
- Guttenberg Z., Muller, H., et al. (2005). Planar Chip Device for PCR and Hybridization with Surface Acoustic Wave Pump. *Lab on a chip*, 5, 308-317.
- Basu, A. S., & Gianchandani, Y. B. (2009). A programmable array for contact-free manipulation of floating droplets on featureless substrates by the modulation of surface tension. *Journal Microelectromechanical Systems*, 18, 1163-1172.
- Burns, M. A., & Srivastava, N. (2006). Electronic drop sensing in microfluidic devices: automated operation of a nanoliter viscometer. *Lab on a Chip*, 6, 744-751.
- Selva, B., Miralles, V., Cantat, I., & Jullien, M. C. (2010). Thermocapillary actuation by optimized resistor pattern: bubbles and droplets displacing, switching and trapping. *Lab on a Chip*, 10, 1835-1840.
- Ichimura, K., Oh, S. K., & Nakagawa, M. (2000). Light-Driven Motion of Liquids on a Photoresponsive Surface. *Science*, 288, 1624-1626.
- Lee, J., & Kim, C. J. (2000). Surface-tension-driven microactuation based on continuous electrowetting. *Journal of Microelectromechanical Systems*, 9, 171-180.

- Chiou, P. Y., Park, S. Y., & Wu, M. C. (2008). Continuous optoelectrowetting for picoliter droplet manipulation. *Applied Physics Letters*, 93, 221110.
- Daniel, S., Chaudhury M. K., & De Gennes, P. G. (2005). Vibration-actuated drop motion on surfaces for batch microfluidic processes. *Langmuir*, 21, 4240-4248.
- Huang, X. Y., Jiao, Z. J., Nguyen, N. T., & Abgrall, P. (2008). Thermocapillary actuation of droplet in a planar microchannel. *Microfluidics and Nanofluidics*, 5, 205–214.
- Darhuber, A. A., Valentino, J. P., & Troian, S. M. (2010). Planar digital nanoliter dispensing system based on thermocapillary actuation. *Lab Chip*, 10, 1061–1071.
- Akbari, M., Bahrami M., & Sinton, D. (2012). Optothermal sample preconcentration and manipulation with temperature gradient focusing. *Microfluidics and Nanofluidics*, DOI: 10.1007/s10404-011-0866-6.
- Liu, M.C., Wu, J. G., Tsai, M. F., et al., (2012). Two dimensional thermoelectric platforms for thermocapillary droplet actuation. *RSC Advances*, 2, 1639–1642. DOI: 10.1039/c1ra00896j.
- Xing, S., Harake, R. S., & Pan, T. (2011). Droplet-driven transports on superhydrophobic-patterned surface microfluidics. *Lab Chip*, 11, 3642-3646.
- Pompano, R. R., Liu, W., Du, W., & Ismagilov, R. F. (2011). Microfluidics using spatially defined arrays of droplets in one, two, and three dimensions. *Annual Review of Analytical Chemistry*, 4, 59–81.
- Basu, A. S., & Gianchandani, Y. B., (2008). Virtual microfluidic traps, filters, channels and pumps using Marangoni flows. *Journal of Micromechanics Microengineering*, 18, 1163-1172.
- Bejan, A., (1993). Time-dependent conduction. Heat transfer (143-215). New York, Wiley.
- Banerjee, A., Noh, J. H., Liu, Y., Rack, P. D., & Papautsky, I. (2015). Programmable Electrowetting with Channels and Droplets. *Micromachines*, 6, 172-185.
- Srinivasan, V, Pamula, V. K., Fair, R. B. (2004). Droplet-based microfluidic lab-on-a-chip for glucose detection. *Analytica Chimica Acta*, 507, 145-150.
- Glucose Colorimetric Assay Kit Booklet. (2015), *Cayman Chemical*, Retrieved from <https://www.caymanchem.com/pdfs/10009582.pdf>.